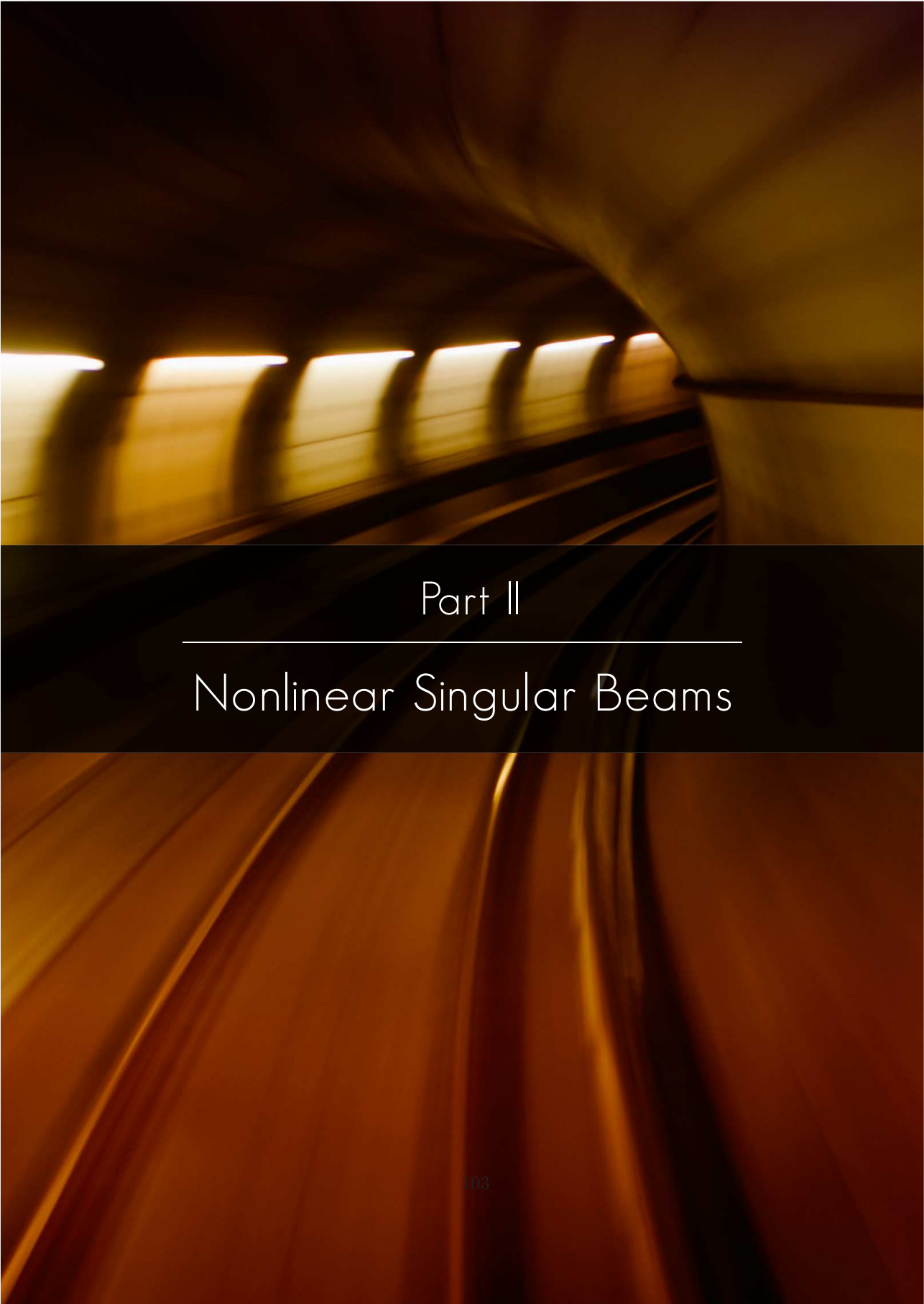
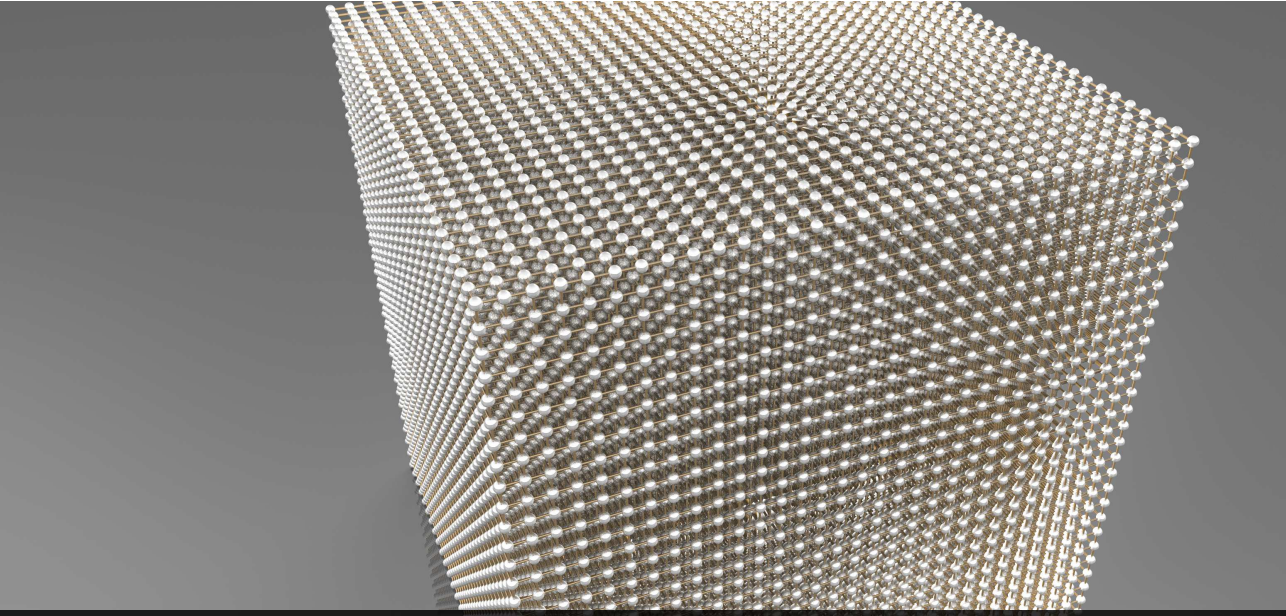


Part II

Nonlinear Singular Beams



Chapter 3

Nonlinear Self-Collimated Beams in Periodic Media

Abstract

We report the propagation of high-intensity sound beams in a sonic crystal, under self-collimation or reduced-divergence conditions. The medium is a fluid with elastic quadratic nonlinearity, where the dominating nonlinear effect is harmonic generation. The conditions for the efficient generation of narrow, non-diverging beam of second harmonic are discussed. Numerical simulations are in agreement with the analytical predictions made, based on the linear dispersion characteristics in modulated media and the nonlinear interaction in a quadratic medium under phase matching conditions.

3.1 Introduction

The beams of different kind of waves, electromagnetic, sonic, etc..., experience diffraction and broaden as they propagate in a homogeneous medium. This spreading of energy in space diminishes the wave amplitude of the beam in the axis along propagation, unless the spreading is balanced by some focusing mechanism. Still, it is possible to prevent this fundamental wave propagation property and create non-diverging beams. Among the beam patterns without divergence the most popular are the linear Bessel beams (J. Durnin et al., 1987), and the nonlinear solitonic or self-trapped beams (Stegeman et al., 1999). Recently, another method for creating linear non-diverging beam was proposed, for waves propagating in a periodic medium. Such beams have been named self-collimated beams, and were first proposed for light beams in photonic crystals (Kosaka et al., 1999), and later extended to other type of waves. The phenomenon of self-collimation has attracted much attention, as a technique to propagate optical, acoustical or even matter wave beams at long distances without a sensible loss of amplitude. Self-collimation is highly sensitive to the frequency: the divergence of beams can be reduced or even suppressed only at particular frequencies, those presenting particular dispersion characteristics, namely flat regions in the isofrequency contours (Kosaka et al., 1999). The size of the self-collimated beam is also limited by the extension of such flat region in angular space.

Self-collimation of low amplitude (linear), monochromatic acoustic waves has been demonstrated in 2D (Espinosa et al., 2007) and 3D (Soliveres et al., 2009) sonic crystals. More recently, the simultaneous self-collimation of two beams of different frequencies was also demonstrated experimentally (Soliveres et al., 2011). These results show that the conditions for self-collimation can be achieved also for non-monochromatic beams; in particular the case of the superposition of beams of one frequency and its second harmonic was considered in (Soliveres et al., 2011). The latter results are valid in linear regime; actually in (Soliveres et al., 2011) both frequency components were present in the input beam, and the corresponding beams propagated in the crystal without nonlinear interaction between them.

In the linear case, the propagation of light and sound beams obey similar equations, and similar propagation characteristics are expected. The similarities between photonic and sonic crystals are well established (Miyashita, 2005), and have motivated many studies, where analogous effects in both systems have been investigated. The analogy, however, breaks for high amplitude waves, where nonlinear effects appear. For example, second and higher harmonic generation processes may be essentially different in optics and acoustics. One reason is the absence of intrinsic dispersion for acoustic waves propagating in homogeneous media. Nonlinear acoustical waves in nondispersive media as homogeneous fluids, eventually generate shock waves, which are not observed in optics. Also, the type and strength of nonlinearity may be different. While most common optical nonlinearities are cubic (Kerr-type), in fluids and homogeneous solids, quadratic

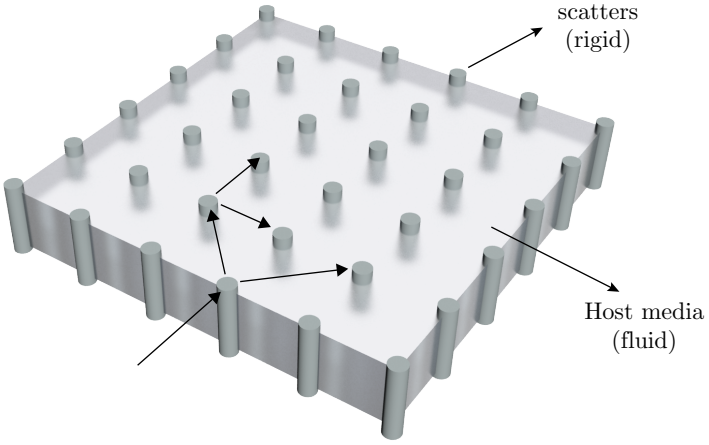


Figure 3.1: Basic scheme of a sonic crystal. The strong dispersion of the system is caused by the multiple scattering of waves over periodically distributed rigid inclusions. The resulting waves that propagates in the periodic media are Bloch waves, where the specific band structure of the media depends on the scatters and host media parameters. In this work we consider a fluid host media (nonlinear) and perfectly rigid scatters.

nonlinearity is dominant in acoustics. Even, nontraditional acoustic nonlinearities (power-law, hysteretic,...) are typical of some complex or microstructured acoustic media. In this sense, nonlinear effects of acoustic waves in periodic media, and in particular the self-collimation problem considered here are not a direct extension of the same effects in the optical case. Furthermore, the propagation of nonlinear acoustic beams in sonic crystals has never been addressed before.

The basic effect in nonlinear acoustics is harmonic generation (Hamilton et al., 1998b). It is known that efficient harmonic generation is only possible under fulfillment of phase matching conditions. For acoustic waves in fluids, this condition is rather natural, being always fulfilled for all harmonics due to the absence of dispersion, however in optics this requires special materials and special phase matching techniques (Boyd, 2003).

Acoustic harmonic generation has been studied in a variety of highly-dispersive nonlinear media, as bubbly liquids, or acoustic waveguides (Hamilton et al., 1998b), and weakly dispersive media as elastic plates (De Lima et al., 2003; Müller et al., 2010), nonlinear porous-elastic media (Donskoy et al., 1997) and in granular media (Legland et al., 2012). It has been proven as a useful effect in different applications, as material characterization (Hirsekorn et al., 1994; Zheng et al., 2000), ultrasound imaging and echography, (Humphrey, 2000), biological tissue characterization (Law et al., 1981) and other medical ultrasound applications.

The purpose of this Chapter is to study nonlinear propagation of high intensity

sound beams in periodic media, and in particular to demonstrate the formation of nonlinear self-collimated acoustic beams in sonic crystals, and discuss the conditions under which this process occurs with maximal efficiency. A sonic crystal, as sketched in Fig 3.1 is designed, by using an iterative method, to fulfill the three conditions for optimal energy transfer between harmonics: flatness of isofrequency contour for each harmonic, phase matching and large overlap between distributions of the interacting Bloch modes. The predictions are checked by FDTD simulations of the nonlinear problem, that demonstrate the efficient generation of fundamental and second harmonic acoustic narrow beams.

3.2 Nonlinear sound beam propagation model

Several models can be used to describe nonlinear sound wave propagation though a fluid medium, with different levels of accuracy. An accurate description, when thermal and viscous effects are negligible, follows from the conservation laws of mass and momentum, can be written, respectively, in a Eulerian form (Hamilton et al., 1998b):

$$\frac{\partial \rho}{\partial t} = -\nabla \cdot (\rho \mathbf{v}) \,, \tag{3.1}$$

$$\rho \left(\frac{\partial \mathbf{v}}{\partial t} + \mathbf{v} \cdot \nabla \mathbf{v} \right) = -\nabla p, \tag{3.2}$$

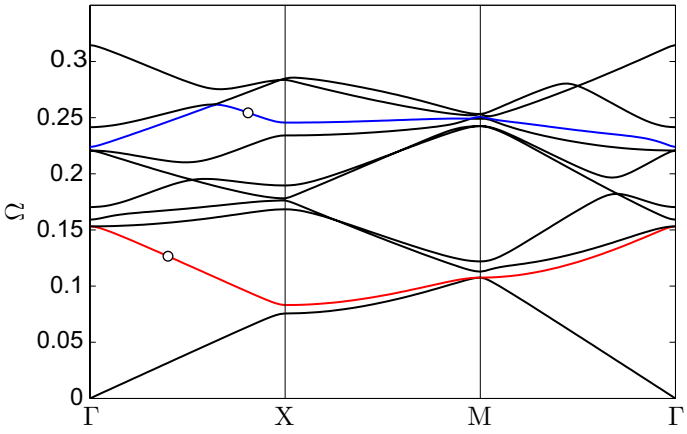


Figure 3.2: Band structure obtained by the Plane Wave Expansion (PWE) method for a SC made by a square lattice of rigid cylinders with $r = 0.11a$, where a is the lattice constant, immersed in water. Red and blue lines mark the bands (2nd and 8th) for which simultaneous nondiffractive propagation in $\Gamma - \mathrm{X}$ direction is explored for both FW and SH respectively.

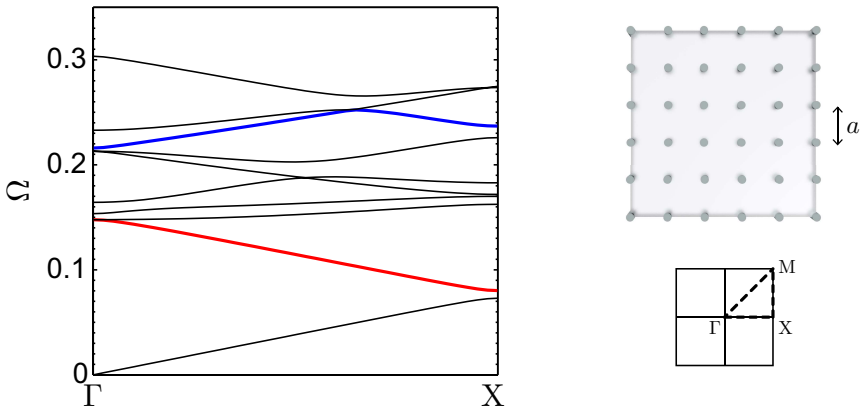


Figure 3.3: Top: Band structure (left) of a square lattice of rigid cylinders with $r = 0.11a$, where a is the lattice constant, immersed in water (right). Red and blue lines mark the bands (2nd and 8th) for which simultaneous self-collimation for both fundamental and second harmonic searched, along $\Gamma - \mathrm{X}$ direction.

where $\mathbf{v}$ is the particle velocity vector, p is the acoustic pressure, ρ is the total density field that can be expressed as $\rho = \rho_0 + \rho'$, where ρ_0 the ambient fluid density and ρ' is the acoustic density. The system is closed by the equation of state of the fluid, that under our assumptions is a pressure-density relation, $p = p(\rho)$. A commonly used expression is obtained after Taylor expansion, keeping nonlinear terms up to second order. Then

$$p = c_0^2 \rho + \frac{c_0^2}{\rho_0} \frac{B}{2A} \rho^2, \tag{3.3}$$

where B/A is the nonlinearity parameter of the medium (which is known for most of materials, see e.g. (Naugolnykh et al., 1998)) and c_0 the sound speed in the medium. Note that Eqs. (3.1) and (3.2) also contain nonlinearities related to (1) mass and momentum advection , or (2) geometrical nonlinearities. However, for the second harmonic generation they are of minor importance compared with the nonlinear terms in the equation of state, Eq. (3.3).

The above formulation of nonlinear propagation problem remains valid when the propagating medium is inhomogeneous, including the case of sonic crystals where inhomogeneity is periodically distributed in space. In such case, the medium parameters c_0 and ρ_0 are space-dependent, represented by periodic functions. To our knowledge, the propagation of acoustic beams in periodic media has been only studied in the linear regime, and the corresponding nonlinear problem is addressed here for the first time.

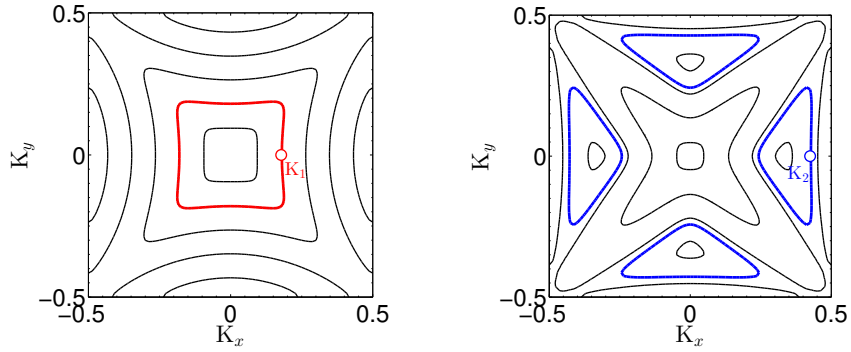


Figure 3.4: Isofrequency contours for the 2nd (left) and 8th bands (right). Points denote the wavevectors for both waves, lying on flat segments respectively.

3.3 Self-collimation of intense acoustic beams

We consider a narrow, intense acoustic beam incident on a 2D sonic crystal made of cylindrical scatterers of radius r embedded in a fluid, arranged in a square-lattice with lattice constant a. The corresponding filling fraction is $ff = \pi(r/a)^2$. The beam width is roughly 6 lattice periods. For the sake of simplicity the scatterers are considered perfectly rigid (the sound field is totally reflected from the wall of scatterer). Assuming water as a host fluid, the material parameters are $\rho_0 = 1000$ kg/m^3, $c_0 = 1490$ m/s.

The special conditions required for a sound beam to propagate without diffraction are presented in this section. The problem of self-collimation has been already discussed for linear, monofrequency (Pérez-Arjona et al., 2007; Espinosa et al., 2007) and bi-frequency (Soliveres et al., 2011) beams. Since a nonlinear beam is composed by a fundamental frequency component and its high frequency harmonics, self-collimation of the nonlinear beam requires self-collimation of its constituent frequency components. We remind that in self-collimation regime the sonic beam does not spread diffractively because Bloch wave vectors lying on the flat segment of the spatial dispersion curve have equal longitudinal components and thus do not dephase mutually in propagation. In general, this flatness of the dispersion curve appears at a particular frequency, but as shown in (Soliveres et al., 2011) it can be also obtained for a wave and its second harmonic regarded they propagate in different propagation bands.

To illustrate this case, we show in Fig. 3.3 the dispersion diagram of the sonic crystal for small-amplitude excitations, obtained using the Plane Wave Expansion (PWE) method on a linearized version of Eqs. (3.1)-(3.3). The conventional form of the band diagram is represented on the trajectory along the principal directions of the crystal, $\Gamma - \mathrm{X} - \mathrm{M} - \Gamma$, which are the boundary of the irreducible Brillouin

zone (BZ). Figure 3.3 (top) shows the dispersion diagram for $\Gamma - \mathrm{X}$ direction. The red line in Fig. 3.3 denotes the 2nd propagation band. The fundamental (driving) field lies on this band. Its frequency Ω is chosen such that the corresponding isofrequency contour contains flat regions. The blue line in Fig. 3.3 denotes the 8th propagation band. The second harmonic frequency, 2Ω, lies in this band for the particular crystal parameters considered.

As shown in (Soliveres et al., 2011), for a given crystal, it is possible to choose the fundamental frequency such that the isofrequency contours for both frequencies present flat regions. In our particular crystal, this happens when $\Omega = 0.125$. These are dimensionless frequencies, related to physical frequencies ω as $\omega = \Omega(2\pi c_0/a)$. Similarly, a normalized Bloch wavevector is defined as $\mathrm{K} = \mathrm{k}_x(a/\pi)$

Such condition is necessary to achieve self-collimated propagation of the nonlinear beam. In order to obtain an efficient generation of the second harmonic, together with simultaneous self-collimation for both waves two additional geometric conditions must be fulfilled, related to the wavenumber and spatial shape of the interacting beams. These conditions have been discussed for photonic crystals (Nistor et al., 2008; Nistor et al., 2010). The analysis can be extended to higher harmonics (third,...), however numerical simulations show that the amplitude of harmonics higher than second is small and does not contribute significantly to the beam profile, and therefore they will not be considered for the design of the structure.

3.3.1 Phase matching conditions

It is well known from nonlinear optics (Boyd, 2003) that a proper phase relationship between the fundamental and second harmonic waves must be satisfied for an efficient nonlinear frequency conversion along the propagation direction. In a dispersive medium, the wavenumbers of first harmonics do not combine to result precisely in wavevector of second harmonics, and a phase mismatch $\Delta\mathrm{K} = 2\mathrm{K}(\Omega) - \mathrm{K}(2\Omega)$ occurs. As a consequence, the second harmonic field is limited in amplitude: it does not grow linearly but oscillates in propagation, with a characteristic period given by the coherence length (Boyd, 2003)

$$l_c = \frac{\pi}{\Delta \mathrm{k}} = \frac{a}{\Delta \mathrm{K}}. \tag{3.4}$$

The conversion efficiency into second harmonics generally is smaller in optics than in acoustics, because of the inherent material dispersion for light waves (absent for sound waves in fluids), that causes the fundamental and second harmonic waves to travel along the crystal with different phase velocities. Thus, the presence of the scatterers is the only important source of dispersion in the acoustic case.

Phase matching corresponds to $\Delta\mathrm{K} = 0$. Figure 3.5 shows that it can be actually achieved for the pair of frequencies where self-collimation occurs, as follows

from the previous analysis. There, we represent the dispersion branches involved in self-collimation, along $\Gamma - \mathrm{X}$ direction, as in Fig. 3.3. Fundamental and second harmonic modes correspond to the crossings of the dotted horizontal lines with the corresponding dispersion branches. For a given fundamental frequency Ω, in order to check the fulfillment of the phase matching condition, the curve corresponding to the "double" of the 2nd band dispersion curve, $2\Omega(2\mathrm{K})$, has been represented in Fig. 3.5 as a red dashed line. Phase matching is satisfied at the intersection between this curve with the corresponding curve at the 8th band. This corresponds to the mode labeled A in Fig. 3.5, which is phase-matched with the fundamental mode.

Note that due to the concavity of the 8th band, at frequency 2Ω a second mode labelled with B in Figure. 3.5 can be also excited. This solution presents a large phase mismatch with the fundamental mode, and its contribution to the second harmonic field is negligible.

The simultaneous fulfillment of both conditions is obtained by an iterative procedure, which implies a re-design of the crystal parameters. The procedure is as follows: we start from a pair of frequencies $(\Omega, 2\Omega)$ showing self-collimation for a given crystal parameters. Around this doublet, we seek the closest pair of frequencies $\Omega' = \Omega + \delta\Omega$ and $2\Omega'$ showing phase-matching. Then the isofrequency curves (Fig. 3.3) are again calculated in order to evaluate the deviation of flatness

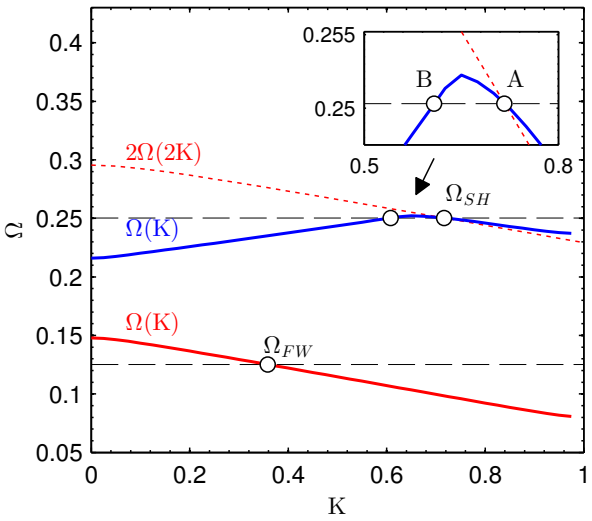


Figure 3.5: Dispersion curves involved in simultaneous self-collimation for the fundamental (red line) at the 2nd band and second harmonic (blue line) at the 8th band. The "doubled" dispersion curve is represented (dashed red line) to identify phase matching of harmonics. The intersection denotes the frequency presenting phase matching. A closest view (inset) shows that for the self-collimated second harmonic, two solutions (modes A and B, with distinct K) are found, phase and non-phase matched, respectively

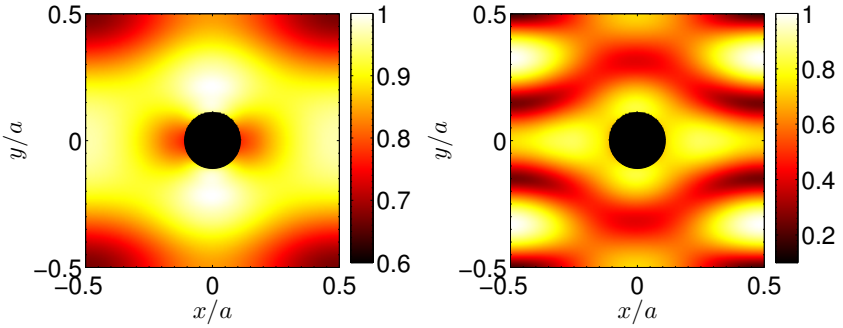


Figure 3.6: Spatial distribution of the pressure field for the Bloch modes of the fundamental (left) and the second harmonic (right) waves. The coupling coefficient is estimated to be $\kappa = 0.85$.

in the isofrequency contours. The sonic crystal parameters are then modified, e.g. by a slight variation of the filling fraction, in order to tune the dispersion relations to get again self-collimation conditions. The process is repeated again until both conditions (flatness and phase matching) are simultaneously satisfied. We note that, despite this is out of the scope of this paper, optimization techniques as genetic algorithms can be applied here in order to find an optimal structure.

3.3.2 Nonlinear coupling of Bloch modes

Efficient energy transfer between harmonics requires also a strong mode coupling, which depends on the spatial overlapping between the two interacting waves. For plane waves in a homogeneous medium a perfect spatial nonlinear coupling between first and second harmonic is assured, since mode overlapping is maximal. The propagation eigenmodes in a periodic medium are Bloch waves, whose amplitudes are spatially modulated and does not necessarily overlap. If two modes do not overlap in space, the energy transfer is less efficient even if they are phase matched. The amount of energy transfer can be estimated evaluating the spatial overlap between the envelopes of the corresponding Bloch modes.

Let B_1 and B_2 be the spatial envelopes of the Bloch modes of the fundamental and and second harmonic waves, respectively. The nonlinear coupling coefficient is calculated as the cross-correlation between the functions B_1^2 and B_2 normalized in such a way that unity would correspond to the perfect matching of the modes (Nistor et al., 2008). We define the coupling coefficient as

$$\kappa = \frac{|\int_M B_1^2\, B_2^* \mathrm{d}r|}{\sqrt{\int_C |B_1^4|\,\mathrm{d}r \int_C |B_2|^2\,\mathrm{d}r}}, \tag{3.5}$$

where the upper integral is calculated in the nonlinear medium from one unit cell, while the lower integrals are taken over the entire unit cell.

To calculate B_1 and B_2 we solve the eigenvalue problem for the pressure field by means of the PWE method, which converts the differential equation to an infinite matrix eigenvalue problem that can be truncated and solved numerically. For that, we follow the same procedure as in (Pérez-Arjona et al., 2007), however, the problem is solved inversely, i.e. for a given frequency, the corresponding wave vectors satisfying the phase matching condition are obtained. Then B_1 and B_2 are obtained as the eigenvectors corresponding to fundamental and second harmonic frequencies, respectively. In Fig. 3.6 we plot the spatial distributions of B_1 and B_2, respectively, for the selected final design where a coupling coefficient of $\kappa = 0.85$ is obtained. This value is of the same order as the coupling in homogeneous media, $\kappa = 1$, and therefore sufficiently large for an efficient harmonic generation.

3.4 Numerical simulation

A full-wave nonlinear simulation was performed, using the FDTD method, to validate the efficiency of the second harmonic generation in the proposed structure. The crystal parameters, obtained after the iterative procedure describe above, are as in Fig. 3.3 and Fig. 3.5. The source is a plane piston with a width of $6a$, located near the crystal, and radiating a harmonic wave with normalized frequency $\Omega = 0.125$. In order to minimize numerical dispersion a computational grid with $N_\lambda = 45$ elements per wavelength and a Courant-Friedrich-Levy number of $S = 0.95$ was used. In Fig. 3.7 we present the numerically obtained spatial distributions of the fundamental and its nonlinearly generated second harmonic. As predicted, both beams are nearly collimated. For comparison, the beam spatial distribution calculated for an homogeneous material (removing the crystal) are represented in Fig. 3.7 (e-f), where the diffractive broadening of the beams is visible. Transversal intensity distributions are shown in Fig. 3.8 (a-b) for a distance $80a$, where beam widths are compared with the reference beams in the homogeneous medium, broadened by diffraction.

The pressure amplitudes along the beam axis are shown in Fig. 3.9 for each harmonic. Here, the analytic solution for a nonlinear plane wave propagating in a homogeneous (nondispersive) medium is plotted for reference (dashed lines) (Naugolnykh et al., 1998), given by $p_n/p_0 = 2J_n(n\sigma)/n\sigma$, where J_n is the Bessel function of order n, $\sigma = (\beta\omega p_0/\rho_0 c_0^3)x$ is coordinate normalized to the shock formation distance, p_0 is the pressure at the source and $\beta = 1+B/2A$ the nonlinearity parameter. Such analytical solution is valid in the preshock region $\sigma < 1$. The growth rate of the self-collimated second harmonic beam propagating in the crystal matches well the growth rate of a plane wave in a homogeneous medium in such preshock region, which is a consequence of the weak divergence of the beam and the high degree of phase matching. Also, the second harmonic field can reach even higher amplitudes than those corresponding to nondispersive media (where harmonics decay beyond the shock formation distance). The latter effect can be

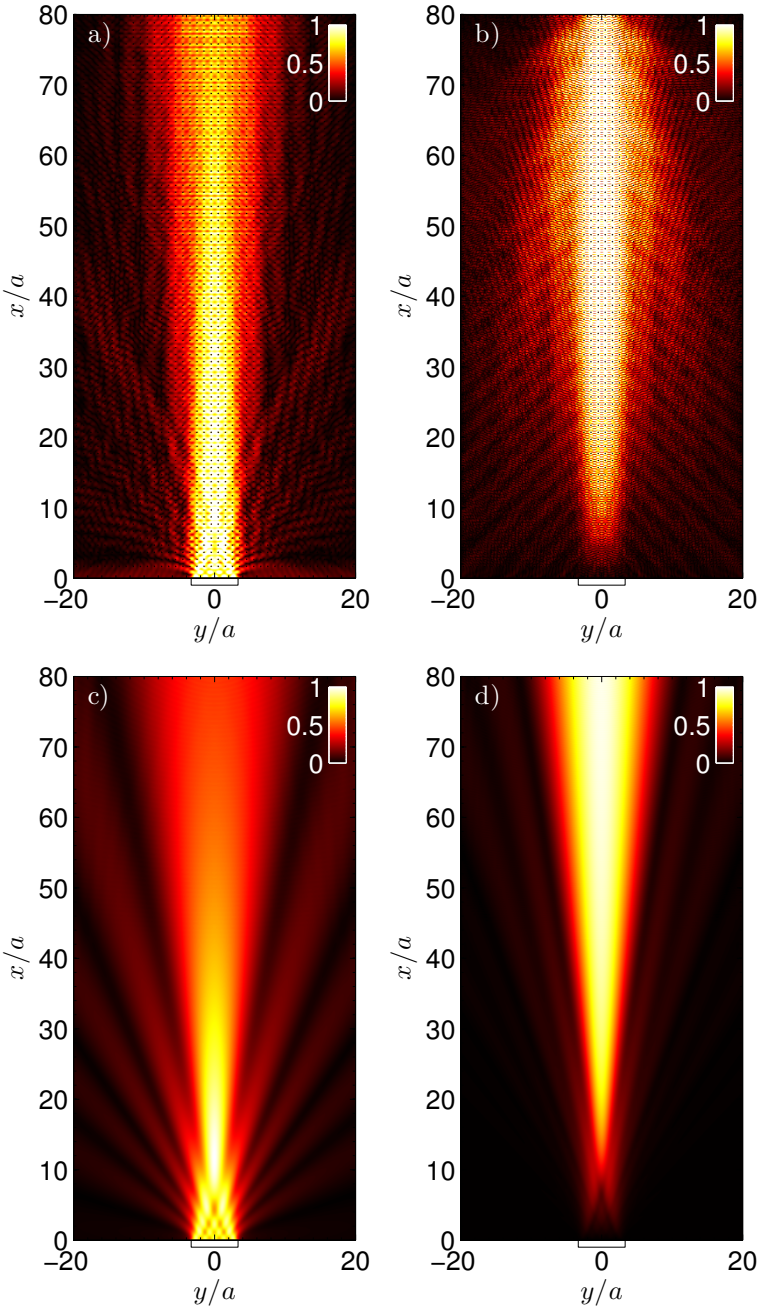


Figure 3.7: Beam spatial distribution for simultaneously self-collimated harmonics in the sonic crystal (c-d) and in homogeneous fluid (e-f). Pressures are normalized to the maximum pressure.

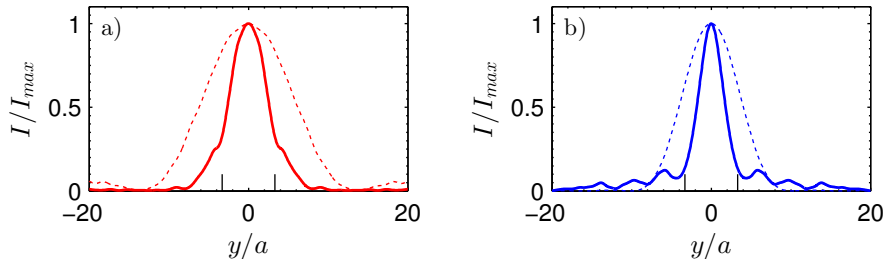


Figure 3.8: Pressure distributions obtained by FDTD simulations. Normalized intensity cross section of fundamental (a) and second harmonic (b) at $x = 80a$ propagating in the crystal (continuous line) and in a homogeneous (water) medium (dashed lines).

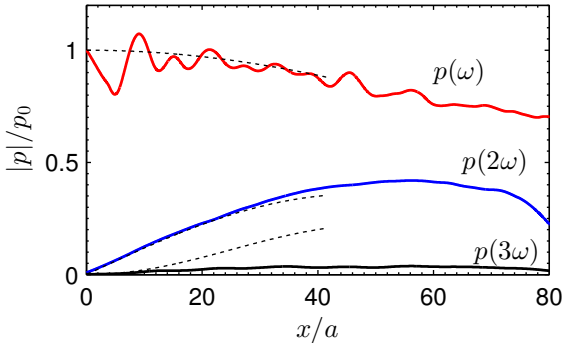


Figure 3.9: Normalized field amplitude along the acoustical axis $y = 0$, for the fundamental, second and third harmonic beams. The dashed lines represent the analytical solutions for harmonic evolution on a plane wave propagating in a nondispersive medium.

understood in terms of phase mismatch of higher harmonics: in homogeneous media all harmonics are phase matched while in the crystal only the second harmonic is phase matched. In Fig. 3.9 the third harmonic is also plotted, where its small contribution to the beam is evident. The phase mismatch in third and higher harmonics decrease the energy flow into these components. Finally, the amplitude in Fig. 3.9 decays because non-perfect conditions for self-collimation, that makes the beam to start diverging after a long distance, or non-perfect phase matching, which results in a beating period with long coherence length.

3.5 Conclusions and Remarks

We have demonstrated the possibility of efficient second harmonic generation of sound in a sonic crystal, by means of the formation of narrow, weakly diverging nonlinear acoustic beams. Three conditions must be simultaneously present for a

efficient second harmonic generation, which are: 1) simultaneous self-collimation, 2) phase mathing and 3) high spatial coupling of interacting harmonics. The use of simultaneous self-collimation regime limits the diffraction of both harmonic beams, maintaining the amplitude at the axis and therefore the nonlinear interaction. Under ideal conditions (no divergence and losses), the decrease of the first harmonic beam is mainly attributed to the energy transfer to second and higher harmonics. The sonic crystal parameters can be chosen to fulfill phase matching with the second harmonic, maximizing second harmonic generation due to synchronous cumulative interaction. Finally, the spatial coupling (overlapping) between interacting modes is also analyzed by calculating a nonlinear coupling coefficient. It is shown that its value ($\kappa = 0.85$ for the case studied) is not far from the ideal case, revealing a strong spatial overlap between both Bloch modes that leads to high energy transfer.

The study show that linear dispersion characteristics (band structures, isofrequency contours) can be used to predict the behaviour of nonlinear beams propagating in periodic media. This opens the possibility of extending the study of nonlinear sound beam propagation in sonic crystals to other cases of interest. For example, crystals with higher filling factors present full frequency bandgaps, that may be used to filter out the propagation of selected higher harmonics. In this sense, sonic crystals can be a way to control the spectrum of intense acoustic waves, using the strong dispersion properties introduced by the periodicity.

References

Boyd, Robert W (2003). *Nonlinear optics, 2nd edition*. Academic press.

De Lima, WJN and MF Hamilton (2003). "Finite-amplitude waves in isotropic elastic plates". In: *Journal of sound and vibration* 265.4, pp. 819–839.

Donskoy, D. M., K. Khashanah, and T. G. McKee (1997). "Nonlinear acoustic waves in porous media in the context of Biot???s theory". In: *The Journal of the Acoustical Society of America* 102.5, pp. 2521–2528.

Espinosa, Víctor, Víctor J Sánchez-Morcillo, Kestutis Staliunas, Isabel Pérez-Arjona, and Javier Redondo (2007). "Subdiffractive propagation of ultrasound in sonic crystals". In: *Physical Review B* 76.14, p. 140302.

Hamilton, M.F. and D.T. Blackstock (1998b). *Nonlinear Acoustics*. Academic Press.

Hirsekorn, S and S Pangraz (1994). "Materials characterization with the acoustic microscope". In: *Applied physics letters* 64.13, pp. 1632–1634.

Humphrey, Victor F (2000). "Nonlinear propagation in ultrasonic fields: measurements, modelling and harmonic imaging". In: *Ultrasonics* 38.1, pp. 267–272.

J. Durnin, J.J. Miceli and J.H. Eberly (1987). "Diffraction-free beams". In: *Phys. Rev. Lett.* 58.4, pp. 1499–1501.

Kosaka, Hideo, Takayuki Kawashima, Akihisa Tomita, Masaya Notomi, Toshiaki Tamamura, Takashi Sato, and Shojiro Kawakami (1999). "Self-collimating phenomena in photonic crystals". In: *Applied Physics Letters* 74.9, pp. 1212–1214.

Law, WK, LA Frizzell, and F Dunn (1981). "Ultrasonic determination of the nonlinearity parameter B/A for biological media". In: *The Journal of the Acoustical Society of America* 69.4, pp. 1210–1212.

Legland, JB, V Tournat, O Dazel, A Novak, and V Gusev (2012). "Linear and nonlinear Biot waves in a noncohesive granular medium slab: Transfer function, self-action, second harmonic generation". In: *The Journal of the Acoustical Society of America* 131.6, pp. 4292–4303.

Miyashita (2005). "Sonic crystals and sonic waveguides". In: *Meas. Sci. Technol.* 16, R47–R63.

Müller, Martin F, Jin-Yeon Kim, Jianmin Qu, and Laurence J Jacobs (2010). "Characteristics of second harmonic generation of Lamb waves in nonlinear elastic plates". In: *The Journal of the Acoustical Society of America* 127.4, pp. 2141–2152.

Naugolnykh, K. and L. Ostrovsky (1998). *Nonlinear Wave Processes in Acoustics*. Cambridge Texts in Applied Mathematics. Cambridge University Press.

Nistor, C, C Cojocaru, Yu Loiko, J Trull, R Herrero, and K Staliunas (2008). "Second-harmonic generation of narrow beams in subdiffractive photonic crystals". In: *Physical Review A* 78.5, p. 053818.

Nistor, Cristian, Crina Cojocaru, Jose Trull, and Kestutis Staliunas (2010). "Broad angle phase matching in subdiffractive photonic crystals". In: *Optics Communications* 283.18, pp. 3533–3535.

Pérez-Arjona, Isabel, Víctor J Sánchez-Morcillo, Javier Redondo, Víctor Espinosa, and Kestutis Staliunas (2007). "Theoretical prediction of the nondiffractive propagation of sonic waves through periodic acoustic media". In: *Physical Review B* 75.1, p. 014304.

Soliveres, Ester, Víctor Espinosa, Isabel Pérez-Arjona, Víctor J Sánchez-Morcillo, and Kestutis Staliunas (2009). "Self collimation of ultrasound in a three-dimensional sonic crystal". In: *Applied Physics Letters* 94.16, p. 164101.

Soliveres, Ester, Isabel Pérez-Arjona, R Picó, V Espinosa, Víctor José Sánchez-Morcillo, and K Staliunas (2011). "Simultaneous self-collimation of fundamental and second-harmonic in sonic crystals". In: *Applied Physics Letters* 99.15, p. 151905.

Stegeman, George I and Mordechai Segev (1999). "Optical spatial solitons and their interactions: universality and diversity". In: *Science* 286.5444, pp. 1518–1523.

Zheng, Yongping, R Gr Maev, and I Yu Solodov (2000). "Review/Sythèse Nonlinear acoustic applications for material characterization: A review". In: *Canadian Journal of Physics* 77.12, pp. 927–967.

Publications

The contents of this chapter have been presented in the following publications:

Journal papers

- Hamham, E.M., **Jiménez, N.**, Picó, R., Sánchez-Morcillo, V., García-Raffi, L., Staliunas, K. "Nonlinear self-collimated sound beams in sonic crystals". *Phys. Rev. B.* **Accepted for publication** May (2015)

Conference Proceedings

- El-M. Hamham, **N. Jiménez**, R. Picó, L. M. García-Raffi, V. J. Sánchez-Morcillo, K. Staliunas. "Efficient Second Harmonic Generation of Narrow Beams in 2D Sonic Crystals". *PHONONICS 2015: 3nd International Conference on Phononic Crystals/Metamaterials, Phonon Transport and Phonon Coupling.* Paris, France. May 31–June 5 (2015)

- Mehrem, A., Hamham, El-M., **Jiménez, N.**, Cebrecos, A., Pico, R.; Sanchez-Morcillo, V. and García-Raffi, L. M. "Nonlinear Acoustic Waves Periodic Media" *7th Forum Acusticum 2014* Krakow, Poland. September 7 (2014)



Chapter 4

Acoustic Bessel Beams generated by Axisymmetric Gratings

Abstract

We report Bessel-like beam formation of acoustic waves by means of an axisymmetric grating of rigid tori. The results show that the generated beam pattern is similar to that of Bessel beams, characterized by elongated non-diffracting focal spots. A multiple foci structure is observed, due to the finite size of the lens. The dependence of the focal distance on the frequency is also discussed, on the basis of an extended grating theory. Experimental validation of acoustic Bessel-like beam formation is also reported for sound waves. The results can be generalized to wave beams of different nature, as optical or matter waves.

4.1 Introduction

Bessel beams, originally proposed in optics (Durnin, 1987; Maddox, 1987), are now at the basis of many applications due to their unusual propagation properties (Duocastella et al., 2012; Fahrbach et al., 2011; Chu, 2012; Matsupka et al., 2006; Hsu et al., 1989a; Katchadjian et al., 2010). The most celebrated property of a Bessel beam is that, in the ideal case, the field propagates invariantly, i.e. without any diffracting broadening, in contrast to the other canonical case, the Gaussian beam, where the beam experiences diffractive broadening in free space propagation. As a consequence, the field pattern in a Bessel beam possesses an infinitely extended focal line.

Strictly speaking, Bessel beam is a solution of the wave equation in the form of a monochromatic wave with a transverse profile given by a Bessel function of the first kind, which by definition presents an infinite spatial extension. This ideal case cannot be realized in practice (in the same way as ideal, infinitely extended plane waves cannot exist). However, approximate or imperfect Bessel beams of finite transverse extent can be excited by different means, displaying not an infinite but an extremely elongated focal line.

In optics, Bessel-like beams are usually formed by focusing a Gaussian beam by an axicon (McLeod, 1954), a transparent refractive element of conical shape, as shown in Fig. 4.1 (a). The beam in propagation through the axicon acquires linearly tilted (conical) wave-fronts, which results in an elongated focus behind the axicon. As the axicon is not infinitely extended in transverse space, the resulting Bessel beam is not perfect, and displays a focal line of finite extent. Optical Bessel beams have been also obtained by acoustic gradient index lenses (McLeod et al., 2006). In electromagnetism, Bessel-like beams have been generated from a sub-wavelength aperture by adding a metallic circular grating structure in front of the aperture (Li et al., 2009). Such imperfect Bessel beams find multiple applications, e.g. in optics for laser inscription of patterns deep into transparent materials, or for etching of deep narrow holes in laser manufacturing of opaque materials, among others (Duocastella et al., 2012; Matsupka et al., 2006; Fahrbach et al., 2011).

In acoustics, Bessel beams of sound waves were also reported (Hsu et al., 1989a; Lu et al., 1990a), however are still not so broadly applied as in optics, which is perhaps related with the lack of convenient techniques of formation of such kind of acoustic waves. Acoustic Bessel beams have been excited using acoustical axicons (Katchadjian et al., 2010), in analogy to the optical case. However the most convenient way to form acoustic Bessel beams is by using annular transducer arrays (Masuyama et al., 1999). Related theoretical studies include the scattering of Bessel beams by spheres (Marston, 2007b), nondiffracting bulk-acoustic X waves (Salo et al., 1999) or non linearly generated Bessel beams of higher harmonics (Ding et al., 2000a; Cunningham et al., 2000a). More recently, ultrathin planar acoustic metasurfaces by coiling up space have been proposed to generate acoustic Bessel beams (Li et al., 2012).

4.2 Generation of Zero th-order Bessel beams by axisymmetric gratings

The present work proposes and demonstrates a technique for acoustic Bessel-like beam formation using a structure made of concentric tori of circular section, called here rings for simplicity. We show that, under specific conditions, part of a diffracted wave collimates, producing an elongated focus. Moreover, different diffraction orders can result in different elongated foci, as illustrated in Fig. 4.1(b). In the present work we demonstrate the feasibility of this idea by analytical estimations, numerical simulations and experiments. A simple analytical model based on an approach of axisymmetric diffraction gratings is used to estimate the focal positions and the extent of the focal line. Numerical calculations (using finite difference time domain (FDTD) techniques (Taflove et al., 2000)) of acoustic waves propagating through such axisymmetric gratings were used to observe the complete acoustic field. Finally, the experimental verification of Bessel-like beam formation by an axisymmetric grating is reported.

Each element of the concentric ring structure is characterized by two parameters, (*i*) the toroidal radius, r_m and (*ii*) the radius of the tube (circular section), R_m. The rings in the axisymmetric grating have increasing toroidal radii as $r_m = ma$, where a is the separation between rings and m is an element index, as shown in Fig. 4.1 (b). The continuity of the transversal component of the wave vector at the interface between the free propagation medium and a linear diffraction grating with periodicity a, results in diffraction of normal incident plane waves at diffraction angles given by

$$\sin \beta_n = n\lambda/a \tag{4.1}$$

where λ is the wavelength and n is the diffraction order. It is worth noting that approximately half part of the diffracted radiation converges towards the symmetry axis and the other half diverge. Resulting from the converging radiation, as it follows from simple trigonometry considerations, each ring with major radius r_m is mapped to a particular distance along the symmetry axis, given by

$$f_n(r_m) = f_{nm} = \frac{r_m a}{n\lambda}\sqrt{1 - \left(\frac{n\lambda}{a}\right)^2}. \tag{4.2}$$

If the system of concentric rings extends from r_1 (toroidal radius of inner ring) to r_M (radius of outer ring) in the transverse plane, the focal line for the n-th diffraction order will extend approximately from f_{n1} to f_{nM}. In a limiting case of infinitely extended ring structure ($r_1 = 0$, $r_M = \infty$) Eq. (4.2) predicts an infinitely extended focus, similarly to that of an ideal Bessel beam.

First, we perform numerical simulations in order to explore the character of the elongated focal line (also different foci) due to the axisymmetric diffraction. For

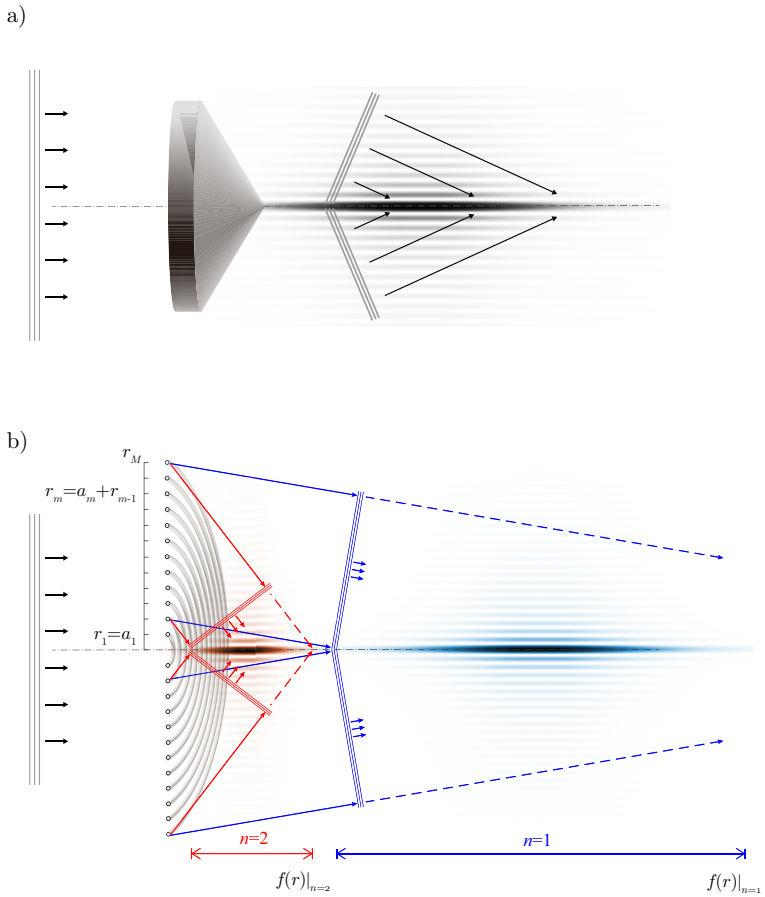


Figure 4.1: Illustration of the formation of Bessel beam by an axicon resulting in imperfect Bessel beam showing a focus-line of finite extent; (b) Illustration of the formation of Bessel-like beams by a plane of concentric rings, where converging diffracted waves result in two elongated foci.

that, we use a structure composed by a set of 50 concentric rings with constant minor radius $R = a/3$, irradiated by a plane wave. We notice that this structure is much larger than that used in experiments (detailed below), therefore, the Bessel-like features of focal line are more pronounced. For the numerical simulations we calculate the wave propagation using the FDTD technique considering an incident plane wave of unity amplitude, $|p_0| = 1$ Pa. Figures 4.2 (a) and 4.2 (b) represent the frequency dependence of the on-axis amplitude and radial far field amplitude respectively. Color map represents the amplitude of the acoustic field, $|p|$, and continuous lines in Fig. 4.2 (a) show the predictions from Eq. (4.2) for the cases $m = 1$ and $m = 50$ for the first three diffraction orders, $n = 1, 2, 3$. The focal spots appear at normalized frequencies $a/\lambda = n$, so the diffraction an-

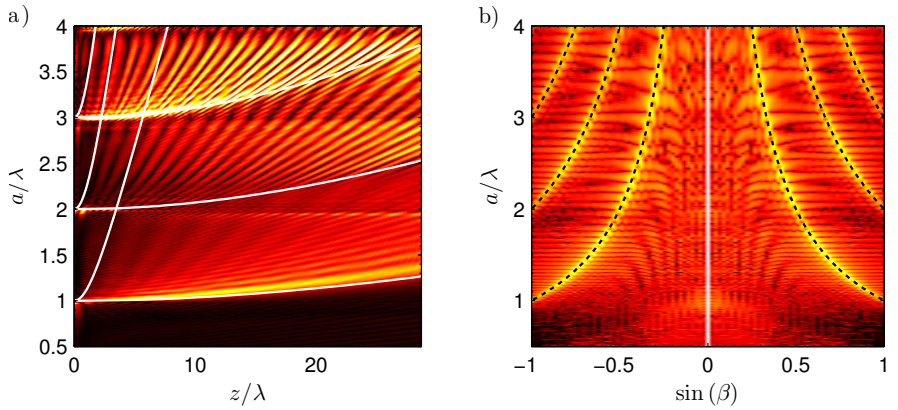


Figure 4.2: Map of acoustic pressure along the symmetry axis (horizontal axis) for varying frequency (vertical axis). Analytical estimations from Eq. (4.2) of focal line extent from f_{n1} to f_{nM} are shown by solid white lines.

gles at these frequencies corresponds to $\beta_n = \pi/2$ ($\sin\beta_n = 1$). With increasing frequency, as shown in Fig. 4.2 (a), foci elongate corresponding to analytical estimations by Eq. (4.2) (white lines in Fig. 4.2 (a)). The diffraction angle decreases with the increasing frequency. Concerning the angular far field distribution shown in Fig. 4.2 (b), excellent agreement between theory (Eq. 4.1) and numerical results are observed, where the characteristic rings appear in the far field pressure distribution. Different maxima appear due to different diffraction order, as a consequence of the focusing effect at near field due to the finite size of the structure, in agreement with Fig. 4.2 (a).

Next, we analyze the acoustic field behind the axisymmetric grating for a particular frequency corresponding to $a = 1.033\lambda$. We study here the case when only one focal line appears. Fig. 4.3 (a) shows the field distribution on axial cross-section. The focus is substantially long, which is a signature of a Bessel-like beam. The latter is proven and illustrated in Fig. 4.3 (b), where the transverse field profiles at the indicated distance behind the ring structure is plotted and compared with Bessel function.

Finally, Fig. 4.4 shows the intensity distribution along the symmetry axis for two different frequencies: important to note that the intensity increases with distance until a maximum focusing distance, where it drops. The scattered energy is proportional to the area between neighbouring rings. Henceforth, the acoustic intensity along the focus increases with a linear trend overlaid of stray oscillations from f_{n1} to f_{nM}, as shown in Fig. 4.4. These oscillations are mainly due to the finite size of the structure: the edges of the diffraction grating result in fringes. The linear dependence of acoustic intensity along the focus is however modified if the thickness of the rings depends on their radius (see the experiments below). Moreover, the transmission efficiency of the structures is high as shown

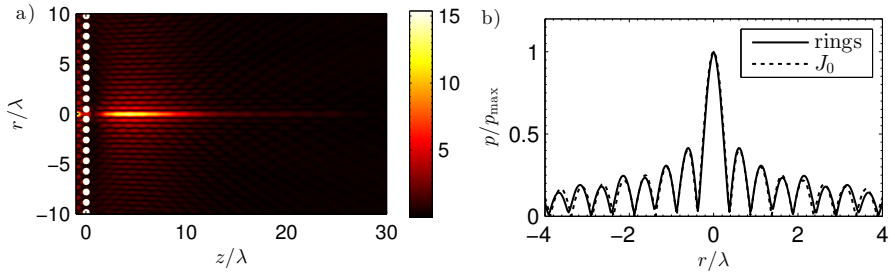


Figure 4.3: 2D pressure distribution for case of single focus ($a = 1.03\lambda$) on a cross section along the symmetry axis. (i) Inset shows axial cross-section of the pressure field at a distance $z = 5\lambda$ (solid black) compared with Bessel beam (solid gray).

in Fig. 4.4, with a gain of amplitude $g = |p|/|p_0| = 12.5$ for $a/\lambda = 1.17$ (red line) and of $g = 9.76$ for $a/\lambda = 1.63$ (blue line). We also note, that although the focal lines associated with different diffraction orders partially overlap, the radiation due to higher order diffraction clearly dominates in the interference picture being the higher diffraction order presenting the biggest gain (see maximum values in Fig. 4.2 (a)).

4.3 Experimental validation

For the experimental validation we designed a system composed by a set of 7 concentric rigid rings embedded in air. The rings are made of methyl methacry-

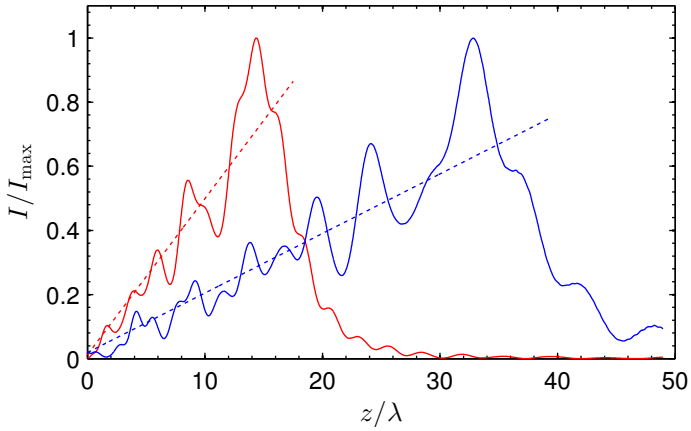


Figure 4.4: On-axis intensity for the cases $a/\lambda = 1.17$ (red line) and $a/\lambda = 1.63$ (blue line). Dashed line is an eye-guide to show the linear dependence.

late (plexiglass), which acoustic impedance is much larger than that of the air ($Z_{plexiglass}/Z_{air} \sim 6000$); therefore, they can be considered acoustically rigid. The variation of the toroidal radius in the structure is $r_m = ma$, where $a = 4$ cm. The minor radius now is a function of the major radius, $R(r_m)$, following a hyperbolic secant profile like in the axisymmetric gradient index lens analyzed in Ref. (Romero-García et al., 2014). This profile slightly modifies the linear dependence of the intensity along the focus because of the changing of the area between the different tori. The hyperbolic secant used here increases the intensity of the components at the end of the foci because the area between the external tori is bigger than the area between the inner tori. In the same way, if the profile is inverted, i.e. the area is bigger between the inner tori, then the near components are increased. Therefore, as we want to show the elongated focus produced by these structures, we use the hyperbolic secant profile with decreasing R with r_m, in order to increase the far components. This profile produces clearer and better reproducible diffraction pattern with smaller number of concentric rings. All measurements were performed in anechoic chamber to avoid unwanted reflections. The source was a loudspeaker radiating a sound wave with a white noise spectrum placed at 1.5 m in front of the plane of concentric rings, a sufficient distance in order to ensure that a nearly plane wave radiates the structure at the frequencies of interest. A movable microphone located behind the structure recorded the transmission spectrum. The experimental set-up is shown in Fig. 4.5 (a).

The quantitative study of Bessel-like beam formation is summarized in Figs. 4.5(b) and 4.5(c). Pressure color maps of Figs. 4.5(b) and 4.5(c) show the numerical and experimental frequency dependence of the on-axis amplitude produced by the used structure. In the experiment, we were able to measure frequencies until 20 kHz ($\frac{a}{\lambda} < 2.3$), i.e. we could achieve Bessel beam formation by the first diffraction order only. The expected dependence of the focal distance on frequency (compare with Fig. 4.4) is also evident in both numerical and experimental plots.

We have also measured field cross-sections: an horizontal plane containing the symmetry axis (see Figs. 4.6 (a-d)) as well as several axial cross-sections (see Figs. 4.6 (e-j)). We focused on two particular frequencies, 10 kHz ($a/\lambda = 1.17$) and 16 kHz ($a/\lambda = 1.88$) (indicated by white dashed-dotted horizontal lines in Figs. 4.5(b) and 4.5(c)). For the analyzed structure the frequency of 10 kHz is close to the condition $a/\lambda = 1$, consequently, the first diffraction spot appears just behind the structure (see white dashed line in Fig. 4.5(c) as a reference). However, the frequency of 16 kHz produces the elongated focus or Bessel-like beam. These two phenomena are both numerically and experimentally shown in Figs. 4.6(a)-(c) and Figs. 4.6(b)-(d) with good agreement.

In order to see the symmetry quality of the beams produced experimentally, we have also measured the axial cross-sections of the pressure field at different z-positions for above discussed cases of 10 kHz and 16 kHz (Fig. 4.6(e)-(j)). In both cases (i) the diffracted pattern is highly axisymmetric and (ii) the diffracting broadening of the central beam, along the extended focus, is almost negligible.

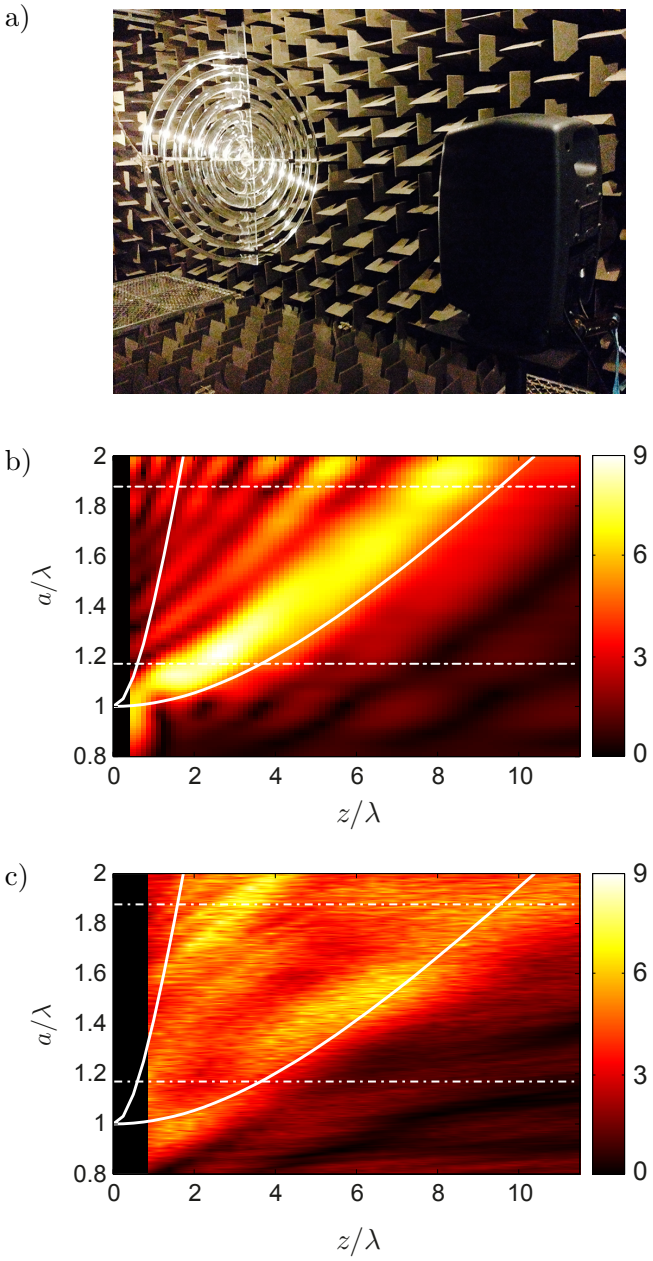


Figure 4.5: (Color online) (a) Experimental set-up. (b) Numerically calculated and (c) experimentally measured maps of on-axis amplitude dependence for varying frequency (vertical). Solid white lines indicate the extend of the focal line from analytical estimations using Eq. (4.2) for $f_1(r_1)$ and $f_1(r_7)$. Dashed white lines represent the frequencies shown in Fig. 4.6

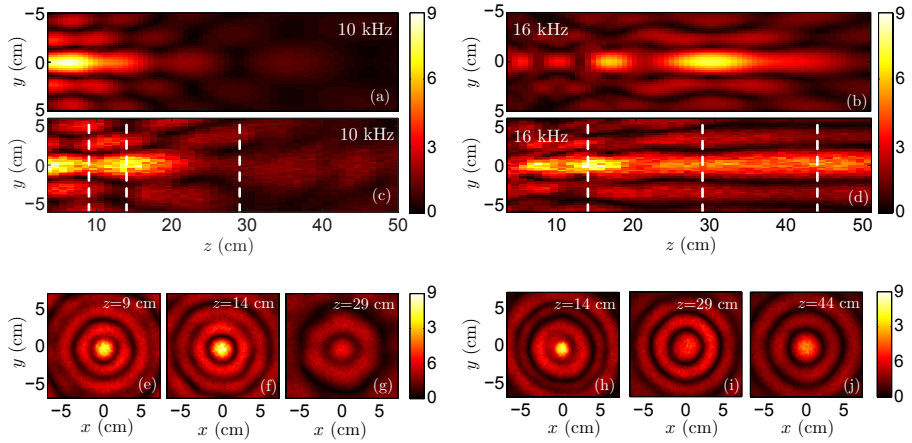


Figure 4.6: (Color online) (a-d) Amplitude distributions in planes along the symmetry axis $r(z, x)$ obtained by numerical simulations (a, b) and experimental (c, d) measurements for two different frequencies, showing the formation of elongated foci. Experimental transversal amplitude cross-sections (x, y) at different distances behind the ring structure, showing the formation of the Bessel-like beam. (e-g) correspond to the experimental transversal planes at 10 kHz marked with dashed lines in (c). (h-j) correspond to the experimental transversal planes at 16 kHz marked with dashed lines in (d).

The transversal profiles in Figs. 4.6(e)-(j) also illustrate the typical shape of the truncated Bessel function. It is simple to predict the tendencies of the amplitude distribution along the focus for such a small number of rings. The longitudinal shape along the elongated focus seems to be not linearly increasing/sharply dropping, but correspondingly smoother. This is due to the small number of rings in the structure; also due to the difference in thickness of the rings.

4.4 Conclusions

Concluding, we have demonstrated the principle of Bessel-like focusing in a system of concentric rigid rings. Although the size of experimental system was reduced (to 7 rings), the main properties of the Bessel beam formation were demonstrated: the elongated foci along the symmetry axis, the Bessel-like distributions of the field in axial cross-sections, and the expected dependence of the focal distance with the frequency. The Bessel beam formation can be substantially improved, as follows from numerical calculations with larger number of rings.

For technical applications, the Bessel beam formation can be modified and improved, according to specific needs, by some means as for example: (i) the use of not toroidal rings, but rather the ones with more sophisticated shapes, which would favor the converging part of the diffracted wave (i.e. to convert into Bessel

beams nearly all radiation (note that the rings can converge as maximum the half of initial radiation); (*ii*) the use of a ring structure of adequate thickness which would allow tailoring the longitudinal profile of the focus, according to the requirements; (*iii*) modifying the radii of the rings (making the radii incrementing not linearly) which is another parameter allowing the engineering of the focusing, and allowing to optimize the focal structure; finally (*iv*) by using multiple layers of rings at equidistant separations along the symmetry axis one could not only enhance the effect, but also introduce another possibility of tailoring the focal spot, as the interference from different planes will come into play.

References

Chu, X. (2012). "Analytical study on the self-healing property of Bessel beam". In: *Eur. Phys. J. D* 66, p. 259.

Cunningham, Kevin B. and Mark F. Hamilton (2000a). "Bessel beams of finite amplitude in absorbing fluids". In: *J. Acous. Soc. Am.* 108, p. 519.

Ding, D. and J. y. Lu (2000a). "Higher-order harmonics of limited diffraction Bessel beams". In: *J. Acous. Soc. Am.* 107, p. 1212.

Duocastella, M. and C.B. Arnold (2012). "Bessel and annular beams for material processing". In: *Laser Photonics Rev.* 6, p. 607.

Durnin, J. (1987). "Exact solutions for nondiffracting beams. I. The scalar theory". In: *J. Opt. Soc. Am. A* 4, p. 651.

Fahrbach, F.O. and A. Rohrbach (2011). "Propagation stability of self-reconstructing Bessel beams enables contrast-enhanced imaging in thick media". In: *Nat. Commun.* 3, p. 632.

Hsu, D.K., F.J. Margetan, and D. O. Thompson (1989a). "Bessel beam ultrasonic transducer: fabrication method and experimental results". In: *Appl. Phys. Lett.* 55, p. 2066.

Katchadjian, P., C. Desimone, and A.D. Garcia (2010). "Application of Axicon Lenses in Ultrasonic Techniques". In: *AIP Conf. Proc.* 1211, p. 1043.

Li, Yong, Bin Liang, Zhong ming Gu, Xin ye Zou, and Jian chun Cheng (2012). "-". In: *Sci. Rep.* 3, p. 2546.

Li, Zhaofeng, Kamil Boratay Alici, Humeyra Caglayan, and Ekmel Ozbay (2009). "Generation of an Axially Asymmetric Bessel-Like Beam from a Metallic Subwavelength Aperture". In: *Phys. Rev. Lett.* 102, p. 143901.

Lu, J. and F.J. Greenleaf (1990a). "Ultrasonic nondiffracting transducer for medical imaging". In: *IEEE Trans. Ultrason. Ferroelec. Freq. Contr.* 37, p. 438.

Maddox, J. (1987). "Making Light Spots travel further". In: *Nature* 327, p. 183.

Marston, Philip L. (2007b). "Scattering of a Bessel beam by a sphere". In: *J. Acous. Soc. Am.* 121, p. 753.

Masuyama, Hiroyuki, Tomoki Yokoyama, Keinosuke Nagai, and Koichi Mizutani (1999). "Generation of Bessel Beam from Equiamplitude-Driven Annular Transducer Array Consisting of a Few Elements". In: *Jpn. J. Appl. Phys.* 38, p. 3080.

Matsupka, Y., Y. Kizuka, and T. Inoue (2006). "The characteristics of laser microdrilling using a Bessel beam". In: *Appl. Phys. A-Mater.* 84, p. 423.

McLeod, Euan, Adam B. Hopkins, and Craig B. Arnold (2006). "Multiscale Bessel beams generated by a tunable acoustic gradient index of refraction lens". In: *Opt. Lett.* 31, p. 3155.

McLeod, J. H. (1954). "The axicon: A new type of optical element". In: *J. Opt. Soc. Am.* 44, p. 592.

Romero-García, V., A. Cebrecos, R. Picó, V. Sánchez-Morcillo, L.M. Garcia-Raffi, and J.V. Sánchez-Pérez. (2014). "Wave focusing using symmetry matching in axisymmetric acoustic gradient index lenses". In: *App. Phys. Lett.* 103, p. 264106.

Salo, J., J. Fagerholm, A. T. Friberg, and M. M. Salomaa (1999). "Nondiffracting Bulk-Acoustic X waves in Crystals". In: *Phys. Rev. Lett.* 83, p. 1171.
Taflove, A. and S.C. Hagness (2000). *Computational Electrodynamics: The Finite-Difference Time-Domain Method*. Artech House, Boston.

Publications

The contents of this chapter have been presented in the following publications:

Journal papers

- **Jimenez, N.**; Romero-García, V.; Picó, R.; Cebrecos, A.; Sanchez-Morcillo, V.; García-Raffi, L.; Sánchez-Pérez, J. V. and Staliunas, K. "Acoustic Bessel-like beam formation by an axisymmetric grating" *Europhysics Letters*, 106, 24005 (2014)



Chapter 5

Nonlinear Focused Beams by Axisymmetric Gratings

Abstract

Previously, we presented the diffraction of waves on axisymmetric uniform gratings can conform a Bessel beam. Here, the spacing between slits is designed in order to provide focusing as in Fresnel Zone Plates. The device presents a very narrow focal spot, that is between the sub-diffraction and the sub-wavelength limits. As common from other Fresnel-like lenses, and also in Bessel beams, the narrow focal is accompanied by high amplitude side lobes. The lens presents high gain, around 30 dB. Thus, nonlinear effects can mainly activated locally at the focal spot. The field of the second harmonic maintain the excellent beam-width of the Fresnel lens, while its side-lobes are strongly reduced. The proposed lens in the weakly nonlinear regime is suitable for second harmonic imaging techniques: the excellent beam spatial resolution of the second harmonic is maintained, while the side-lobe amplitude, responsible of signal-to-noise ratio, is reduced.

5.1 Introduction

Acoustic focusing is an interdisciplinary topic covering a rich set of applied sciences that include nondestructive testing and acoustic microscopy techniques, detection of fish and undersea exploration, ultrasound and elasticity diagnostic imaging or ultrasound therapeutic techniques among others. Particularly interesting is the fact that focusing results in high intensities at a specific location and over only a small volume, triggering nonlinear acoustics effects and enhancing specific mechanical and thermal effects. Mechanical phenomena include cavitation, microstreaming, and acoustic radiation forces while the thermal effects include heat generation due to acoustic energy absorption.

These nonlinear effects are exploited by a broad range of applications. In ultrasound medical applications second harmonic generation is widely used in harmonic imaging techniques as in Tissue Harmonic Imaging (THI) (Averkiou et al., 1997), microbubble cavitation processes are commonly used for increase contrast in ultrasound imaging (Duck, 2002), to induce mechanical interaction with the surrounding tissues in ultrasound-enhanced drug delivery techniques (Bailey et al., 2003) or for noninvasive blood-brain barrier opening using focused ultrasound (Choi et al., 2007). Acoustic radiation forces are exploited to map media elasticity in ultrasound elastography techniques such as in Shear Wave Elasticity Imaging (SWEI) (Sarvazyan et al., 1998), Acoustic Radiation Force Impulse imaging (ARFI) (Nightingale et al., 2002), Harmonic Motion Imaging (HMI) (Konofagou et al., 2003) or in Supersonic Shear Imaging (SSI) (Bercoff et al., 2004). Moreover, at high intensities nonlinearity increase energy deposition rate, that is exploited in High Intensity Focused Ultrasound (HIFU) for enhancing thermal ablation (Bailey et al., 2003). Finally, in the case of Shock Wave Lithotripsy (SWL) acoustic pulsed-shock waves are focused to produce high-amplitude localized shear stresses and induce calculus fragmentation, as widely used for kidney stone treatments (Bailey et al., 2003). In all of these techniques, the design of devices to easily manage the focusing properties and the enhancement of the focal gain is of pivotal importance.

Acoustic focusing can be achieved by arrays of transducers where the beam focusing and steering can be controlled actively, where its focusing performance is limited by the number of active channels. It is attractive the design of passive acoustic focusing devices in order to reduce costs.

Generally, there are four main different procedures to generate strongly focused acoustic field by passive devices: by optimizing the geometry of the transducer, by using refraction lenses, by using reflective systems or by using diffraction gratings. The most common approach is to use curved shaped radiation surfaces. These can be made by curved bowl single element piezoelectric transducers, but also from different arrangements of small plane transducers distributed over a curved surface and excited in-phase. Curved acoustic lenses made of different refraction

index material are also common, as long the lens is also used as an impedance matching layer between the active element, and the surrounding media. However, the transmission efficiency of these lenses is strongly reduced because the contrast of refraction index between the lens and the surrounding media is remarkable. On the other hand, focusing can be achieved by curved reflectors, e.g. elliptic reflectors in SWL. Due to the low dispersion of the acoustic media, all these focusing devices based on refraction, and also based on reflection of curved surfaces, present the feature that focusing does not strongly depends on frequency and therefore are suitable for impulsive excitations. However, in these devices, in which the focal sport is limited by the diffraction limit (Rayleigh criterion), the focal size is larger than one wavelength, i.e. the focal resolution is bigger than the sub-wavelength regime.

The last group of passive devices to generate strongly ultrasound focusing is based on the diffraction grating. The diffraction of waves on flat grating plates have been proposed as acoustic analogues of the Fresnel Zone Plates (FZP) (Farnow et al., 1974; Sleva et al., 1994; Schindel et al., 1997; Wang et al., 2008). As in optics, acoustic Fresnel Zone Plates consist of alternating rigid (opaque) and open (transparent) annuli. The radius and width of the open annuli are specially designed to only transmit the waves that constructively interferes at focus, while the radiation that destructively interferes is blocked by the rigid annuli. There exist other approaches that exploit the diffraction over concentric ringed-shaped structures to achieve focalization. These include axisymmetric gratings based on Fresnel Zone Plates in which the area of the annuli is not equal for opaque and transparent zones (Clement et al., 2015) or acoustic Fresnel lenses that exploit resonances to enhance the transmission (Molerón et al., 2014).

It is worth noting here that the diffraction grating over equally spaced toroidal scatters, as those presented in Chapter 4, can generate Bessel beams at the axis (Jimenez et al., 2014). This approach is roughly equivalent to the Bessel beams created by annular piezoelectric annuli (Hsu et al., 1989b). A characteristic feature of Bessel beams is that the transverse beam-width can be reduced below the sub-wavelength limit. However, these beams present also high amplitude side-lobes. Thus, when used for imaging, these devices provides high spatial resolution but low signal-to-noise (S/N) ratios (Lu et al., 1990b).

As soon as high amplitudes are applied to these focusing devices, it is well-known that the second harmonic field is generated mainly around the focal spot due to the local activation of the nonlinear response of the media. The focus of the second harmonic has reduced side-lobes as long the nonlinear processes are mainly activated at the focal spot (Duck, 2002). In the case of ideal Bessel beams, it has been observed a reduction of half intensity of the side-lobe amplitude for the second harmonic component (Ding et al., 1996), while its transverse profile is reduced to the half, i.e. exactly maintain its narrowness if normalized to the wavelength (Ding et al., 2000b). These effects have been also observed in more realistic configurations including absorption (Cunningham et al., 2000b) and limited

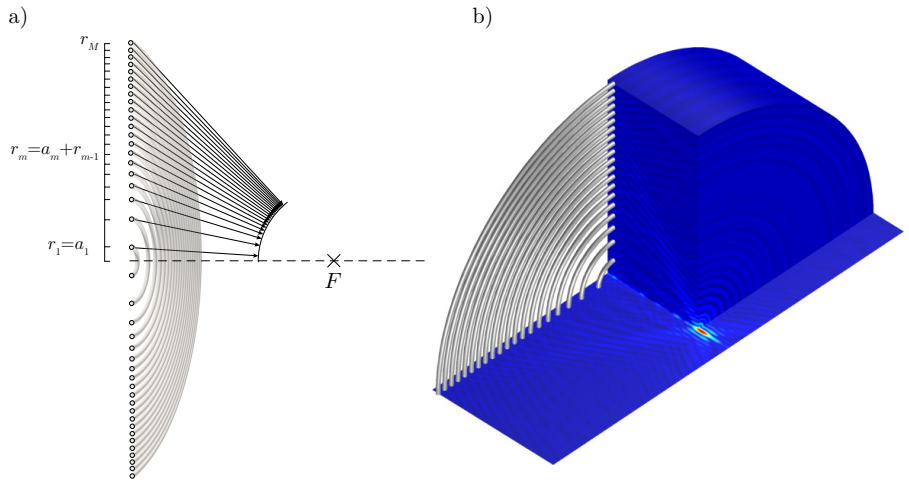


Figure 5.1: (a) Scheme of the passive focusing device composed of concentric rings. (b) Simulation example of focusing by this device.

aperture Bessel beams (Holm et al., 2010). Recently, the reduction of side-lobes of second harmonic has been observed for a focused Fresnel field, where the focalization, instead of passive lenses, has been achieved by active Fresnel beamforming in the context of second harmonic imaging (Nguyen et al., 2014).

In this Chapter, we present the acoustical focusing properties of an axisymmetric diffraction grating in both the linear and the nonlinear regime. We show that in the linear regime the system presents a focal spot in the sub-wavelength regime with high gain, around 30 dB, with relative high amplitude side-lobes. Interestingly, nonlinear effects can be excited locally mainly at the sharp focal spot. Thus, in the nonlinear regime the high intensity at the focal spot activates the harmonic generation, producing a focus of the second harmonic with particular spatial features. Mainly, second harmonic beam-width is between sub-diffraction and sub-wavelength limits, but having strongly reduced lateral lobes.

We demonstrate these results by analytical estimations, numerical simulations and experiments. A simple analytical model based on an approach of axisymmetric diffraction gratings is used to estimate the focal positions and the extent of the focal spot. Numerical calculations (using finite-difference time domain (FDTD) techniques (Botteldooren, 1995)) of acoustic waves propagating through such axisymmetric gratings were used to observe the complete acoustic field in both the linear and the nonlinear regime. The experimental verification of the theoretical prediction is also reported showing very good agreement with the theory.

5.2 Axisymmetric diffraction grating design

We consider M concentric toroidal scatterers of minor radius R and major radius r_m with $m = 1, ..., M$. A detailed scheme is presented in Fig. 5.1 (a). A plane wave radiates the axisymmetric grating and as a consequence it is scattered. We consider that R is small in comparison to the wavelength of the incident wave, in such a way that each scatterer can be considered as a point source. Then, in order to have an optimal superposition at a given focal point, F, behind the axisymmetric grating, all the incoming waves should arrive precisely in phase to F. This suggests an ideal axisymmetric grating would consist of a series of infinitesimal toroidal scatterers located in a plane at radial distances given by the geometric focal law

$$r_{m+1}^2 = r_m^2 + n\lambda\left(n\lambda + 2\sqrt{r_m^2 + F^2}\right), \tag{5.1}$$

where n indicates the diffraction order of the axisymmetric diffraction grating. Equivalently, given the distribution of toroidal scatterers, r_m, the focal position can be determined by the following expression,

$$F = \sqrt{\left(\frac{r_{m+1}^2 - r_m^2}{2n\lambda} - \frac{n\lambda}{2}\right)^2 - r_m^2}. \tag{5.2}$$

Here, it is important to note the relation of Eq. (5.1) to the standard Fresnel Zone Plate. As explained above, FZP consist in alternating opaque and open annuli. The location of the edges for the m zone is given by

$$r'_m = \sqrt{\left(\sqrt{r_0 + F^2} + m\frac{\lambda}{2}\right)^2 - F^2}. \tag{5.3}$$

The location of the center of each annuli in the standard FZP is given by (Clement et al., 2015)

$$r_m = \sqrt{\left(\sqrt{r_0 + F^2} + m\lambda\right)^2 - F^2}, \tag{5.4}$$

which gives same radial distribution of the toroidal rings as the succession obtained by diffraction grating in Eq. (5.1) if the proper first toroidal radius is matched for both lenses. On the other hand, in the work of Clement et al. (2015) they study a lens formed by slits of different thickness located at r_m, while in the present work we used rigid scattered located at r_m. Following Babinet's principle considerations, both approach can be considered equivalent.

Figure 5.1 (b) presents a simulation example of the focalization. As long the separation between the external rings is about one wavelength, it can be seen qualitatively the focusing of the system, the focal spot and the good spatial resolution

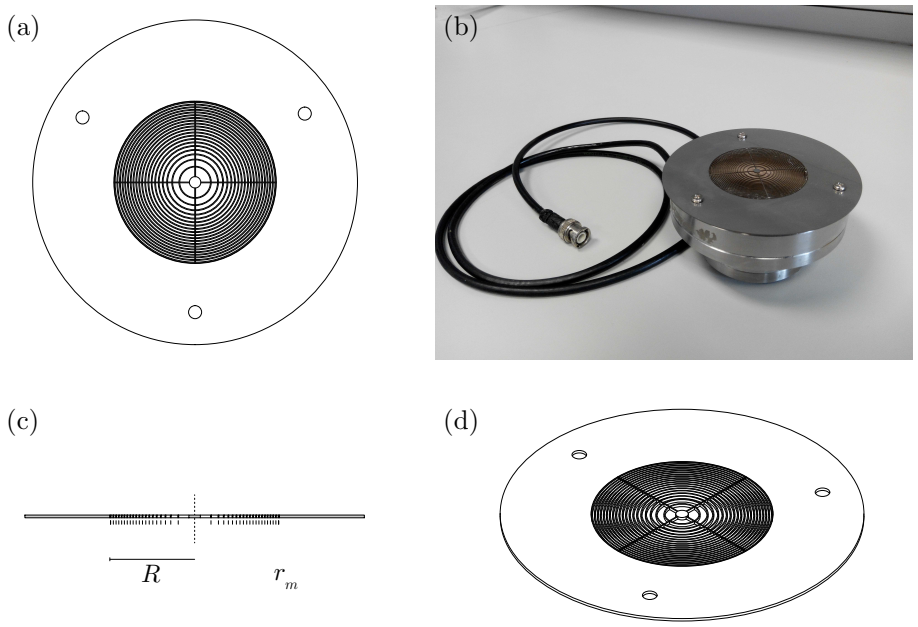


Figure 5.2: (a,c,d) Design of the axisymmetric grating plate. (b) Image of the constructed grating mounted over a plane piezoelectric transducer of 50 mm aperture.

compared to the wavelength. In the following sections a further analysis of the focusing quality of this design is presented.

5.3 Small amplitude focusing

An experiential test was performed in order to validate model results. Following the design Eq. (5.1), an axisymmetric grating was designed by using a focal distance of $F = 15$ mm and focal frequency $f_0 = 2.29$ MHz. The passive system was fabricated by laser cutting over a stainless steel plate of 0.8 mm thickness. Figures 5.2 (a,c,d) show a scheme of the axisymmetric grating. The minor radius of the toroidal scatterers was $R = 0.75$ mm (solid parts). The number of rings was $M = 21$ and the grating total radius was $r_M = 25$ mm.

The axisymmetric grating lens was placed in front of an ultrasound plane transducer as shown in Fig. 5.2 (b). This source was formed by a plane single element piezoceramic crystal (PZ 26, Ferroperm Piezoceramics, Denmark) mounted in a custom designed steel housing with aperture $R = 25$ mm, matching the area of the grating. The separation distance between the grating and the source plane was adjusted to 0.5 mm.

The assembled grating-transducer system was immersed in a degassed and distilled water tank of $350 \times 350 \times 350$ mm^3, the temperature of which during the measurements was constant at 26 °C. The source was driven with a sinusoidal sweep burst ranging from frequency $f_{\min} = 1$ MHz to $f_{\max} = 3$ MHz and 50 cycles using a function generator (14 bits, 100 MS/s, model PXI5412, National Instruments) and a linear RF amplifier (ENI 1040L, 400W, 55dB, ENI, Rochester, NY). The pressure waveforms were acquired with a HNR 500 μm needle PVDF hydrophone (Onda Corp, CA), and a digitizer (64 MS/s, model PXI5620, National Instruments) were used. A three-axis micropositioning system (OWIS GmbH, Germany) was used to move the hydrophone in three orthogonal directions with an accuracy of 10 μm and a National Instruments PXI-Technology controller NI8176 was used to control all the devices. The amplitude frequency response of the hydrophone was compensated in post-processing.

In addition to measurements, we perform numerical simulations in order to explore the linear character of the designed axisymmetric diffraction grating. For the numerical simulations we calculate the wave propagation using the FDTD technique considering an incident plane wave of unity amplitude, $p_0 = 1$ Pa. From

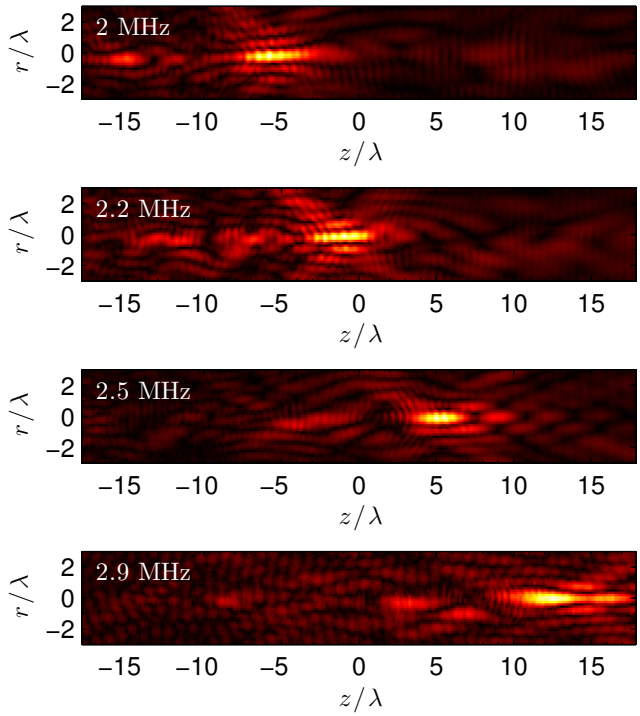


Figure 5.3: Field distribution for four different frequencies obtained by the experiment. It can be seen how the focal spot displaces in the axial location.

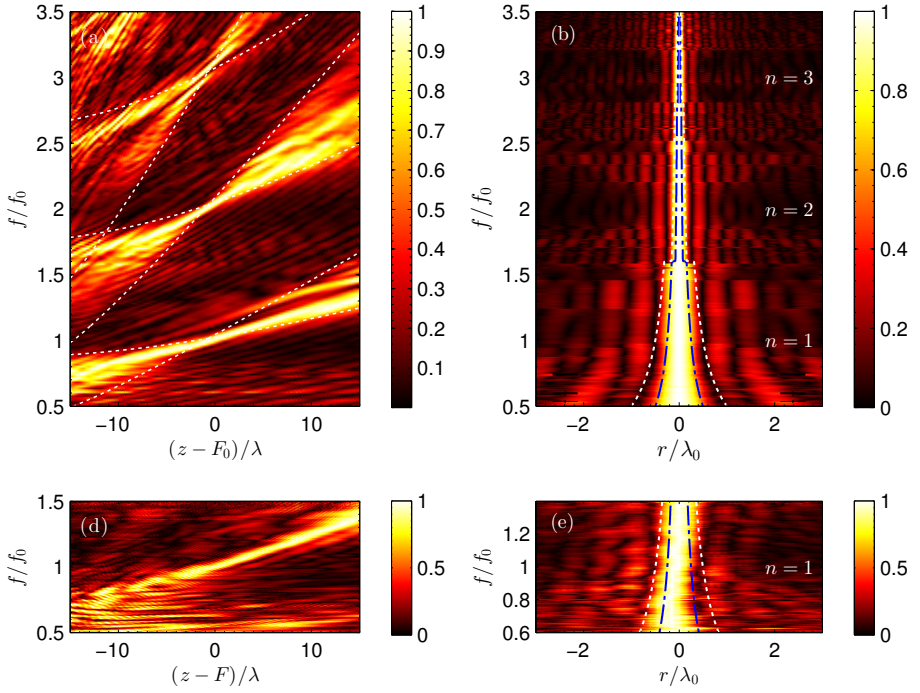


Figure 5.4: On axis field distribution as a function of frequency obtained by (a) simulation and (c) experiment. White lines indicates theoretical focus by using Eq. (5.2). Transverse field distribution measured at the focal spot axial distance as a function of frequency obtained by (b) simulations and (d) experiment. White lines mark the sub-wavelength and blue lines the sub-diffractive limit.

now we will show the results in normalized units. Distances will be normalized with respect to the wavelength, λ, and in the case of the distances in the symmetry axis will be referred to the focal distance F; frequencies will be normalized to the design frequency, f_0.

Figure 5.3 shows the experimental pressure distribution for different frequencies around the design frequency $f_0 = 2.229$ MHz. It can be seen that a sharp focusing is observed for the design frequency. Furthermore, if frequency is modified the focal position displaces in the axial direction according to Eq. (5.2). In these cases, some focus aberration appears as long the design model holds exact only for the design frequency (Fig. 5.3 (b)). However, the focal spot maintains its shape and focusing properties for a reasonably bandwidth that we will study in the following sections.

The axial pressure distribution as a function of frequency is presented in Fig. 5.4 (a) for the simulations and Fig. 5.4 (c) for the experiment. Note that, due to the finite bandwidth of the ultrasonic source, in the experimental measurements

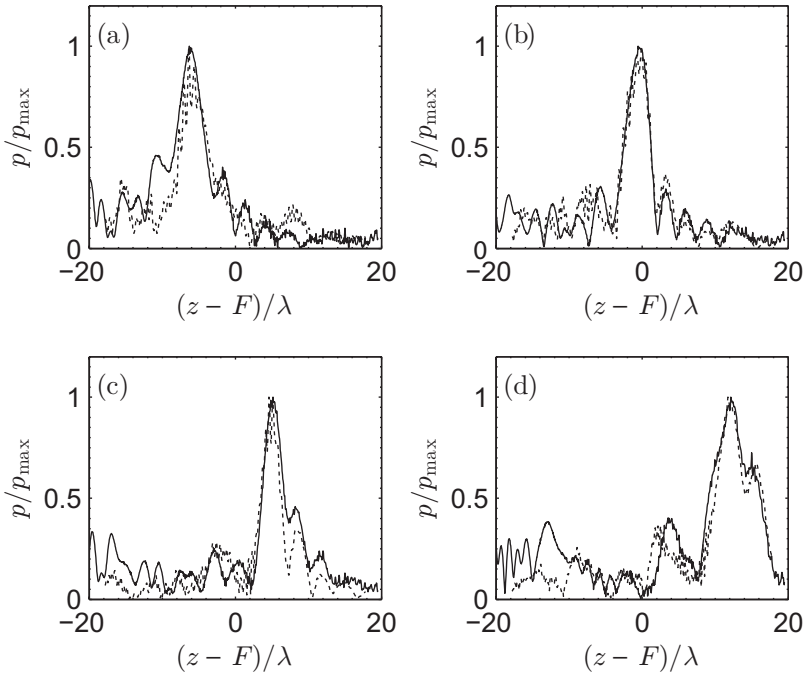


Figure 5.5: (a-d) On-axis pressure measured for the frequencies $f = 2, 2.2, 2.5, 2.9$ MHz respectively obtained by (doted lines) experiments and (continuous lines) simulations.

the characterization is restricted to a frequency range covering the first diffraction grating mode, i.e., $n = 1$, while in the simulations the characterization is extended for frequencies covering up to $n = 3$ diffraction orders. White dotted line represents the curves obtained from Eq. (5.2) for two different pairs of m, ($m = 1$ and $m = 21$), the crossing of this line represents the focal point. The agreement with the numerical simulation is very good. Moreover, one can see that although the lens is designed to focus waves in the point F at frequency f_0, the lens produces a focal shift with frequency giving the possibility to manage the position of the focus with frequency. However, as we will see later, the gain at focal spot changes considerably with frequency. Finally, we notice that as we increase frequency in the simulations new focal spots are generated for the higher diffraction grating orders. according to Eq. (5.2).

Figures 5.4 (b, d) represents the radial distribution of the normalized acoustic field at the position of the focal spot: Fig. 5.4 (b) shows the simulation while Fig. 5.4 (d) shows experimental results. Figures 5.4 (a, c) represents the equivalent radial distribution to the results of Figs. 5.4 (b, d) respectively. We can observe a main lobe aligned with the center of the axisymmetric lens. Secondary smaller lobes also appears. We also represent the the theoretical Full Width at Half Maximum (FWHM) corresponding to (dotted white lines) sub-wavelength ($< \lambda$) and

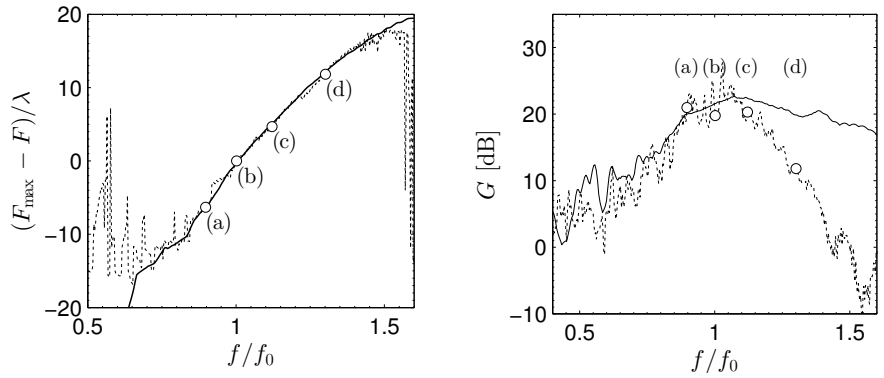


Figure 5.6: (Left) Location of the focal obtained by (dotted lines) experiments and (continuous line) simulations. (Right) Gain value obtained by (dotted lines) experiments and (continuous line) simulations. Markers (a-d) corresponds to the frequencies $f = 2, 2.22.5, 2.9$ MHz respectively.

(dashed blue lines) subdiffractive ($< \lambda/2$) limits respectively. At first glance, we can observe that in both, simulations and experiments, the width of the focal spot between the sub-diffractive and sub-wavelength regime, overcoming the diffraction limit. A deeper analysis is presenter later.

In order to see the agreement between experiments and theory, we have plotted in Fig. 5.5 the longitudinal cuts of the normalized acoustic pressure for the cases $f = 2, 2.2, 2.5, 2.9$ MHz, in the subplots (a-c) respectively. Continuous line represents the numerical predictions while dashed lines show the experimental results. Good agreement is seen in all cases, where again it can be seen how the focal spot is shifted in axial direction for increasing frequencies. The shifting of the focal position can be seen in detail in Fig. 5.6 (left), where it is represented the location of the peak pressure for the (continuous line) simulations and (dashed lines) experiment. Excellent agreement is observed between them. The frequencies corresponding to $f = 2, 2.2, 2.5, 2.9$ MHz, are marked as the points (a-c).

In order to evaluate the focusing capability of the axisymmetric grating we are discussing in this work, we have analyzed the gain of the lens evaluating the expression $G = 20 \log (|p_{\max}|/|p_0|)$ [dB], where $p_{\max}$ is the pressure at the focal point and $|p_0|$ is the incident wave pressure amplitude. Figure 5.6 (right) shows the gain numerically evaluated (continuous line) and experimentally measured (dotted line). For the design of this lens with $M = 21$ scatterers, the gain is 20 dB. We notice that this gain is constant around $f/f_0 = 1$, so the focusing properties of the axisymmetric lens is robust in terms of frequency, i.e., it is insensitive to possible errors in frequency around $f/f_0 = 1$.

Figure 5.7 (left) goes further and shows a general overview of the gain of a lens designed with the Eq. (5.1) as the number of toroidal scatterers, M is increased.

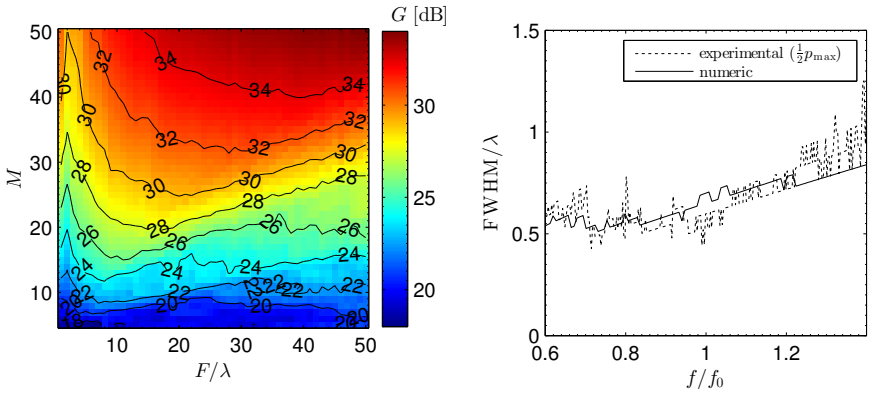


Figure 5.7: (Left) Simulated gain value measured at the design frequency for different gratings, as a function of the number of rings, M, and the design focal distance, F. (Right) Full Width at Half Maximum (FWHM) obtained by (dotted lines) experiments and (continuous line) simulations, measured at the half pressure.

By using double number of toroidal scatterers, $M = 42$, the gain of the system can be increased to 34 dB. We notice that this amount of gains are competitive with the usual systems used in high intensity focused ultrasound (Canney et al., 2008), but note we can achieve these values for very short distances. It is worth noting here that we can achieve these high gains at very short focal distances, of the order of wavelength. This property is almost impossible with with other common passive devices due to geometrical limitations. A further discussion is reported in the Conclusions section.

Finally, we have analyzed the Full Width at Half Maximum (FWHM) of the radial dimensions of the focal spot in the whole range of frequencies. Figure 5.7 (right) shows the (continuous line) numerical predictions and the (dotted line) experimental results for the FWHM. The axisymmetric lens presented in this work, shows a sub-wavelength full width at half maximum, i.e., FWHM $< \lambda$, for the whole range of analyzed frequencies. We also calculated the FWHM evaluated from the intensity data, i.e. the with of the spot at $p = p_{\max}/\sqrt{2}$. Obviously the width of the focal evaluated by intensity is thinner but the same concussions applies here: the central radial lobe corresponding to the focal spot is always between the sub-wavelength regime and the diffraction limit. This feature can be also observed by the white dashed lines in the maps shown in Figs. 5.4 (b, d).

5.4 Transition from linear-to-nonlinear focusing

Now we start the study of the transition from the linear- to the nonlinear focusing of the axisymmetric grating by increasing the amplitude of the incident plane wave. The piezoelectric transducer is excited with an amplitude in which its behavior can be considered linear in the range of frequencies from $0.5f/f_0$ to $1.5f/f_0$. In this range of frequencies we reproduce the same acoustic pattern as in the linear (small amplitude excitation) regime showing the focal spot at $f/f_0 = 1$ and at $z = F$, as shown in Fig. 5.8 (a). However, now we can clearly see that the focal spot has contributions fro the double frequency $f/f_0 = 2$, i.e., at the second harmonic of the fundamental wave. The high amplitude around the spot generated at frequency $f/f_0 = 1$ activates the harmonic generation due to the nonlinearity of water, activating the contribution from $f/f_0 = 2$ due to the high amplitudes around the focal spot.

The focal spot generated by this nonlinear effect presents a spatial acoustic profile with different properties than the focal spot of the fundamental mode. Because of the local nonlinear generation of this spot, the longitudinal profile presents smaller lobes than in the case of the spot of the fundamental frequency. Figure 5.8 (b) shows the comparison between the experimental longitudinal profile for (continuous line) first harmonic and (dashed line) its corresponding second harmonic.

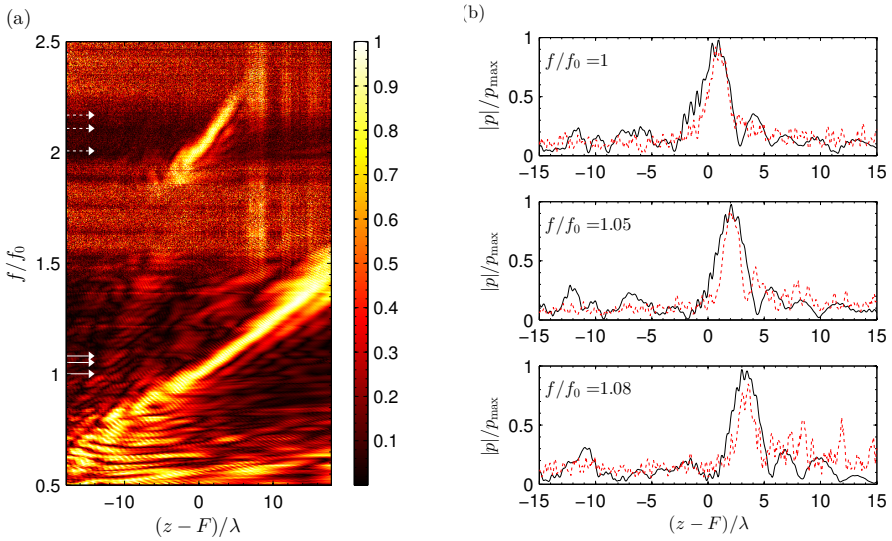


Figure 5.8: Weakly nonlinear experimental measurements of the grating. (a) On-axis field distribution as a function of the frequency. (b) On-axis field distribution for the second harmonic for three frequencies, marked by the arrows in (a). Experiments (Red dotted line) and simulation (continuous line).

5.5 High intensity regime

We explore the high amplitude regime by using nonlinear simulation methods based also in FDTD technique, as used previously in Chapter 3. The simulations assumed perfectly rigid scatters over a cylindrical axisymmetric coordinate system, where the nonlinearity is only present on the bulk of the fluid, in this case we assumed water, with parameters: $\beta = 1 + B/2A = 3.5$, density $\rho_0 = 1000$, sound speed $c_0 = 1500$.

An overview of the device focusing for increasing source amplitude is shown in Fig. 5.9. The source amplitude is expressed as the normalized quantity F/x_s, being $x_s = 1/k\varepsilon\beta$ the shock formation distance with k the wavenumber, ε the acoustic match number and β the parameter of nonlinearity. In Fig. 5.9, we show the axial peak pressure distribution, i.e. the maximum of the nonlinear waveforms, $|p|^+$, and the minimum rarefaction distribution, $|p|^-$. On the other hand, in Fig. 5.10 it is shown the lateral pressure distribution corresponding also to $|p|^+$ and $|p|^-$ for the same range of excitation amplitudes.

The main nonlinear effects in the field distribution in high intensity focused ultrasound can be observed here. The effective gain of the system, the peak value corresponding to $p_{\max}/p_0$, is extraordinary increased from the linear value of $p/p_0 = 39$ (32 dB), to $|p|^+/p_0 = 92$ (39 dB) in the case of very strong nonlinearity. Thus, as peak pressure grows locally at the focus, the focal width stretches in both axial and lateral dimensions. In addition, the relative amplitude between the peak pressure and its lateral lobes is strongly increased.

In Figure 5.11 we illustrate the pressure distribution for 4 different source

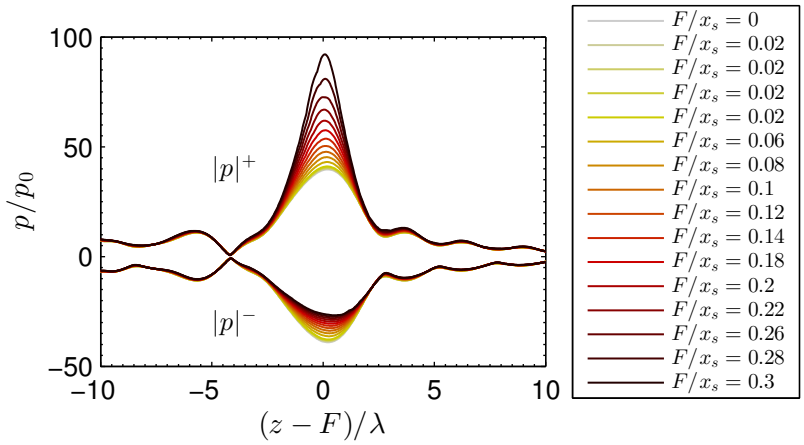


Figure 5.9: Axial simulated pressure profile for the positive envelope ($|p|^+$) and for the rarefaction minimum distribution ($|p|^-$). Different excitation amplitudes are marked as different color lines.

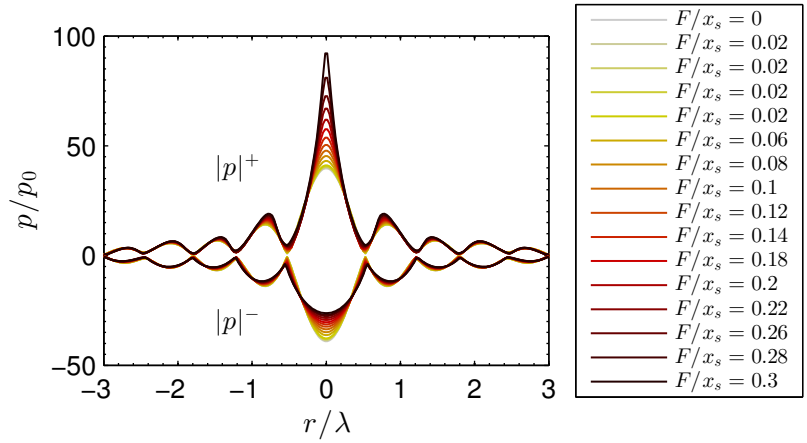


Figure 5.10: Transversal simulated pressure profile for the positive envelope ($|p|^+$) and for the rarefaction minimum distribution ($|p|^-$). Different excitation amplitudes are marked as different color lines.

amplitudes, being $F/x_s = 0.02, 0.16, 0.260.3$ from low to high amplitude. The above described effects can be observed. The axial field distribution corresponding to these amplitudes can be observed in Fig. 5.12, where the amplitude of the first and second harmonic is extracted. It can be seen that the amplitude of the first harmonic is slightly reduced for increasing amplitudes and the second harmonic field grows locally at the focal spot.

The locally nonlinear generation of the higher harmonics contributes to modify the waveform, shown in the corresponding subplots of Fig. 5.12. Here, the characteristic shape of nonlinear focused waveforms can be observed, reaching a peak pressure of $|p|^+ = 126$ MPa and a rarefaction pressures of $|p|^+ = -36$ MPa. These peak pressures are of the order of those used in medical therapy applications for thermal ablation, with the rarefaction pressure close to the cavitation threshold of the water at room hydrodynamic pressure and temperature[1] (Caupin et al., 2006).

[1]Note the cavitation threshold strongly depends of the dissolved oxygen content and bubbles in general of the water.

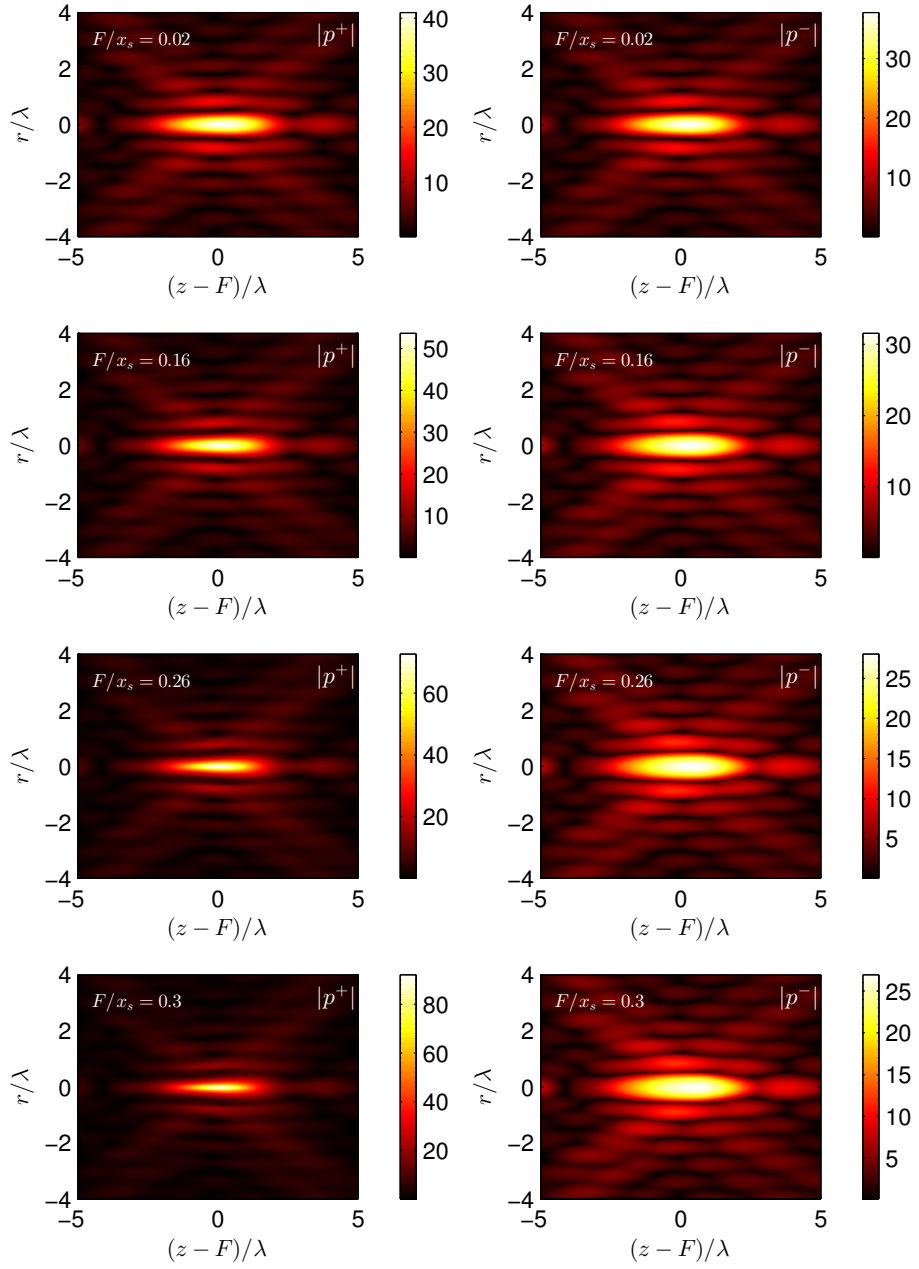


Figure 5.11: Field distribution for increasing amplitude excitation. (Left column) pressure profile for the positive envelope ($|p|^+$) and (right column) for the rarefaction minimum distribution ($|p|^-$).

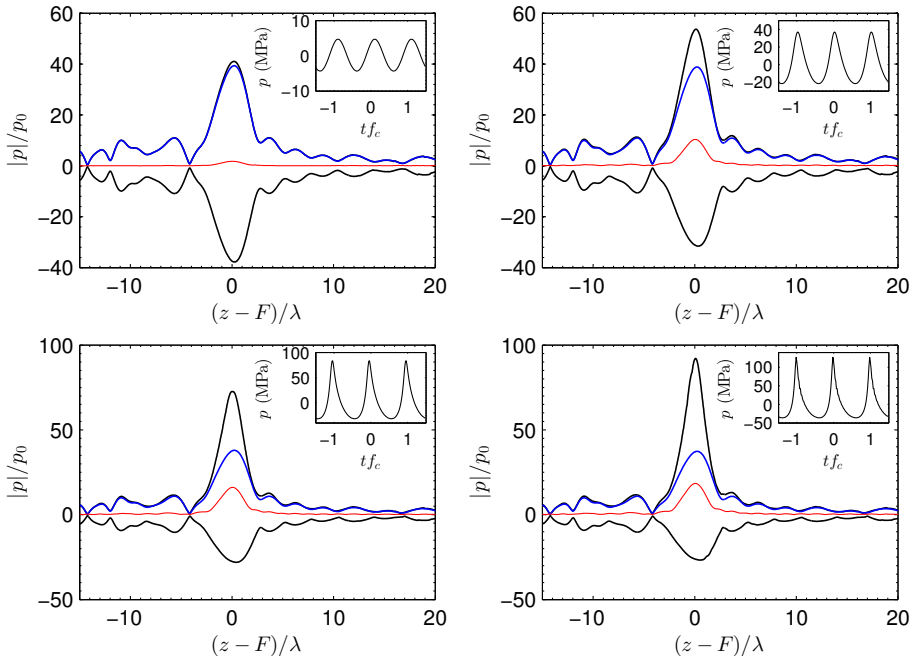


Figure 5.12: Axial field distribution for four increasing amplitudes, being $F/x_s = 0.02, 0.16, 0.260.3$ from low to high amplitude. (Black lines) full envelopes $|p|^+$ and $|p|^-$, (blue) fundamental harmonic component and (red) second harmonic field distribution. The inset shows the corresponding waveforms measured at the focal in physical units.

Finally, from all these the simulation data, the nonlinear dependence of the focusing parameters of the grating is calculated and presented in Fig. 5.13. In first place, the nonlinear gain of the system is shown in Fig. 5.13 (a), where it is plotted the gain for the full peak amplitudes ($|p|^+/p_0$ and $|p|^-/p_0$), and also the corresponding gain for the first, second and third harmonics. It can be seen that the nonlinear effects dramatically increases the peak pressure gain due to the strong asymmetry of the waveforms. In the same way, the gain for the rarefaction pressure decreases with excitation amplitude also due to the asymmetry of the nonlinear distortion at focus (see insets in Fig. 5.12). The gain for the first harmonic is almost constant, around 40 dB, but it slightly reduces for increasing amplitudes as long energy is transferred to higher harmonics. Finally, the gain for second and higher harmonics increases. In the case of second harmonic it varies from 0 to about the half of the linear gain of the system.

There exist also a nonlinear focal shift in the location of the peak pressure, shown in Fig. 5.13 (b). Thus, as the source amplitude is increased the location of the peak pressure is displaced in the axial direction beyond the linear focal position, a self-defocusing effect is observed. On the other hand, for the case of the rarefaction pressure it appears a nonlinear self-focusing effect, i.e. the focal

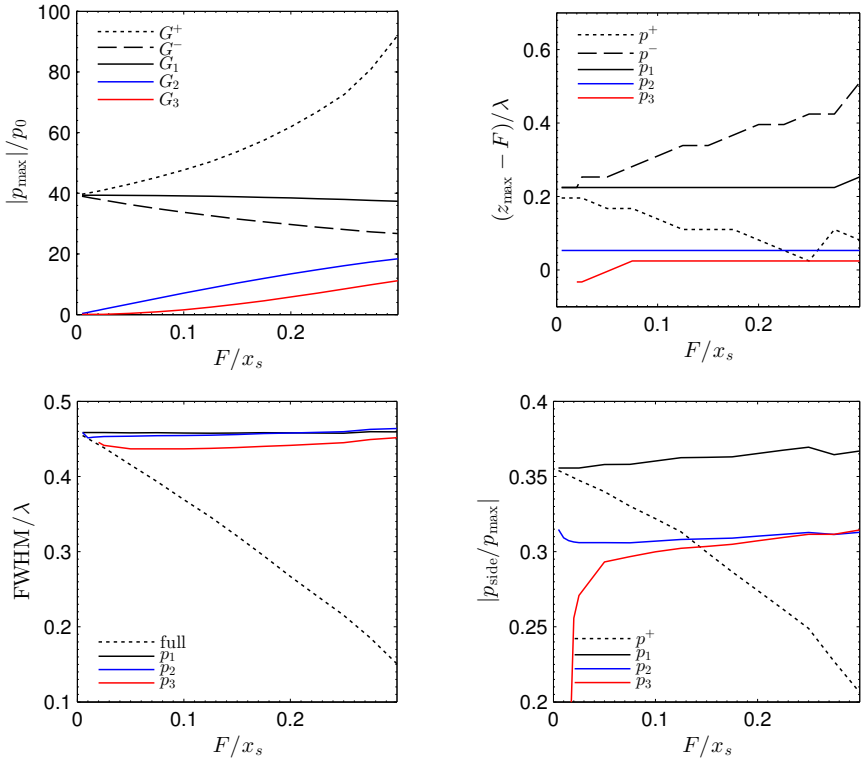


Figure 5.13: Focal characterization in the nonlinear regime. (Up left) Effective gain obtained as $|p_{max}|/p_0$ as a function of the normalized excitation amplitude. (Up right) Location of the peak pressure. (Bottom left) Intensity Full Width at Half Maximum (FWHM), also normalized by the harmonic index. (Bottom right) Side lobe amplitude as a function of the excitation amplitude.

displaces towards the source. Both effects can be related to nonlinear self-refraction of the beam in the focal spot (Camarena et al., 2013a). However, due to the low focal size of this strongly focused device (Camarena et al., 2010) these effects are minor and the total displacements are not longer that $\lambda/4$.

We have analyzed the FWHM of the several harmonics as the amplitude of the incident wave in increased. Figure 5.13 (c) shows the dependence of FWHM on the amplitude of the incident wave, measured again in terms of the shock distance normalized to the focal position in the linear regime, F. FWHM is constant for both the fundamental and the second harmonic focal spots, note here that the second harmonic focal size is effectively half of the size of the fundamental wave, but we show the value normalized to its wavelength. It is worth noting here, that as the nonlinearity of the medium is activated, the focal spot considering all the components, decreases dramatically its FWHM because of the strong asymmetry of the waveforms only at the focal spot.

Finally, we can compare the different transversal profiles and observe the reduction of the side lobes of the second-and-higher harmonic profiles. The numerical results show the highly reduced lobes around the focal spot both in the radial and in the longitudinal directions. This effect is caused by the locally generation of the field only at the focal spot, where in the other hand, the nonlinear (local) harmonic generation at the lateral lobes is reduced due to its low amplitude. It is worth noting here that the reduction does not strongly depends on the excitation amplitude: very weak nonlinear effects are enough to provide second harmonic side-lobe reduction.

5.6 Conclusions

We have presented a characterization of the focusing properties of an axisymmetric grating constructed by toroidal scatters. The design is equivalent to a binary Fresnel lens of infinitesimally thicker slits. We demonstrated experimentally and numerically that the device presents a very narrow focal spot, that is between the sub-diffraction and the sub-wavelength limits. As common from other Fresnel-like lenses and also in Bessel beams, the narrow focal is accompanied by high amplitude side lobes. On the other hand, the confined focal provides strong energy concentration over a small volume. Thus, nonlinear effects can be mainly activated locally at the focal spot, and second harmonic is generated mainly there. In this way, the field of the second harmonic maintain the excellent beam-width of the Fresnel lens, while its side-lobes are strongly reduced. The proposed lens in the weakly nonlinear regime is suitable for second harmonic imaging techniques: the excellent beam spatial resolution of the second harmonic (normalized to the wavelength) is maintained, while the side-lobe amplitude, responsible of signal-to-noise ratio, is reduced.

Another important feature is related to the energy concentration of the system. In the proposed system, an amplification of the incident field up to 30 dB has been observed numerically and experimentally. A parametric study shows that amplification values up to 35 dB can be also obtained if the number of rings, i.e. the aperture, are increased to $M = 50$.

Finally, it is worth noting here that the device is designed for single frequency operation. The chromatic aberration for frequencies around the design frequency is not strong: for a relatively broad bandwidth, around one octave, the main observed effect in simulations and experiments is a focal shift. The focal spot shifts in the axial direction and the displacement can be estimated analytically. For the presented device a focal displacement of about 30 wavelengths has been observed in the frequency range studied. The gain also is modified by the chromatic aberration, but notice that these variations can be compensated by signal processing. In this way, the focal aberration provides a way to actively change the axial location of the sharp focus if the passive device is excited by a frequency modulated signal.

Thus, it can provide a cheap alternative to ultrasound imaging techniques that requires a fast intense moving focal, as in Supersonic Shear Imaging.

References

Averkiou, Michalakis A, David N Roundhill, and JE Powers (1997). "A new imaging technique based on the nonlinear properties of tissues". In: *Ultrasonics Symposium, 1997. Proceedings., 1997 IEEE*. Vol. 2. IEEE, pp. 1561–1566.

Bailey, MR, VA Khokhlova, OA Sapozhnikov, SG Kargl, and LA Crum (2003). "Physical mechanisms of the therapeutic effect of ultrasound (a review)". In: *Acoustical Physics* 49.4, pp. 369–388.

Bercoff, Jérémy, Mickaël Tanter, and Mathias Fink (2004). "Supersonic shear imaging: a new technique for soft tissue elasticity mapping". In: *Ultrasonics, Ferroelectrics, and Frequency Control, IEEE Transactions on* 51.4, pp. 396–409.

Botteldooren, Dick (1995). "Finite-difference time-domain simulation of low-frequency room acoustic problems". In: *The Journal of the Acoustical Society of America* 98.6, pp. 3302–3308.

Camarena, Francisco, Yuri Makov, Víctor Sánchez-Morcillo, Silvia Adrián, and Noé Jiménez (2010). "Nonlinear focal shift in medium Fresnel-number focused acoustic beams". In: *Ultrasonics Symposium (IUS), 2010 IEEE*. IEEE, pp. 1845–1848.

Camarena, Francisco, Silvia Adrian-Martinez, Noe Jimenez, and Victor Sanchez-Morcillo (2013a). "Nonlinear focal shift beyond the geometrical focus in moderately focused acoustic beams". In: *The Journal of the Acoustical Society of America* 134, pp. 1463–1472.

Canney, Michael S, Michael R Bailey, Lawrence A Crum, Vera A Khokhlova, and Oleg A Sapozhnikov (2008). "Acoustic characterization of high intensity focused ultrasound fields: A combined measurement and modeling approach". In: *The Journal of the Acoustical Society of America* 124.4, pp. 2406–2420.

Caupin, Frédéric and Eric Herbert (2006). "Cavitation in water: a review". In: *Comptes Rendus Physique* 7.9, pp. 1000–1017.

Choi, James J, Mathieu Pernot, Scott A Small, and Elisa E Konofagou (2007). "Noninvasive, transcranial and localized opening of the blood-brain barrier using focused ultrasound in mice". In: *Ultrasound in medicine & biology* 33.1, pp. 95–104.

Clement, G., H. Nomura, and T. Kamakura (2015). "Ultrasound field measurement using a binary lens". In: *Ultrasonics, Ferroelectrics, and Frequency Control, IEEE Transactions on* 62.2, pp. 350–359.

Cunningham, Kevin B and Mark F Hamilton (2000b). "Bessel beams of finite amplitude in absorbing fluids". In: *The Journal of the Acoustical Society of America* 108.2, pp. 519–525.

Ding, Desheng and Zuhong Lu (1996). "The second harmonic component in the Bessel beam". In: *Applied physics letters* 68.5, pp. 608–610.

Ding, Desheng and L Jian-yu (2000b). "Higher-order harmonics of limited diffraction Bessel beams". In: *The Journal of the Acoustical Society of America* 107, pp. 1212–1214.

Duck, Francis A (2002). "Nonlinear acoustics in diagnostic ultrasound". In: *Ultrasound in medicine & biology* 28.1, pp. 1–18.

Farnow, SA and BA Auld (1974). "Acoustic Fresnel zone plate transducers". In: *Applied Physics Letters* 25.12, pp. 681–682.

Holm, Sverre and Fabrice Prieur (2010). "Low sidelobe limited diffraction beams in the nonlinear regime". In: *The Journal of the Acoustical Society of America* 128.3, pp. 1015–1020.

Hsu, DK, FJ Margetan, and DO Thompson (1989b). "Bessel beam ultrasonic transducer: Fabrication method and experimental results". In: *Applied physics letters* 55.20, pp. 2066–2068.

Jimenez, Noe, Vicente Romero-García, R Picó, A Cebrecos, Víctor José Sánchez-Morcillo, LM Garcia-Raffi, Juan Vicente Sánchez-Pérez, and K Staliunas (2014). "Acoustic Bessel-like beam formation by an axisymmetric grating". In: *EPL (Europhysics Letters)* 106.2, p. 24005.

Konofagou, Elisa E and Kullervo Hynynen (2003). "Localized harmonic motion imaging: theory, simulations and experiments". In: *Ultrasound in medicine & biology* 29.10, pp. 1405–1413.

Lu, J.-y. and J.F. Greenleaf (1990b). "Ultrasonic nondiffracting transducer for medical imaging". In: *Ultrasonics, Ferroelectrics, and Frequency Control, IEEE Transactions on* 37.5, pp. 438–447.

Molerón, M., A. Leonard, and C. Daraio (2014). "Solitary waves in a chain of repelling magnets". In: *J. Appl. Phys.* 115.18, p. 184901.

Nguyen, Man Minh, Junseob Shin, and Jesse Yen (2014). "Harmonic Imaging with Fresnel Beamforming in the Presence of Phase Aberration". In: *Ultrasound in medicine & biology* 40.10, pp. 2488–2498.

Nightingale, Kathryn, Mary Scott Soo, Roger Nightingale, and Gregg Trahey (2002). "Acoustic radiation force impulse imaging: in vivo demonstration of clinical feasibility". In: *Ultrasound in medicine & biology* 28.2, pp. 227–235.

Sarvazyan, Armen P, Oleg V Rudenko, Scott D Swanson, J Brian Fowlkes, and Stanislav Y Emelianov (1998). "Shear wave elasticity imaging: a new ultrasonic technology of medical diagnostics". In: *Ultrasound in medicine & biology* 24.9, pp. 1419–1435.

Schindel, DW, AG Bashford, and DA Hutchins (1997). "Focussing of ultrasonic waves in air using a micromachined Fresnel zone-plate". In: *Ultrasonics* 35.4, pp. 275–285.

Sleva, Michael Z, William D Hunt, and Ronald D Briggs (1994). "Focusing performance of epoxy- and air-backed polyvinylidene fluoride Fresnel zone plates". In: *The Journal of the Acoustical Society of America* 96.3, pp. 1627–1633.

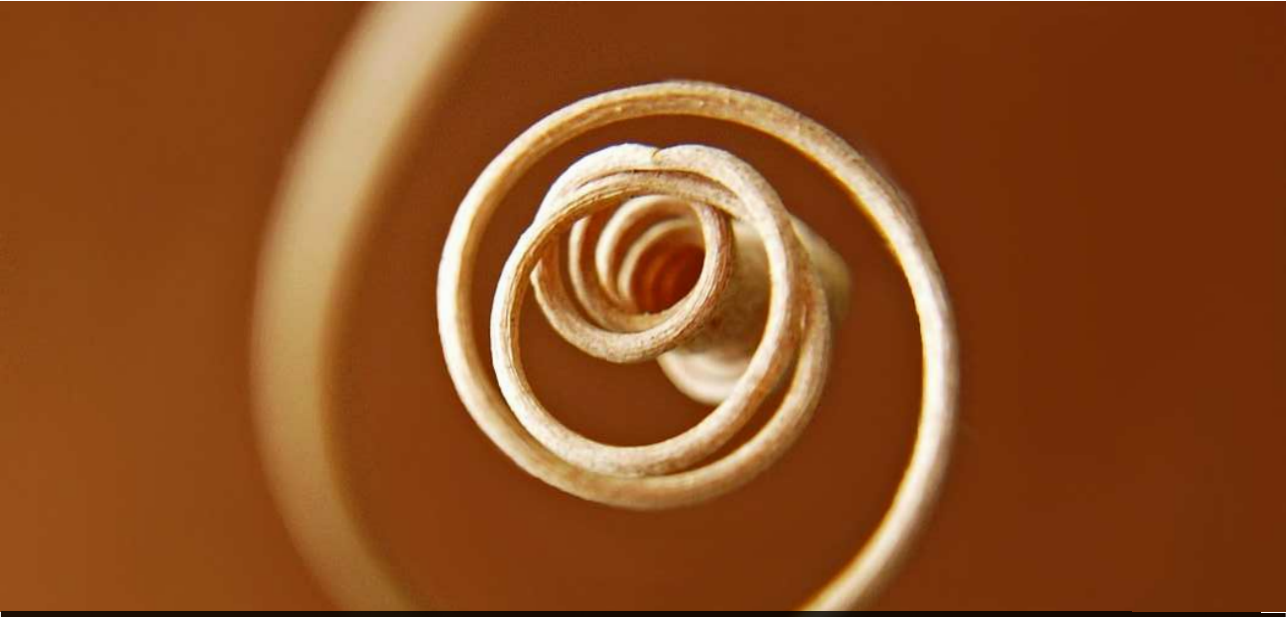
Wang, Hui, Da Xing, and Liangzhong Xiang (2008). "Photoacoustic imaging using an ultrasonic Fresnel zone plate transducer". In: *Journal of Physics D: Applied Physics* 41.9, p. 095111.

Publications

The contents of this Chapter have been presented in the following publications:

Journal papers

- **Jiménez, N.**; Romero-García, V.; Picó, R.; Cebrecos, A.; Sánchez-Morcillo, V.; García-Raffi, L.; and Staliunas, K. "Transition from linear- to nonlinear-focusing regime of ultrasonic waves produced by an axisymmetric diffraction grating" *In preparation* (2015)



Chapter 6

Chiral Beams generated by Spiral Gratings

Abstract

Previously, zeroth order Bessel-like beams have been generated by axisymmetric diffraction gratings. Here, we report the generation of high order Bessel beams by the diffraction of plane waves over spiral shaped scatters. The acoustical beam vortex structure is analyzed and a method for generate arbitrary order Bessel beams based in multiple arms spirals is presented. A passive device is experimentally tested in the ultrasound regime and a first order Bessel vortex beam is observed. Simulations in the weak nonlinear regime are also included where the conservation law for the ratio between the topological charge of the beam and the generated harmonic order is proved. This novel technique can be used to generate cheap lenses for acoustic particle manipulation and acoustic radiation force applications.

6.1 Introduction

In the previous Chapters (4, 5) the diffraction generated by axisymmetric structures is analyzed for generate Bessel beams and strongly focused beams. Many of these axisymmetric structures, matching its symmetry with the usual sources, have been proposed for the control of the acoustic field. thus, zeroth-order Bessel-like beams can be generated by these structures in Bragg regime (Jimenez et al., 2014). In the long-wavelength limit, GRaded INdex (GRIN) lenses amplify the field in the axis (Romero-García et al., 2013; Molerón et al., 2014). In all of these configurations the scattered field maintain the axisymmetry of the lenses.

Zeroth-order Bessel beams, as those reported in Chapter 4, present a maximum of the field trough the axis. On the other hand, higher-order Bessel beams exhibit a minimum of the field at the axis. Both, zeroth and higher Bessel beams propagates in free space without any diffraction spreading, as long they are propagation-invariant solutions of the Helmholtz equation (Durnin et al., 1987). Both types of beams are characterized by the appearance of high amplitude concentric rings surrounding the axis that its transverse profile follows a lth-order Bessel function. Is important to note also that the magnitude of the spatial spectrum of these beams does not depends of the order of the beam, i.e. in the far field all Bessel beam is characterized by a annular radiation. In other words, all Bessel beams can be generated by a conical wavefront of infinite extension. The difference between zeroth and higher order Bessel beams is that for higher order Bessel beams the azimuthal phase shows a linear variation across its annular spectrum. Thus, the central zero in the axis of the higher-order Bessel beams that appears in the near field is caused due to the phase singularity of charge l associated with the azimuthal phase variations.

In this way, high order Bessel beams generates acoustical vortices with a spatial phase dependence that cannot be generated by axisymmetric radiating sources. In optics, different solutions have been proposed to break the axial symmetry in an appropriate way to generate vortices. These methods include direct Gaussian beam illumination by use of axicon-type computer generated holograms (Vasara et al., 1989; Heckenberg et al., 1992) or illuminating an axicon with a Laguerre–Gaussian mode (Arlt et al., 2000). Another solution is to impose an azimuth-dependent retardation on the optical field with Spiral Phase Plates (SPP) (Oemrawsingh et al., 2004). A diffraction grating with groove bifurcation (called "fork") is also able to generate a vortex from an optical beam falling onto the grating center with an arbitrary topological charge (Bekshaev et al., 2008).

Although phase dislocations were first studied in acoustics (Nye et al., 1974), the related experimental works have been developed lately. The acoustic analog of optical Spiral Phase Plates was proposed by Hefner et al. (1999). Here, the transducer surface is physically offset by twisting like the coil of a spring. This design has an important limitation: the transducer has a unique operating frequency of

interest. Other approaches include the use of photoacoustic effeect to generate the Helical beam (Gspan et al., 2004). A common approach to overcome this problem is by using electronic means: an appropriate phase profile for an array of transducers generates the helical beam. Thus, signals emitted by each transducer of the array are delayed in order to control the angular phase shift. The interaction of high order Bessel beams with particles have been widely studied in the exhaustive collection of works of F. G. Mitri and G. T. Silva among others. Two main remarkable effects have been reported: (1) the transference of orbital momentum from the acoustical vortex to the particle (Mitri et al., 2012), and on the other hand, the appearance of negative axial acoustic radiation forces (Marston, 2006; Marston, 2007a; Mitri, 2008; Mitri, 2009). Thus, practical applications of vortex acoustic beams are multiple: particle manipulation (Demore et al., 2011) and acoustical tweezers (Wu, 1991), an acoustic spanner (Skeldon et al., 2008), rotation of fibers (Schwarz, 2013) or multiple-particle trapping (Yoon et al., 2014). However, although the array provides active steering and control of the vortex beam, in these active methods the discretization of the source is restricted by the number of transducers in the array. On the other hand, the screw dislocations generated by finite amplitude acoustical vortex has been also studied. In the case of weak nonlinear regime, it has been proved the conservation law for the ratio between the topological charge of the beam and the generated harmonic order (Thomas et al., 2003; Marchiano et al., 2008). ON the other hand, for intense acoustic beams, azimuthal shock wave have been reported numerically and experimentally (Marchiano et al., 2008; Brunet et al., 2009; Brunet et al., 2010).

In this Chapter we propose a passive system for the formation of acoustic vortex. The design consist of an Archimedes' spiral grating. An experimental setup is proposed in the ultrasound regime, where the results show that the diffracted field around the axis generates a first order Bessel beam with its characteristic screw dislocation. A method for synthesize high order Bessel beams is also provided and tested numerically, where it was proven that a n-arm spiral generates a nth-order Bessel beam. Furthermore, weakly nonlinear propagation is considered, where the conservation law for the ratio between the topological charge of the beam and the generated harmonic order is also observed.

6.2 From axisymmetric to chiral beams

Let us start considering a pair of uniform axisymmetric gratings, A and B, as those studied before in Chapter 4. Let the grating A only differ in one aspect from the grating B: a shift in the radial position of the toroidal rings. Figure 6.1 shows a scheme of the situation. Therefore, the first structure presents a radial distribution for the M toroidal rings as $r_m = ma$, where a is the separation distance between rings and $m = (1, 2, ..., M)$ is the ring index. On the other hand, the second structure is designed as $r_m = ma + a/2$. The incident plane wave is scattered by

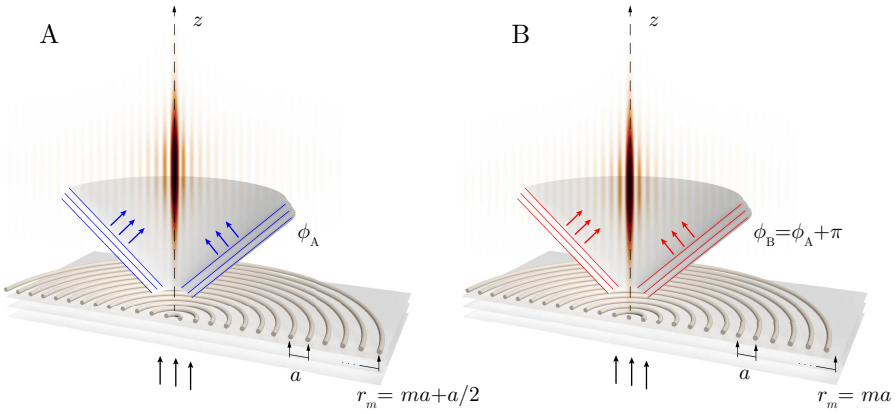


Figure 6.1: Scheme of the axisymmetric diffraction grating. The structure A differs from B by a shift of $\Delta r = a/2$ in the radial distribution of the rings. The incident plane wave is scattered by the structures in a converging conical wavefront. When it converges to the axis a Bessel beam is formed. The beams generated have equal magnitude but are shifted $\Delta\phi = 2\pi\Delta r/a$, that in this example, for $\Delta r = a/2$ leads to a phase difference of $\Delta\phi = pi$.

the structure creating a conical wavefront that converges to the axis of symmetry creating a limited-aperture Bessel beam. Same situation is also produced in the configuration B, with the only main difference of the scattered field is phase shifted.

Numerical solutions for the scattering of the two structures are shown in Fig. 6.2. It is clearly visible how the magnitude of the field remains basically the same, where the transversal field is described by a Bessel function of zeroth order, namely J_0. In the other hand, the phase difference between the structure

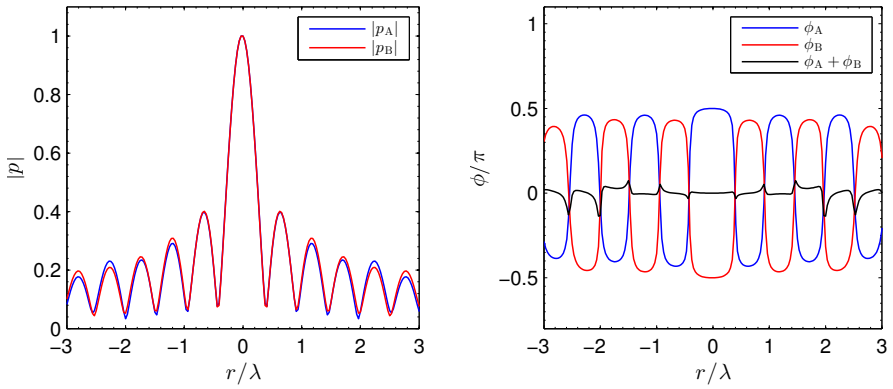


Figure 6.2: Radial distribution of the field generated by the axisymmetric structures A and B. (left) Magnitude, (right) phase. Note if the $\phi_A + \phi_B = 0$, then $\Delta\phi = \pi$.

A and the shifted grating B is π radians. The field remains in anti-phase not only at the center, but over all the the lateral lobes of the Bessel function. Only at the zeros of the Bessel function there exist in the simulations some not perfect anti-phase field distribution. In this example, the structure A is shifted in the radial coordinate by half of the radial period, this spatial shift between both structures is $\Delta r = a/2$. In a more general case, the phase difference can be related to the radial shift simply by

$$\Delta\phi = 2\pi\Delta r/a \tag{6.1}$$

where $\Delta\phi = \phi_{\mathrm{A}} - \phi_{\mathrm{B}}$ is the phase difference between fields generated by a gratings shifted a distance Δr.

Thus, we propose a structure composed of curved tubular scatters, but not necessary of toroidal shape, that mixes the properties of the gratings A and B in order to have a destructive interference in the axis. First, is obvious that this structure is no longer axisymmetric, as long the scatters at azimuth angle $\theta = 0$ must be shifted radially by $\Delta r = na/2$ respect to the plane $\theta = \pi$, being n an integer. On the other hand, the tubular scatters must be continuous in azimuth, and the following design condition

$$\phi(\theta) = \phi(\theta + \pi) \pm \pi \tag{6.2}$$

must hold for any θ. This condition is necessary in order to achieve a minimum at the axis. It essentially states that there exist a scattered field at some θ that have inverted phase respect to the scattered field at opposite azimuth $\theta + \pi$.

Let us here assume that the phase of the field changes linearly with the azimuth angle as $\phi = \alpha\theta$. Substituting this equation in Eq. (6.2) we get that, in order to fulfill the design conditions, that the rate of change of phase respect to the azimuth angle must be $\alpha = \pm 1$, leading to the simple relation $\phi = \pm\theta$.

Then, we can write Eq. (6.1) as

$$\frac{\Delta r}{\Delta\phi} = \frac{a}{2\pi}. \tag{6.3}$$

This relation states that the rate of change in the radial position of the tubes respect to the changes produced in the phase of the field is constant. Thus, using $\Delta\phi = \pm\Delta\theta$, we can relate the change of the radial position of the tubes respect to the azimuth coordinate as

$$\frac{\Delta r}{\Delta\theta} = \pm\frac{a}{2\pi}. \tag{6.4}$$

In the continuous limit, $\frac{\Delta r}{\Delta\theta} \to \frac{\partial r}{\partial\theta}$ and therefore Eq. (6.4) can be expressed as the parametric curve

$$r = \pm b\theta \tag{6.5}$$

with $b = a/2\pi$. Thus, if the tubular scatterers are bend following this parametric curve, the scattering of the structure in the axis must be zero. This expression is the Archimedes' spiral, a particular case of the general class of Archimedean spirals that can be described by

$$r = \pm b\theta^{1/\gamma}. \tag{6.6}$$

Here, the parameter γ controls how fast the spiral is wrapped. For $\gamma = 1$, we get the normal Archimedes' spiral, with uniform separation between turns, for $\gamma > 1$ the spiral radius grows with each turn, while for $\gamma < 1$ the separation distance between turns becomes thigh. Special cases of this family are the lituus ($\gamma = -2$), the hyperbolic spiral ($\gamma = -1$) or the Fermat's spiral ($\gamma = 2$).

6.3 Chiral beams generated by spiral gratings

In the previous section we have found that the spirals gratings are good candidates to provide chiral beams. These spirals have the propriety of having uniform separation between turns as $r(\theta + 2\pi) = r(\theta) + a$. This uniformly spaced grating, as occurs in the previously studied Bessel beams, diffracts plane waves in a converging conical wavefront[1]. In analogy to the well-known diffraction grating, the angle β defined by the conical wavefront is

$$\sin\beta = N\lambda/a, \tag{6.7}$$

where λ is the wavelength and N is the diffraction order. A scheme of this situation is shown in Fig. 6.3. It is well known that a converging conical wavefront generates a Bessel beam. The field of an ideal Bessel beam can be expressed for the velocity potential[2], ψ, as

$$\psi\left(r, \theta, z\right) = \psi_0 J_n\left(k_r r\right) \exp\left(i k_z z \pm i n\theta\right), \tag{6.8}$$

where J_n is the nth-order Bessel function ψ_0 is the amplitude, and k_z and k_r are axial and transverse components of the wavevector $k = \sqrt{k_z^2 + k_r^2}$. It is important the relation of this quantities to the cone angle of the Bessel beam

$$\cos\beta = k_z/k \ , \ \sin\beta = k_r/k. \tag{6.9}$$

[1]Note that the field is also scattered in a diverging cone with angle $\pi/2 - \beta$, but this waves does not contributes to the field distribution near the axis in free propagation. If the structure is embedded inside a tube, this field can be reflected by the boundaries and it will converge to the axis creating another Bessel beam.

[2]the velocity potential can be related to the acoustic pressure as $p = i\omega\rho_0\psi$ and to particle velocity as $\mathbf{v} = \nabla\psi$

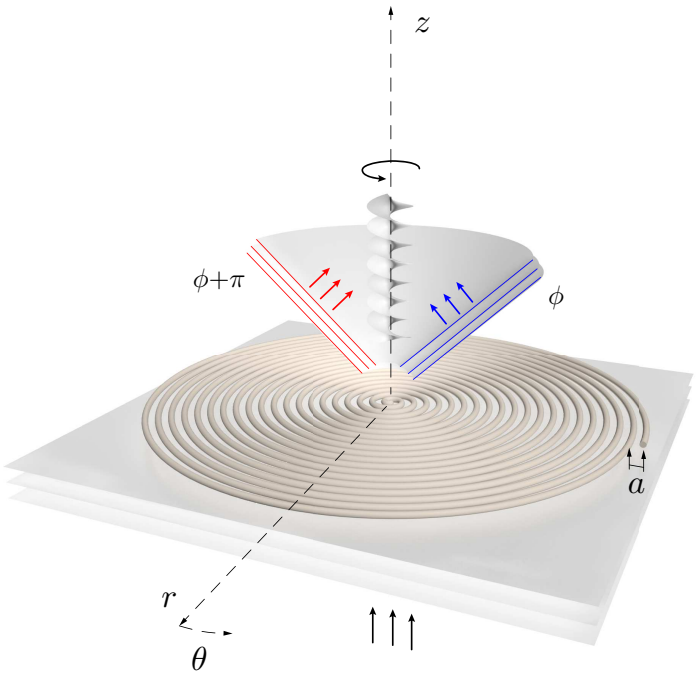


Figure 6.3: Scheme of the Archimedes' spiral scattering process. The incident plane wave is scattered into a converging conical wavefront which its phase changes linearly in azimuthal angle θ. The field can be described as a first order Bessel beam, where in the axis a corkscrew dislocation is produced, leading to an acoustic vortex and a node at $r = 0$.

Note the trivial solution for $\beta = 0$, where the Bessel beam reduces to a plane wave traveling in the z direction. Therefor, thee cone angle β of the Bessel beam depends on the separation of scatters. Thus, combining Eq. (6.7) and (6.9) we get the relations

$$k_z = \frac{2\pi N}{a \tan \beta} \ , \ k_r = \frac{2\pi N}{a}. \tag{6.10}$$

This relations allow us to obtain the Bessel beam field, Eq. (6.8) in terms of the grating parameters as

$$\psi\left(r, \theta, z\right) = \psi_0 J_n \left(\frac{2\pi N}{a} r\right) \exp\left(i \frac{2\pi N}{a \tan \beta} z \pm in\theta\right). \tag{6.11}$$

This idealized field is valid for a grating of infinite aperture. In the case of a real

structure with finite aperture, the Bessel beam is bounded in the axial direction. Is common to refer to this limitation as limited diffraction Bessel beams. Therefore, if the grating have a total aperture of $R = Ma$, where M is the number of turns of the spiral, from simple trigonometrical considerations the cone angle will cover a region of the axis from $z = 0$ to $z = F$, being

$$F = \frac{R}{\tan\beta} = \frac{Ma^2}{N\lambda}\sqrt{1 - \left(\frac{N\lambda}{a}\right)^2} \tag{6.12}$$

the maximum distance at which the Bessel beam is formed, showing the limit of the validity of the nondiffractive propagation.

Let us consider the radiation converging from each ring at angle β, in order to find the locus of the points around the axis where exact constructive interference is produced. The spiral grating is not axisymmetric, but chiral, that is, it is distinguishable from its mirror image and it cannot be superposed onto it. Thus, the radiation converging from each ring do not converge along the symmetry axis. Figure 6.4 shows a scheme, where if we suppose the grating diffracts the wave at angle β, and following simple trigonometry considerations the coordinates of the focal points can be obtained in function of the spiral geometry. Thus, for the axial component of the focal can be expressed as

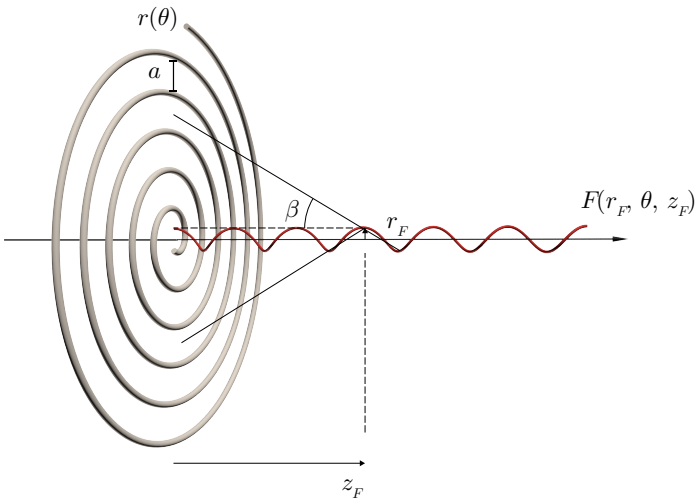


Figure 6.4: Scheme of the geometry of the spiral. Due to the scattering of the spiral at angle β, the locus of points in which perfect constructive interference is produced around the axis is an helix.

$$z_F(r,\theta) = \frac{r(\theta) + \frac{a}{4}}{\sin\beta}\sqrt{1-\sin^2\beta}. \tag{6.13}$$

Then, using the cone angle definition and the spiral curve $r(\theta)$ we get

$$z_F(\theta) = \left(\frac{\theta}{2\pi} + \frac{1}{4}\right)\frac{a^2}{N\lambda}\sqrt{1-\left(\frac{N\lambda}{a}\right)^2}. \tag{6.14}$$

On the other hand, this interference is not produced at the axis, but shifted a constant radial distance. From the geometry, see Fig 6.4, we can see that the radial component of the focal is

$$r_F = a/4. \tag{6.15}$$

Equations (6.14-6.15) composes the curve $F(r_F, \theta, z_F)$, that is a liner helix of constant radius. Thus, in addition the beam generation, the scattering located in the points of the spiral achieves perfect constructive interference over the helix curve that rotates around the axis. Moreover, the distance between turn of this helix can be calculated as $z_F(\theta + 2\pi) - z_F(\theta) = \lambda\cos\beta/N$. Thus, for small diffraction angles, the focal rotates in z with a period of the order of the wavelength, when for shorter Bessel cone is generated, the distance between rotation in the helix stretches[3].

6.3.1 First order Bessel beams

Let us now analyze the Archimedes' spiral with $\gamma = 1$ and $b = a/2\pi$. With this parameters the ideal Bessel beam can be expressed as

$$\psi(r,\theta,z) = \psi_0 J_n\left(\frac{N}{b}r\right)\exp\left(i\frac{N}{b\tan\beta}z \pm in\theta\right). \tag{6.16}$$

In the other hand, we model the scattering of the grating by two methods. First, if the scatters are thing compared to the wavelength, we can assume the scattering of each fragment of the spiral can be modeled by a point source. This modeling is also valid in the opposite limit, where the scatterers are thick enough to provide narrow aperture between them. In this situation the structure forms a grating. From Babinet's principle considerations, both situations can be equivalent. Therefore, we calculate the Rayleigh-Sommerfeld diffraction integral along the path of the spiral, $r = b\theta$, as

$$p(x,y,z) = \frac{-i\omega\rho_0 v_0}{2\pi}\int_r \frac{\exp(ik|\mathbf{r}|)}{|\mathbf{r}|}dr \tag{6.17}$$

[3]In the limit $\beta \to 0$, where the helix period is the wavelength, the divergent and convergent conical wavefront sums again into a plane wave. Thus, the helicity disappears due to the topological charge of two chiral waves is inverted.

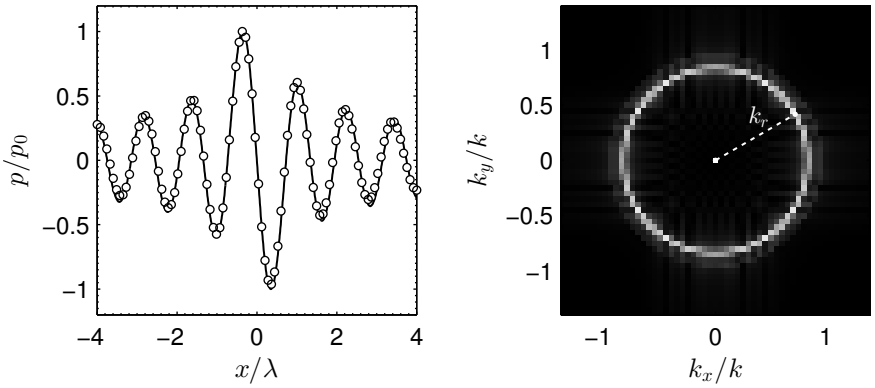


Figure 6.5: (Left) Transversal cut of beam field obtained by (continuous line) the analytic expression for ideal Bessel beam Eq. (6.16) and (circles) obtained by numerical evaluation of the Rayleigh-Sommerfeld diffraction integral Eq. (6.17) for a finite structure. (Right) Far-field of the spiral scattering showing the typical ring of the Bessel beam.

where $|\mathbf{r}|$ is the distance between each point in the path, $r = b\theta$, and the observation point (x, y, z).

Second, we also approximate the diffraction with full-wave numerical integration of the acoustic wave equations. This approach provides an accurate estimation of the diffraction in situations where the wavelength is of the order of the scatter size, but due to the problem is 3D, the full cartesian domain is integrated and is computationally intensive. In order to reduce the grid refinement requirements, we use the k-space method for solving the 3D computational problem. This method will be necessary also for the last section where we include the nonlinear propagation effects.

Figure 6.5 shows an example of first order Bessel-like beam generated by an uniform spiral with parameters $\beta = 56.4^{\text{o}}$, $a/\lambda = 1.2$ and aperture $R = 60\lambda$. We can see that the analytic expression for ideal Bessel beam Eq. (6.16) agrees with the solution obtained by the numerical evaluation of the Rayleigh-Sommerfeld diffraction integral Eq. (6.17) for this finite structure. On the right subplot, it can be appreciated how the typical ring of the Bessel beam appears in the far-field. This result shows that a conical wavefront is being generated by the structure, and it can be seen that the transversal wavenumber agrees with the estimated by the spiral parameters in Eq. (6.10), marked as a dotted line as k_r in the figure. Therefore, we prove the field generated by the spiral structure is a first order Bessel-like beam.

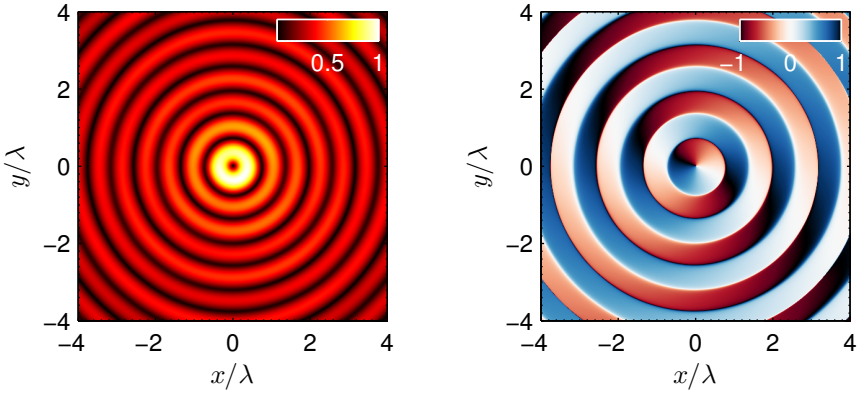


Figure 6.6: Transversal distribution of the field obtained by numerical evaluation of the Rayleigh-Sommerfeld diffraction integral. (Left) Magnitude, (right) phase. Colorbars in normalized units (p/p_0 and ϕ/π).

Radial distribution: vortex

One of the main features of the high order Bessel beams (HOBBs) is that all over the axis the field is zero, in contrast with the zeroth-order Bessel beam where a maximum appears in the symmetry axis. In the high order Bessel beams this zero is generated by destructive interference of a phase-rotating conical wavefront. Therefore, as a necessary condition, a vortex is generated around the axis. Figure 6.6 shows the transversal distribution of the field of a spiral at $F/2$. It can be observed the node at the center in the magnitude, as long the high amplitude lateral lobes characteristic of the HOBBs.

On the right subplot, it can be appreciated that a vortex is generated. The number of complete phase shifts per turn is one, the vortex presents a topological charge of 1. The nodes of the field connects 2 areas with opposite phase, while at the central minimum a screw-cork like dislocation is produced in the field. The ringed areas of the phase distribution corresponding to odd lateral lobes are phase inverted respect than the even ones, but all have the same rotation direction.

Axial distribution

Although the field distribution in the sagittal plane correctly corresponds to a truncated Bessel beam, there exist some features that must be underlined. Figure 6.7 shows the field in the ($x = 0$) plane of two first order Bessel beams. In the top subplot the spiral parameters are $a/\lambda = 1.85$, that leads to a cone angle of $\beta = 32.7^{\text{o}}$ and a beam extension distance of $F = 115\lambda$. As can be seen in the figure, the generated beam agrees with the analytical parameters. However, the farther part of the beam that is close to F presents more amplitude compared to

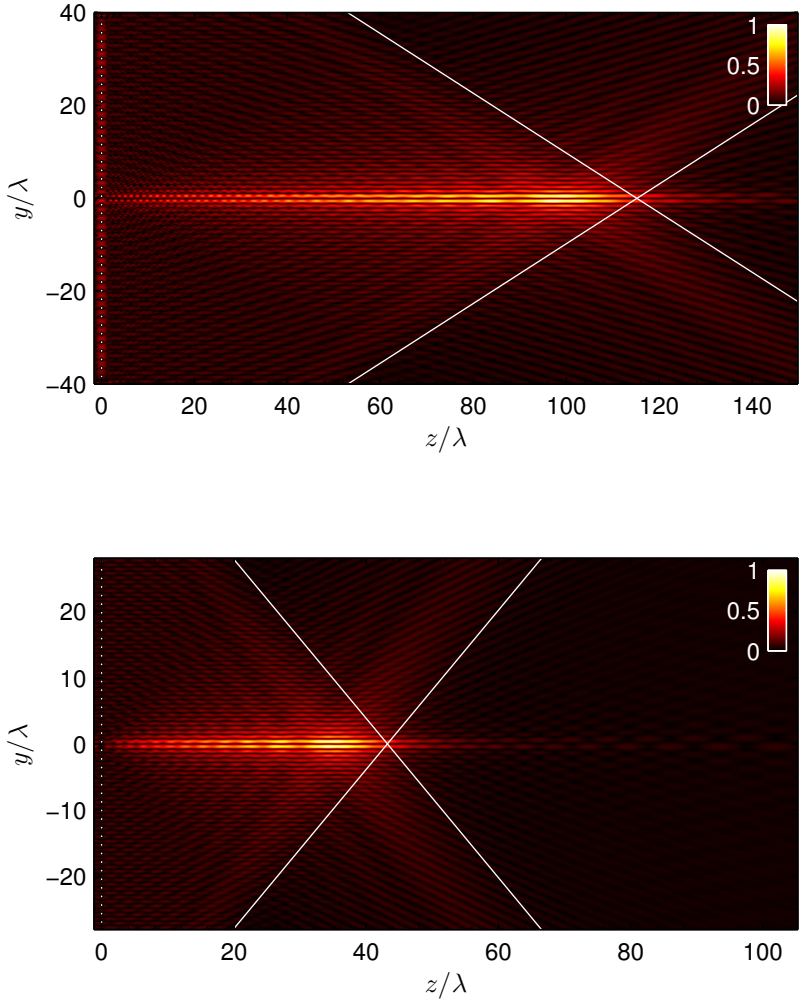


Figure 6.7: (Top) Distribution of the field for a spiral of $a/\lambda = 1.85$ that leads to a (white line) cone angle of $\beta = 32.7^{o}$ and beam extension distance of $F = 115\lambda$ (white line at $y = 0$). (Bottom) Distribution of the field for a spiral of $a/\lambda = 1.3$ that leads to a (white line) cone angle of $\beta = 50^{o}$ and beam extension distance of $F = 43.2\lambda$ (white line at $y = 0$). Colorbars in normalized units ($p/p_{\max}$).

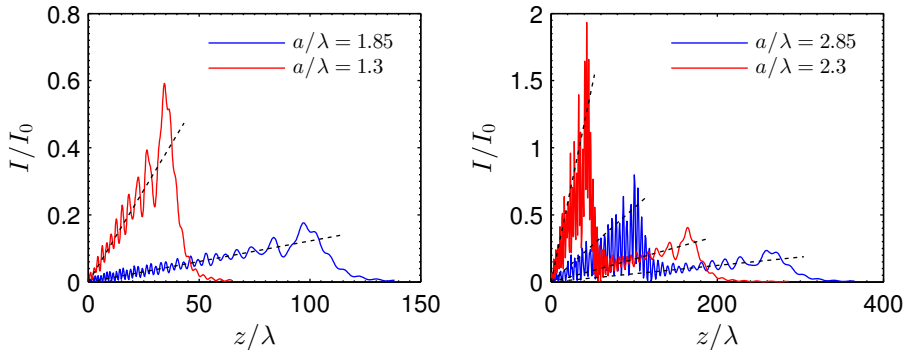


Figure 6.8: (Left) Axial Intensity distribution for a spiral of (blue) $a/\lambda = 1.85$ and (red) $a/\lambda = 1.3$. Black dashed lines shows the analytical extension of the truncated beam with a linear intensity profile. (Right) Axial Intensity distribution including higher diffraction orders for a spiral of (blue) $a/\lambda = 2.85$ and (red) $a/\lambda = 2.3$.

the part of the beam that is close to the grating. On the other hand, the field also present some oscillations in the z direction.

Figure 6.7 (bottom) shows other example at lower frequency. Here, the spiral parameters are $a/\lambda = 1.3$, that leads to a sharper cone angle of $\beta = 50^{\text{o}}$ and a closest extension distance of $F = 43.2$. Same properties can be observed in this situation.

In order to analyze the field amplitude, a axial cut is represented in Fig. 6.8. As long the field is zero in the axis, the intensity distribution shown in Fig. 6.8 is evaluated trough the maximum of the first lateral lobe. It can be clearly seen that the intensity increases linearly with the axial distance. This effect, is analogous to the studied in Sec. 4.2. As long the outermost rings scatters more energy, the external portions of the conical wavefront present more intensity. This energy converges to axial points around F, creating the same Bessel beam but with linearly increasing intensity.

Same effects are observed for the higher diffraction orders. As can be seen in Fig. 6.8 (right), when $a/\lambda > 2$ the higher diffraction orders generates a secondary beam. Its corresponding parameters correctly follows the analytical estimations, as can be seen comparing the beam distribution to the dashed black lines. Due tho the appearance of this secondary beam, the amplitude of the fundamental diffraction order is reduced.

A parametric study of the longitudinal field is presented in Fig. 6.9 (left). It is analogous to the Fig. 4.2 for the zeroth-order Bessel beams. The field distribution extends with frequency following the analytical estimations (white lines), and for $a/\lambda > 2$ higher diffraction orders appears forming secondary Beams close to the grating. On the other hand, similar study can be addressed for the transversal

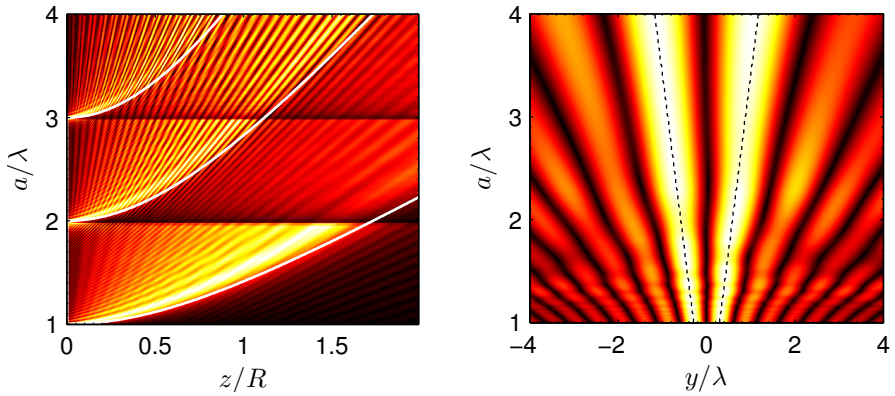


Figure 6.9: (Left) Axial distribution of the field in function of the quantity a/λ obtained by numerical evaluation of the Rayleigh-Sommerfeld diffraction integral. White lines indicates the estimation of the focal by Eq. (6.12). (Right) Transversal distribution of the field in function of the quantity a/λ. Black dotted lines indicates the lateral location of the lobes estimated by Eq. (6.16). Colorbars in normalized units (p/p_0 and ϕ/π).

distribution. Figure 6.9 (right) shows the lateral distribution normalized to the wavelength in both axes. The separation distance is varied. As long the lateral distribution of the HOBBs depends on the transversal component of the wavevector, $k_r = 2\pi N/a$, there exist a lateral dependence of the lateral beam-width respect to spiral parameters. It essentially states that extending the Bessel beam at longer distances by spacing the spiral also spreads the beam-width. The numerical integration agrees with the analytical estimations (dashed black lines).

6.3.2 Experimental validation

An experimental test was realized in order to validate model results. A spiral grating was fabricated by laser cutting over a stainless steel plate of 0.8 mm thickness. Fig. 6.10 (a) shows a scheme of the grating designed. The grating aperture was $a = 1$ mm. The thickness of the scatters was 0.75 mm (solid parts), leading to a grating aperture of 0.25 mm (open parts)[4]. The number of turns was $M = 20$ and the grating radius was $R = 25$ mm. The circular spiral plate was placed in front of a ultrasound plane transducer. This source was formed by a plane single element piezoceramic crystal (PZ 26, Ferroperm Piezoceramics, Denmark) mounted in a custom designed steel housing with aperture $R = 25$ mm, matching the area of the spiral grating. The separation distance between the grating and the source plane was adjusted to 0.5 mm.

[4]As pointed before, following Babinet's principle considerations, the scattered field by an structure of thin scatters or thin slits, in terms of the generated beam profile over the axis, is equivalent.

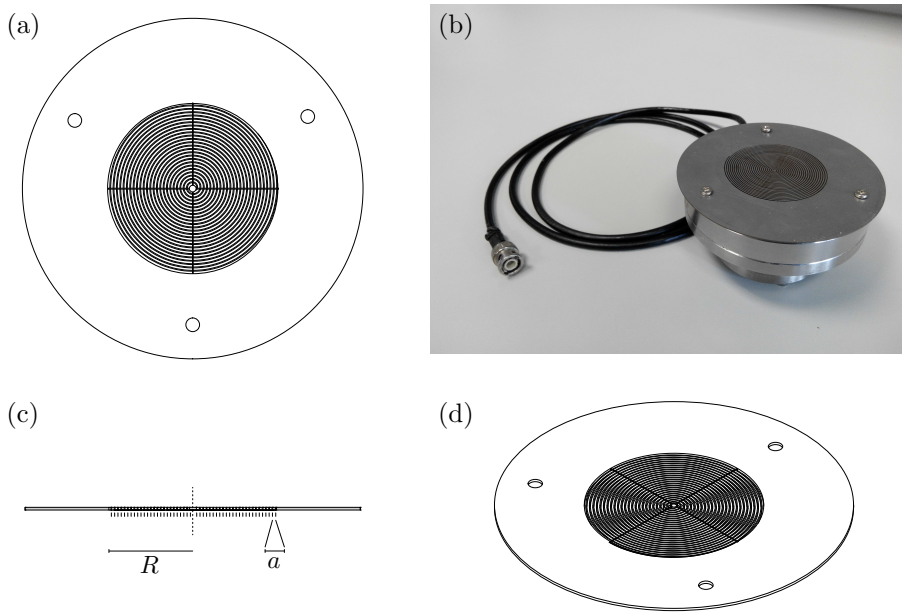


Figure 6.10: (a, c, d) Scheme of the grating used in the experiment. (b) The spiral grating mounted in front of a plane ultrasound transducer.

The transducer was immersed in a degassed and distilled water tank of ($350 \times 350 \times 350$ mm) were during the measurements the temperature was constant at 26° C. Therefore, the theoretical beam extension distance of the proposed grating lens at the operating frequency was $F = 27$ mm and only one diffraction order appear.

The source was driven with a sinusoidal pulse burst of frequency $f_0 = 2.226$ MHz and 50 cycles using a function generator (14 bits, 100 MS/s, model PXI5412, National Instruments) and a linear RF amplifier (ENI 1040L, 400W, 55dB, ENI, Rochester, NY). The pressure waveforms were acquired with a HNR 500 μm needle PVDF hydrophone (Onda Corp, CA), and a digitizer (64 MS/s, model PXI5620, National Instruments) were used. A three-axis micropositioning system (OWIS GmbH, Germany) was used to move the hydrophone in three orthogonal directions with an accuracy of 10 μm and a National Instruments PXI-Technology controller NI8176 was used to control all the devices. The amplitude frequency response of the hydrophone was compensated in post-processing.

Figure 6.11 summarizes the experimental and numerical results, and the Rayleigh-Sommerfeld integration. It can be observed in Fig. 6.11 (a) that the steel grating conform a beam with a zero in its axis, and with a ring shaped maximum surrounding this zero. The experimental beam agrees the analytical Bessel beam presented in Fig. 6.11 (c). On the left column, the phase is shown and, again,

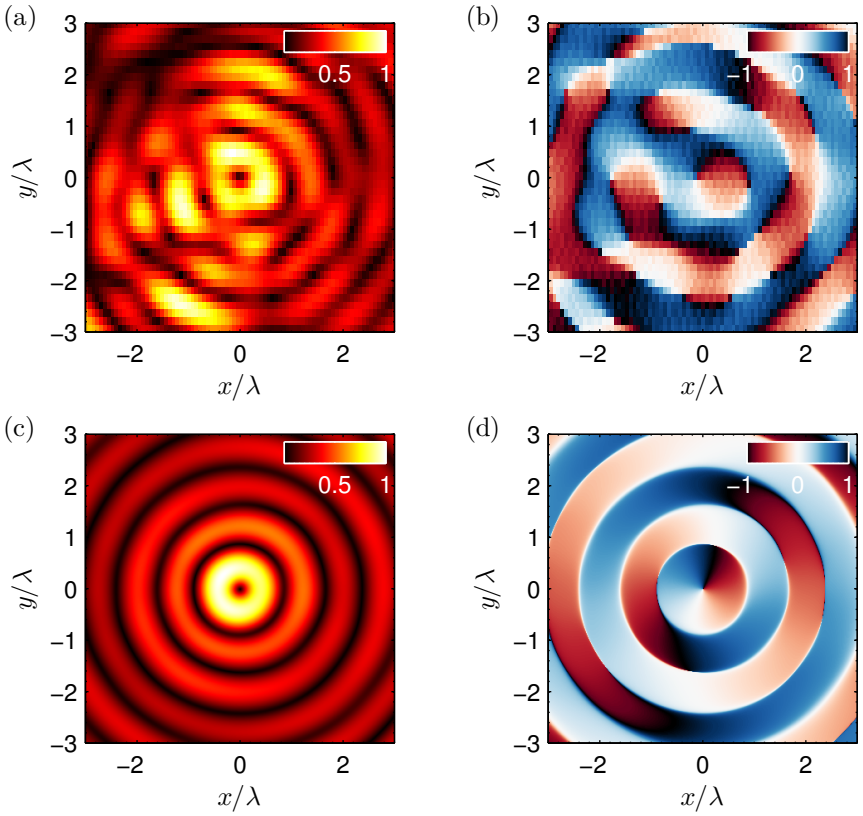


Figure 6.11: (a) Normalized field magnitude and (b) phase observed in the experiment and (c, d) its corresponding analytical estimation using Rayleigh-Sommerfeld integration. Colorbars in $p/p_{\max}$ units for the magnitude and ϕ/π units for the phase.

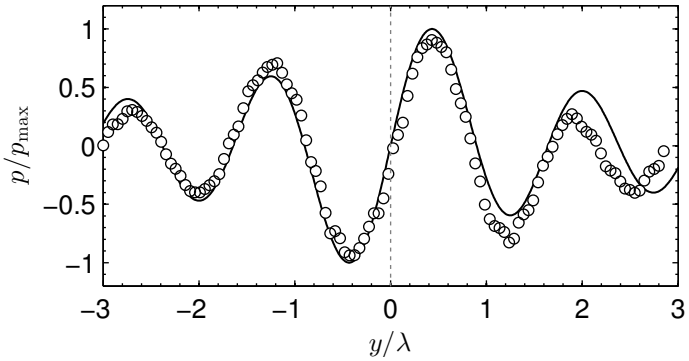


Figure 6.12: Transversal cut of the field observed by (circles) grating experiment and (line) predicted by the HOBB. Vertical line marks the axis were the zero field is expected.

the generated beam in the experiment shows the correct topological charge of the analytic solution plotted in Fig. 6.11 (d). The characteristic screw-cork dislocation of the field at the center is also observed. Moreover, the phase distribution all over the secondary lateral lobes of the beam also shows, in some degree, the correct phase distribution of the HOBB.

However, some discrepancies can be observed in the experimental measurements. These aberrations are minor and can be produced by the misalignment between the grating and the transducer plane. A detailed transversal field profile is presented in Fig. 6.12. The transversal cut (markers) was selected for an azimuthal angle in the (y, x) plane at -3 degrees, in order to present a good fit with the analytical solution (black line). The traversal profile correctly agrees its corresponding $J_1(k_r r)$ first order Bessel function. Minor aberration slightly modifies the lateral lobe amplitude, but the main features of the high order Bessel beam, i.e. its central zero and rotational vortex, are correctly observed by the proposed (and simple) experimental setup.

6.4 High order Bessel beams generated by n-arm spirals

In the preceding section a synthesis of first order Bessel beams is proposed. The basic principle of formation is the destructive interference trough the axis of a rotating-phase conical-wavefront. The phase rotation over a turn in the cone was 2π, and the topological charge of the generated vortex was 1. Here, we extend this idea in order to generate vortex with higher topological charge. Therefore, the phase rotation of the cone must increase for each turn as $n2\pi$. Applying same ideas developed previously, Eq. (6.1), we must increase the spiral radius r as $r(\theta) = nb\theta$ in order to increase the rotation of the phase by $n2\pi$.

However, if the spiral is constructed in that way, the spacing between turns is increased from a to na, and therefore, higher diffraction grating will appear and energy will spread into a multi focal beam as shown in Fig.6.8. Actually, the higher diffraction grating orders of a spiral generates high order Bessel beam. The beams presented in Fig.6.8 (right) corresponding to the diffraction order $N = 2$ were second order Bessel beams. Figure 6.13 shows a more clear example. There, in the left subplot a first order Bessel beam is generated at $a/\lambda = 1.2$. On the right, the frequency is increased to match $a/\lambda = 7.2$, the beam of the first order is generated far a way from the grating plane. Near the source appear the higher diffraction gratings. The profile of the 7th diffraction grating order generates a 7th order Bessel beam, where it can be appreciated that the numerical integration correctly agree the analytical estimation using $N = 7$. Therefore, HOBBs can be generated from the higher diffraction grating of a simple Archimedes' spiral.

For practical applications it must be desirable to generate a single HOBB

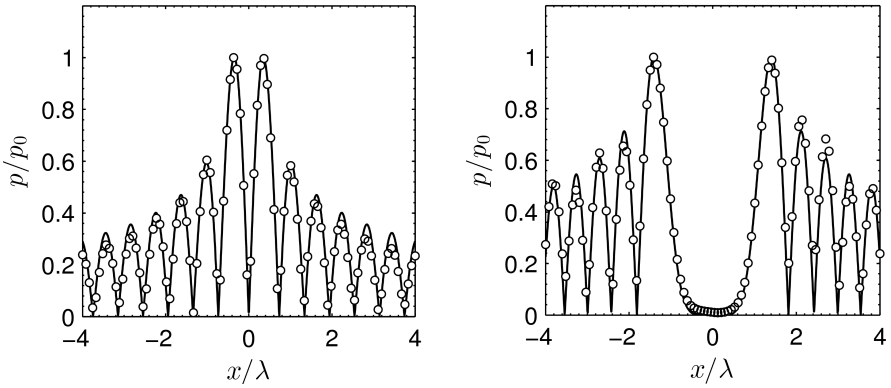


Figure 6.13: Generation of a high order Bessel beam from higher diffraction orders of a simple Archimedes' spiral grating. (continuous line) Analytical solution with (left) $N = 1$ and (right) $N = 7$, (circles) numerical integration at a distance $z = F(N)/2$

without any diffraction orders in order to do not spread energy from the main beam to other secondary spots, e.g. in addition to the previously 7th order Bessel beam of Fig. 6.13, all the inferior order Bessel beams are generated together.

The only way to increase the radius of the spiral as $r(\theta) = nb\theta$, while maintaining the grating spacing between turns, a, is to add additional arms to the spiral that fills the space between the stretched new curve. The general expression of n-arms spiral is

$$r_j = nb\left(\theta + j\frac{2\pi}{n}\right). \tag{6.18}$$

Therefore, there exists n curves, each j curve is separated a distance a from its adjacent curve, and each curve start from the origin at different angles, equispaced $2\pi/n$. Figure 6.14 shows various spirals with increasing number of branches. In the case of $n = 2$, it can be observed that the curve for the $j = 1$ branch (black spiral) have a growth slope of $\Delta r/\Delta\theta = 2b$. Therefore, the phase rotates at $\Delta\phi = \Delta\theta = 2$. Same applies to the second arm, but this arms maintain the separation between turns constant, allowing the generation of the Bessel conical wavefront for the first diffraction order. As Fig. 6.14 shows, other possibilities are also feasible in order to obtain higher spiral arms. The main issue is that when the number of arms increases the aperture between them does not remain constant near the center, when obviously in the limit $n \to \infty$, the structure becomes completely opaque if it is formed by finite sized scatterers, or in-existent if the grating is formed by finite sized slits.

As long the spacing between spiral arms is kept constant at a distant a, the diffraction produced by the grating will create a cone with same angle that for

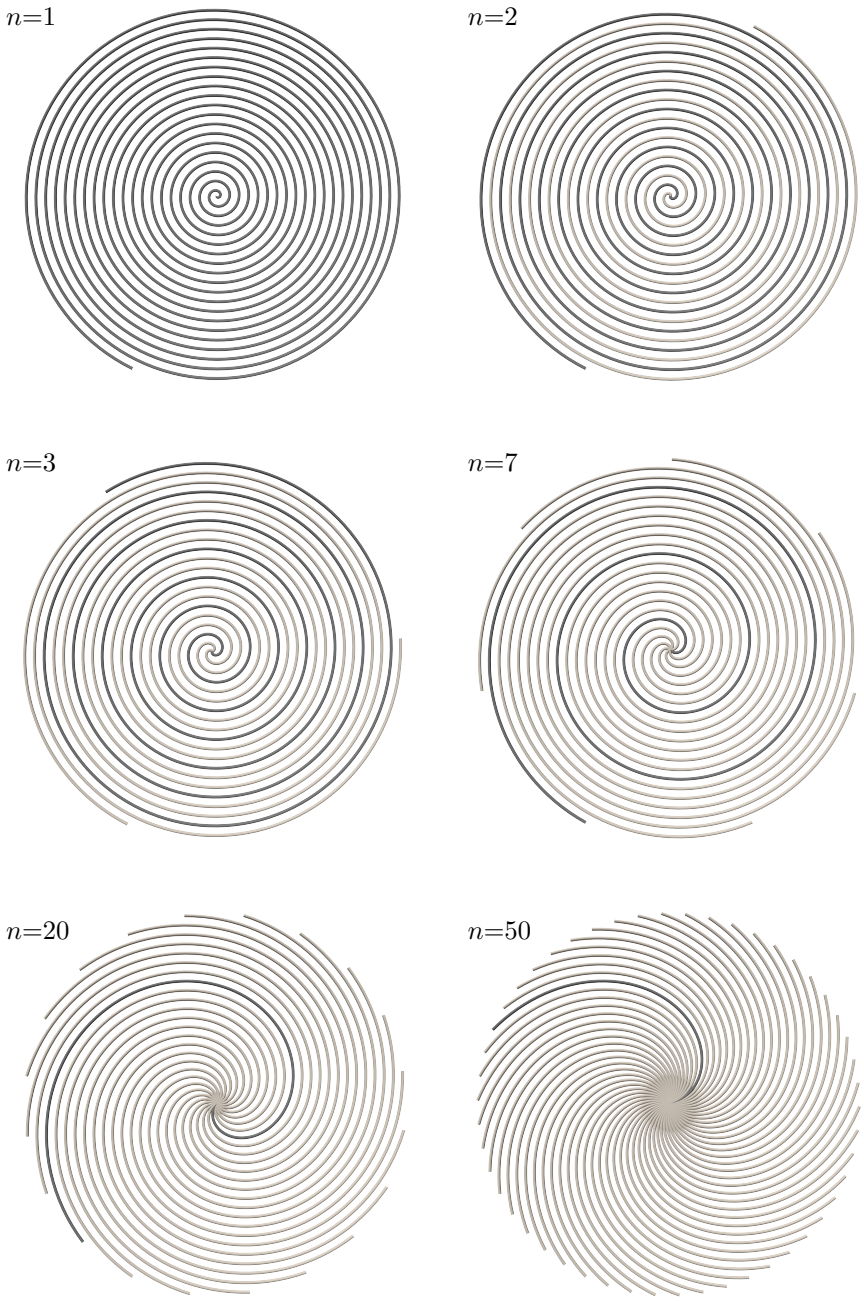


Figure 6.14: Scheme of a variety of n-arm spirals.

the first order Bessel Beams. When this conical wavefront converges to the axis, a Bessel beam is also generated. However, due to the rotation of the phase is increased by a factor of n, the corresponding beam is a nth-order Bessel beam. It can be appreciated in the last term of Eq. (6.11), that the topological charge will also be increased by a factor n. The number of arms of a spiral directly corresponds to the order of the Bessel beam generated and therefore to the topological charge of the acoustical vortex.

Beam profiles of the generated HOBBs are presented in Figs. 6.15-6.17. The magnitude of the field transversal sections are shown in Fig. 6.15 for n-arm spiral gratings of $n = 1, 2, 3, 7, 20, 50$. Here, the grating parameters were selected as $a/\lambda = 1.2$ and $\beta = 56.4^{\circ}$. First, in Fig. 6.15 we represent a transversal cut of the field measured at $z = F/2$. As can be seen, the field is zero at the axis of the beam, and the central null spot increases in size according to the number of branches of the spiral. The generated field is nearly zero in a cylindrical volume around the axis: the higher the number of arms of the spiral, the bigger the volume around the axis where the field is nearly zero. Even in the case of a 50 branches spiral, the generated beam profile agrees with a 50th order Bessel beam. In this case, the corresponding central null is generated over a roughly cylindrical volume of 18 λ diameter (in agreement to Eq. (6.16) and a height of F (in agreement to Eq. (6.12).

The location of the ring shaped lateral lobes, where the field increases to its maximum, also matches the beam profile of the function $J_n(2\pi/ar)$. A close comparison will be presented later. On the other hand, it can be appreciated that the ringed lateral lobes present some oscillations or bumps. They are more evident in the higher order Bessel beams. If the transverse plane where the measurement is done moves from $z = F/2$ to $z = F/2 + \Delta F$, these oscillation rotate around the axis. Furthermore, the number of oscillations is proportional to the order of the Bessel beam. They can be associated to the geometrical laws of perfect constructive interference around the axis for each arm of the spiral, in analogy to Eq. (6.14). Therefore, this results shows evidence of that the focal $F(r_F, \theta, z_F)$ for n-arms develop equispaced n helix curves that rotates around the axis.

On the other hand, the phase of the nth-order Bessel beam rotates around the axis forming an acoustic vortex. As can be seen in Fig. 6.16, the topological charge of the beam, i.e. the number of $n2\pi$ phase increments in a turn, is proportional to the number of branches. Furthermore, it is in agreement with the n-th order phase rotation characteristic HOBBs. These features are specially visible around the ringed areas of the field in which the field is maximum, according to Fig. 6.15.

Figure 6.17 shows the magnitude over the $(x = 0)$ plane. The generated beams correctly agrees with the truncated HOBBs. The extension of the minimum at the axis is in all cases $F = XXX\lambda$. Another feature is that in the case of higher n, i.e. $n = 50$, the extension of the maximum lateral lobe ring is shorter. This is due to the finite size structure, the beam only can be formed in the volume sonificated

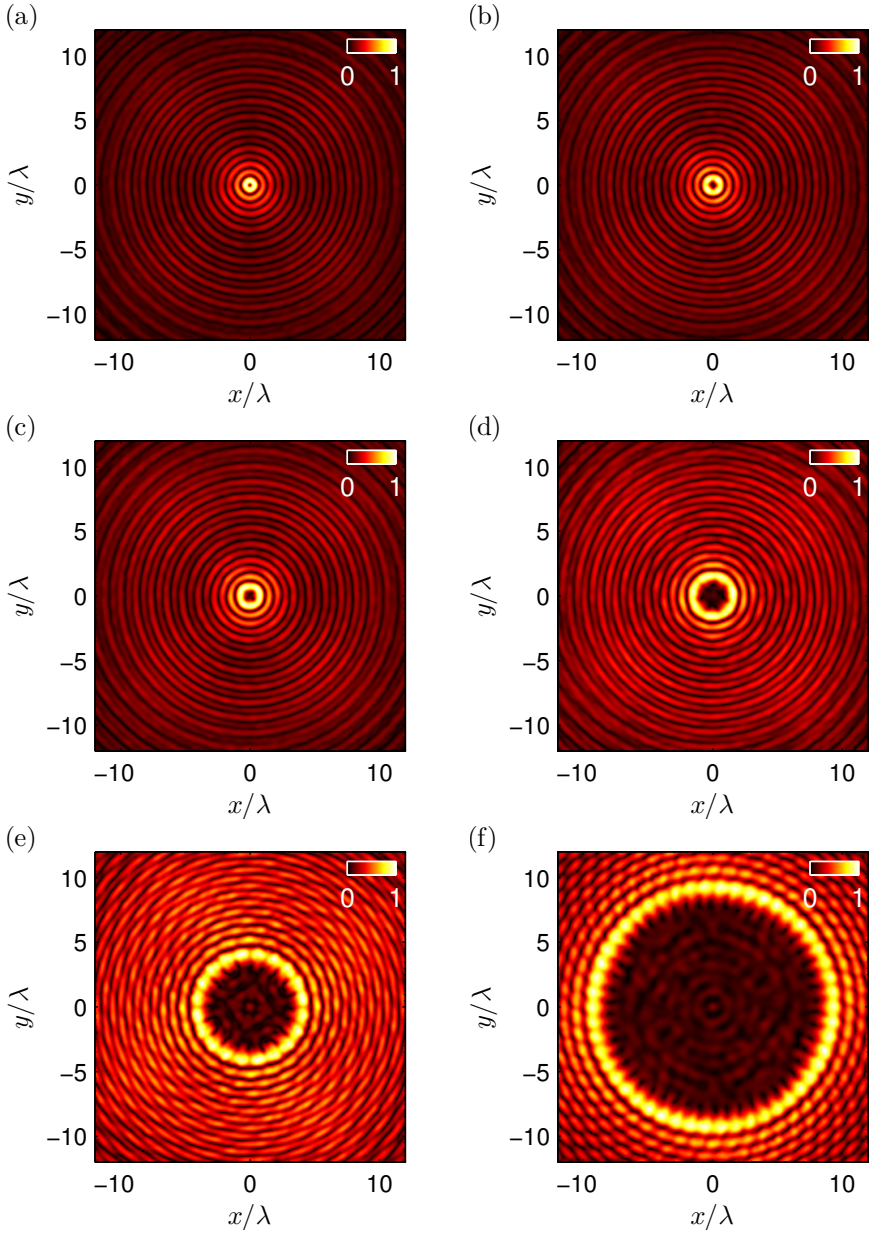


Figure 6.15: Magnitude of the transversal section of the field generated by a n-arm spiral grating, from (a-f), $n = 1, 2, 3, 7, 20, 50$. Colorbars in $p/p_{\max}$ units.

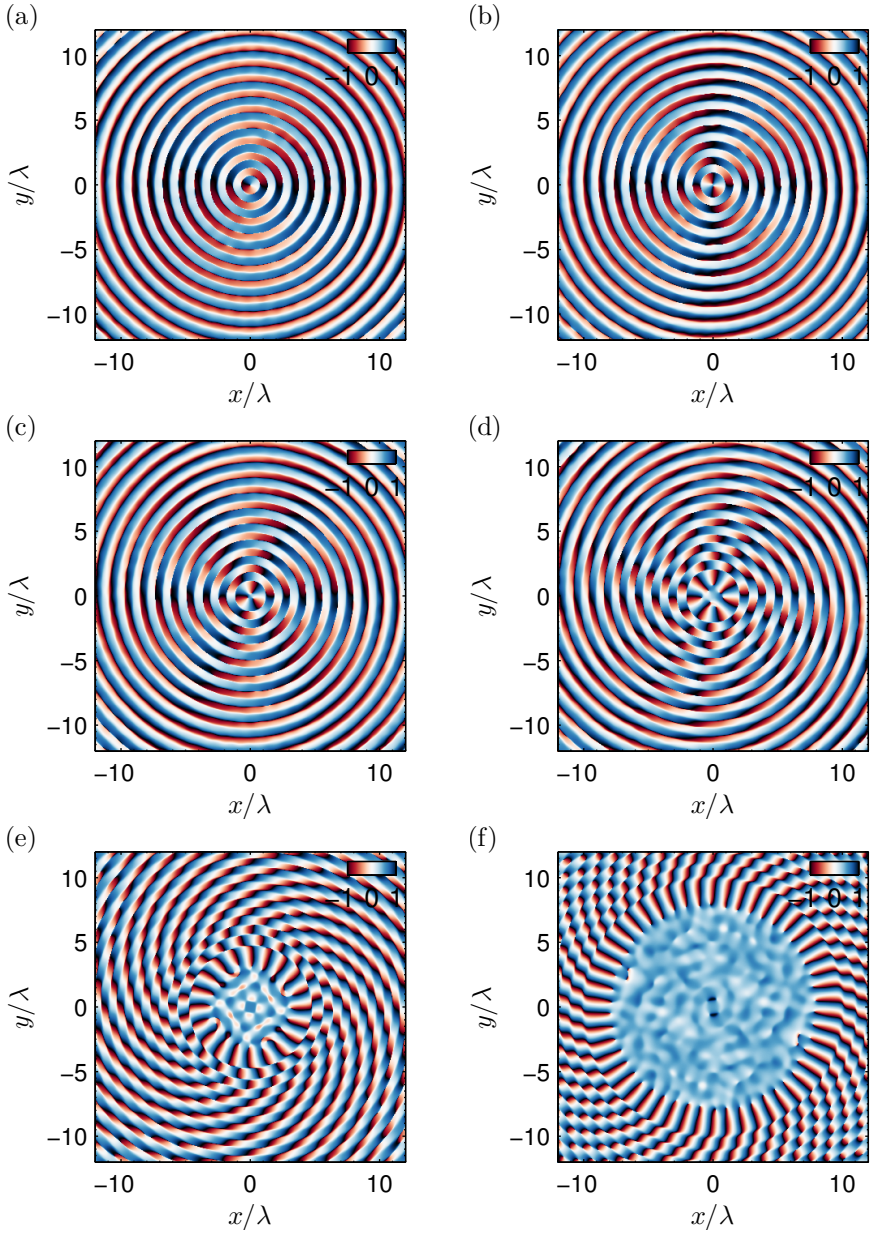


Figure 6.16: Phase of the transversal section of the field generated by a n-arm spiral grating, from (a-f), $n = 1, 2, 3, 7, 20, 50$. Colorbars in ϕ/π units.

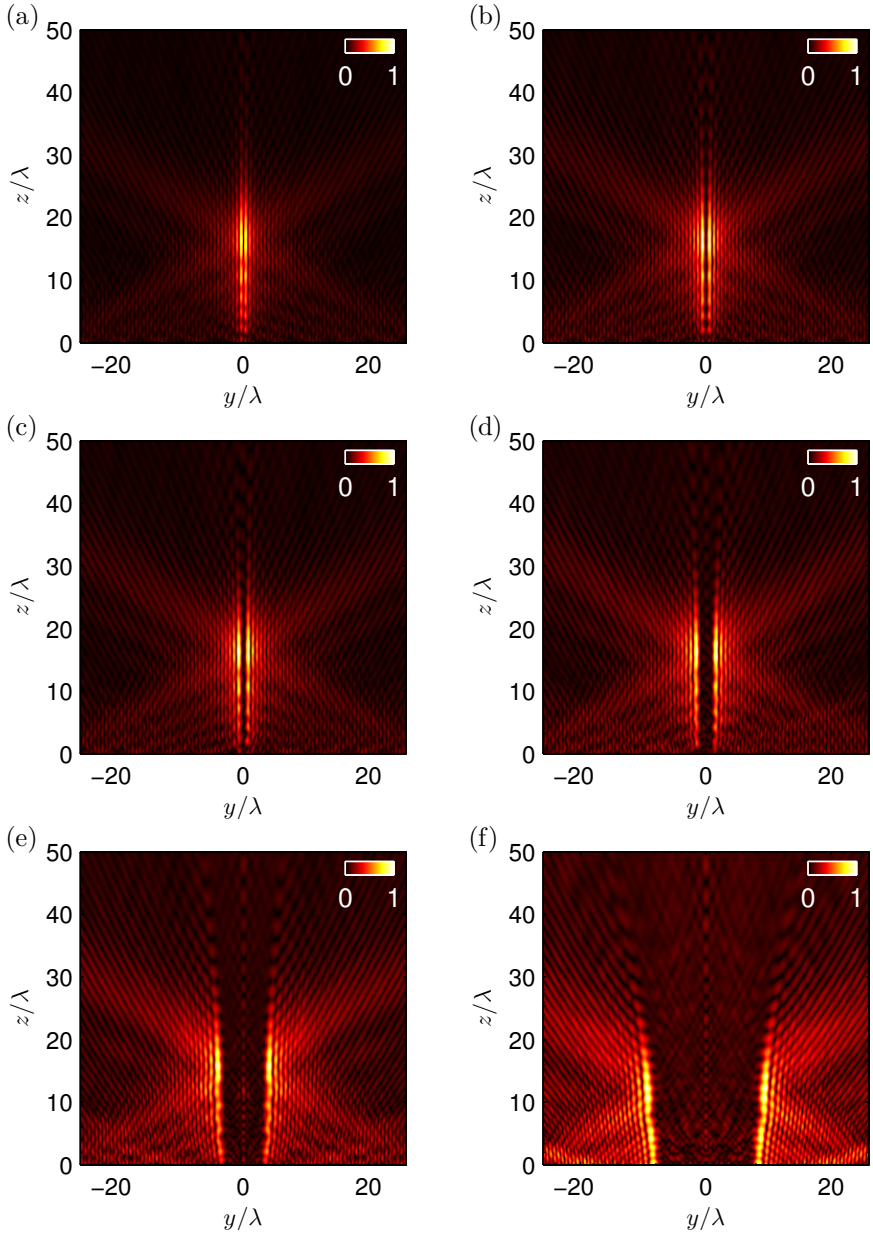


Figure 6.17: Magnitude of the axial distribution of the field for the n-arm spiral grating, from (a-f), $n = 1, 2, 3, 7, 20, 50$. Colorbars in $p/p_{\max}$ units.

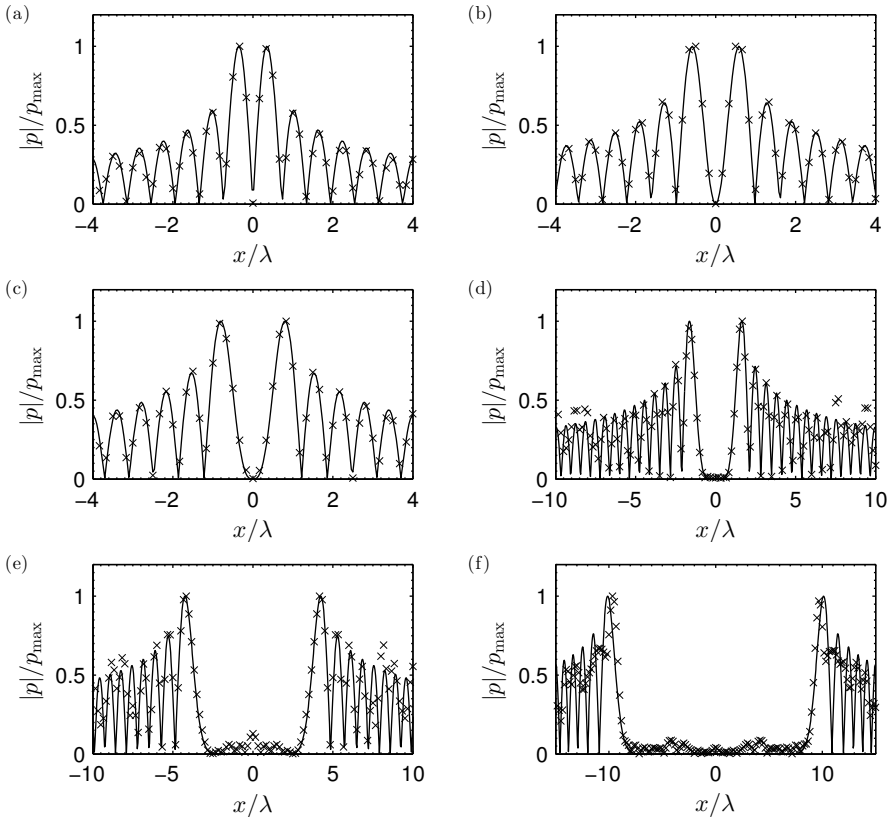


Figure 6.18: Magnitude of a transversal cut of the field for the n-arm spiral grating, from (a-f), $n = 1, 2, 3, 7, 20, 50$. (Markers) k-space numerical simulation, (continuous line) analytical HOBBs solutions.

by the conical wavefront. This volume extends from $z = 0$ to $z = F$ at the axis, but for radially distant points, this distance is reduced. Any case, this limitation does not impedes the correct formation of the truncated Bessel beam, even in the case of $n = 50$.

In order to demonstrate the multiple helix that conforms the acoustic vortex, we can represent the isosurface of the equal phase points. The modulations in the field magnitude over the rings of the high order Bessel beam correctly matches the helical shape shown of this reconstructed Fig. 6.21, in analogy with the analytical locus by Eqs. (6.14-6.15). The number of helix arms is equal to the number of spiral arms of the gratings, and its radius grows also withe the order of the Bessel beam generated.

Finally, in order to study these beams in a more realistic configuration, simulations of the full 3D problem of the same system were performed. In these

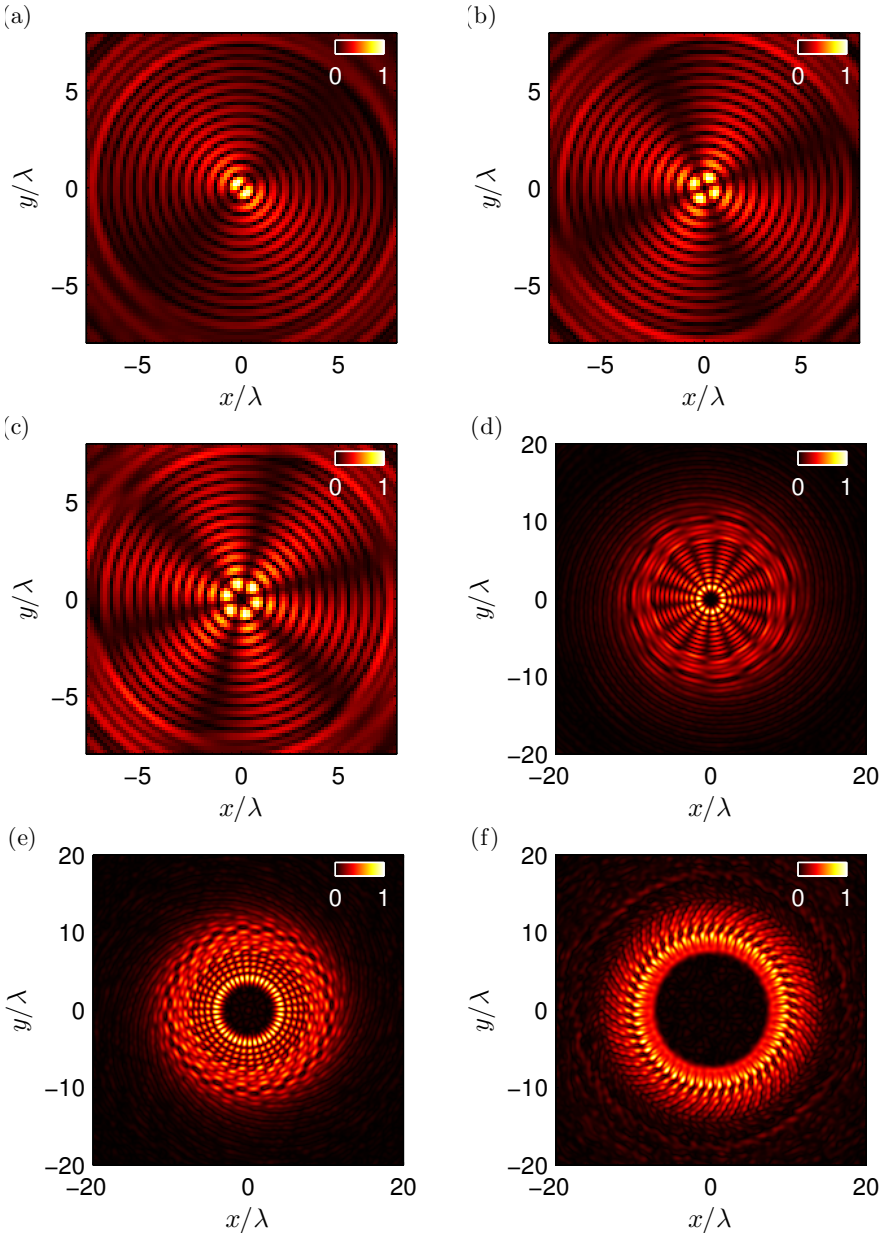


Figure 6.19: Magnitude of the field for the n-arm spiral grating, from (a-f), $n = 1, 2, 3, 7, 20, 50$ obtained by k-space numerical simulation. Colorbars in $p/p_{\max}$ units.

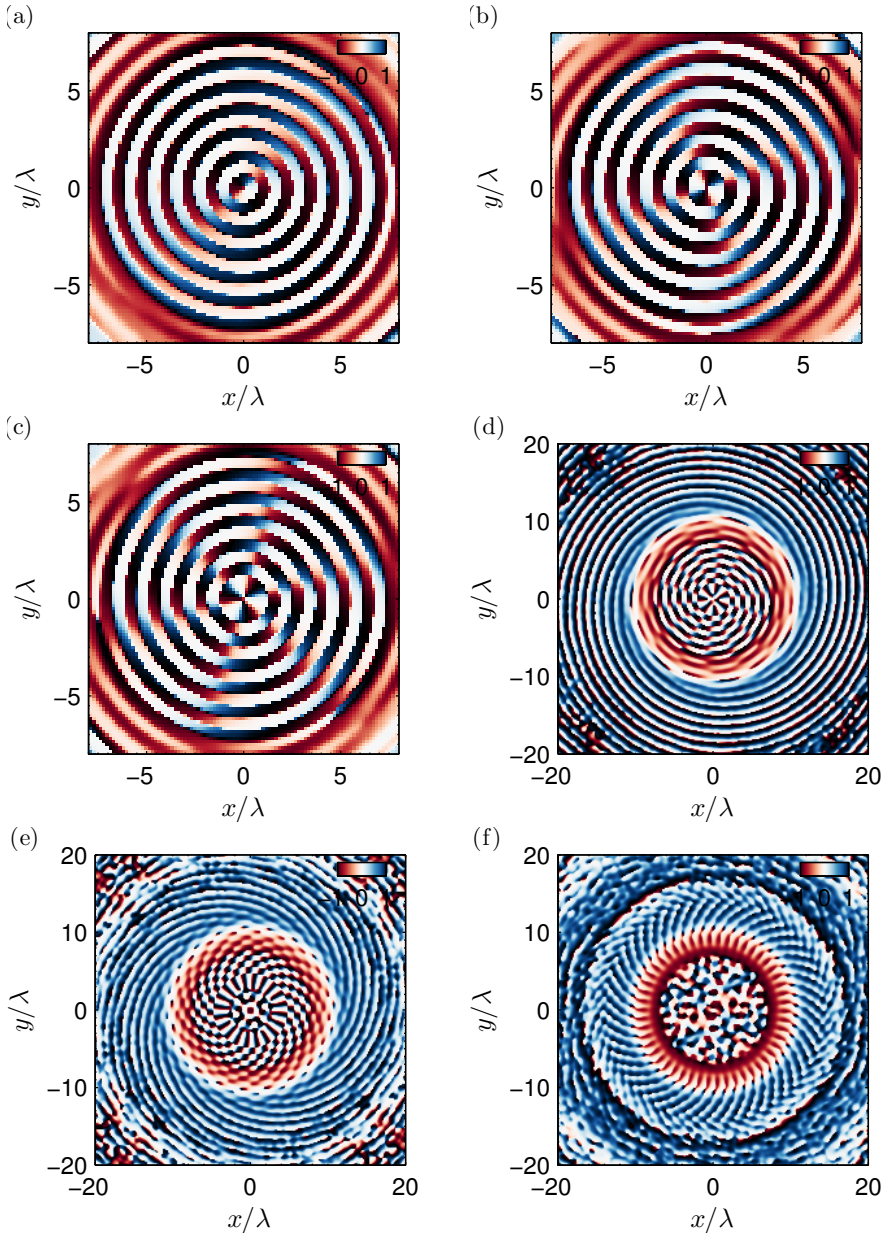


Figure 6.20: Phase of the field for the n-arm spiral grating, from (a-f), $n = 1, 2, 3, 7, 20, 50$ obtained by k-space numerical simulation. Colorbars in ϕ/π units.

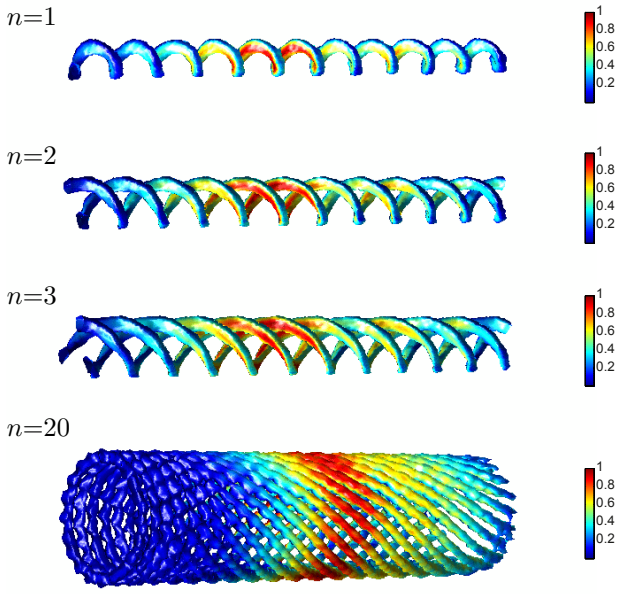


Figure 6.21: Reconstruction of the helical vortex by an isosurface of field points with equal phase. The number of helix arms is equal to the number of spiral arms of the gratings. Colorbars in $p/p_{\max}$ units.

simulations, instead of considering the scatterers perfectly rigid, the grating was included as a stainless steel plate, with same parameters than in the previous experimental setup. Thus, longitudinal wave propagation over the bulk of the steel plane were included. However, shear waves were not included in the simulations for the sake of simplicity. The simulation parameters used for the water media were $c_0 = 1490$ m/s and $\rho_0 = 1000$ kg/m^3 and for the grating plate $c_0 = 6100$ m/s and $\rho_0 = 7850$ kg/m^3. Losses were neglected in both media. Figure 6.18 shows the analytical HOBBs and the simulations of the proposed steel spiral gratings. Excellent agreement is obtained between the theory and the realistic simulations. Due the finite size of the structure, in this cases reduced to $R_{\max} = 25a$, the truncation effect of the Bessel function is more evident, as can be observed in the mismatching of the farther lateral lobes of the simulated beam. Furthermore, the characteristic oscillations of the maxima due to the helix focusing are more evident, as can be observed clearly in Fig. 6.19. It is worth noting here that those maxima are static, at this transversal cut ($z = F/2$), but rotates when the measurement is realized in a different plane according a multiple branch helix.

Concerning the vortex phase, the field also rotates with a topological charge equal to the spiral number of arms. Only in the case of $n = 50$ the beam is roughly generate. This effect is related to the finite sized aperture grating, where the cone

barely cover the volume necessary to generates the 18λ diameter of the ring shaped beam. However, even in this situation the central dark spot is generated, due to at the axis the conical wavefront always covers the volume for $z < F$. Those results evidence the feasibility of high order Bessel beam generation by spiral grating in realistic configurations.

6.5 Weakly nonlinear chiral beams

The nonlinear propagation of acoustic vortex have been studied previously. Most of these studies employs arrays of transducers to electronically modify the phase profile at the source plane. Acoustic vortex beams including shocks has been tested numerically and experimentally, where rotational shock waves have been generated. If nonlinear effects are produced in the propagation path and not near or inside the spiral grating, the propagation of electronically generated beams and the diffraction grating HOBBs proposed here will present high similarities.

We present simulations of the full-wave Eqs (3.1, 3.2, 3.3). The grating is designed as in previous simulations, where the nonlinearity of the water is introduced by the nonlinear parameter $B/A = 5$. Nonlinearity in the bulk of the steel plate is neglected. As Figs (6.22-6.22) shows, nonlinear acoustic vortex are produced in a similar fashion than in the preceding sections. However, in order to correctly account for higher spectral components, the numerical grid have been refined compared to the numerical results presented below. Due to the computation requirements of the resulting 3D problem, the total size of the domain of integration has to be reduced, and therefore, the total aperture, i.e. the number of turns of the spiral, has been reduced dramatically. In this section, the grating spiral is composed by only by 5 turns. These computational limitation impedes the calculation of higher Bessel beams due to the ring lateral lobes falls out of the domain. Other restriction of the full 3D nonlinear numerical problem is that the number of harmonics is very limited, and therefore, the simulations only can take into account weakly nonlinear propagation.

However, the basic features of the nonlinear vortex up to $n = 5$ can be presented. Figure 6.22 shows the magnitude of the first and its second harmonic transversal field distribution. It can be observed that due to the limited aperture grating, the Bessel beam is not correctly formed, but it can be appreciated how the characteristic lateral lobes appears. The zero at the axis roughly appears for the first and third order Bessel-like beams. In the case of $n = 5$ cannot be formed correctly. Here, the focalization of each spiral arm that creates n modulations over the lateral maxima is more evident. Again, if the measurement plane is shifted a small increment in z axial direction, those maxima rotates. Thus, the maxima conforms an n-helix curve. The second harmonic field generated in propagation also focuses on these maxima. In addition, second harmonic field also present additional modulations in the positions between the first harmonic modulations,

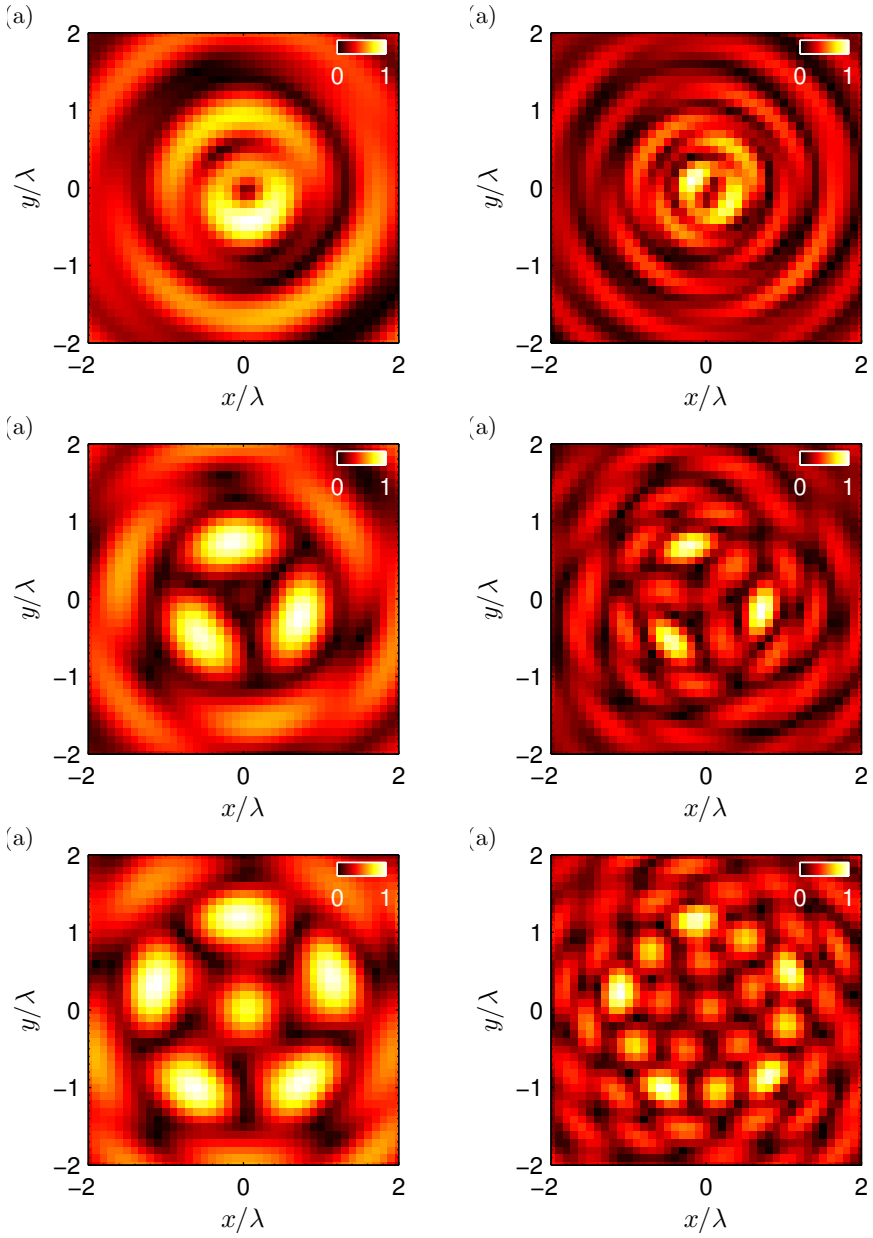


Figure 6.22: Magnitude of the field for the n-arm spiral grating, from top to bottom $n = 1, 3, 5$, (left column) first harmonic, (right column) second harmonic. Colorbars in $p/p_{\max}$ units.

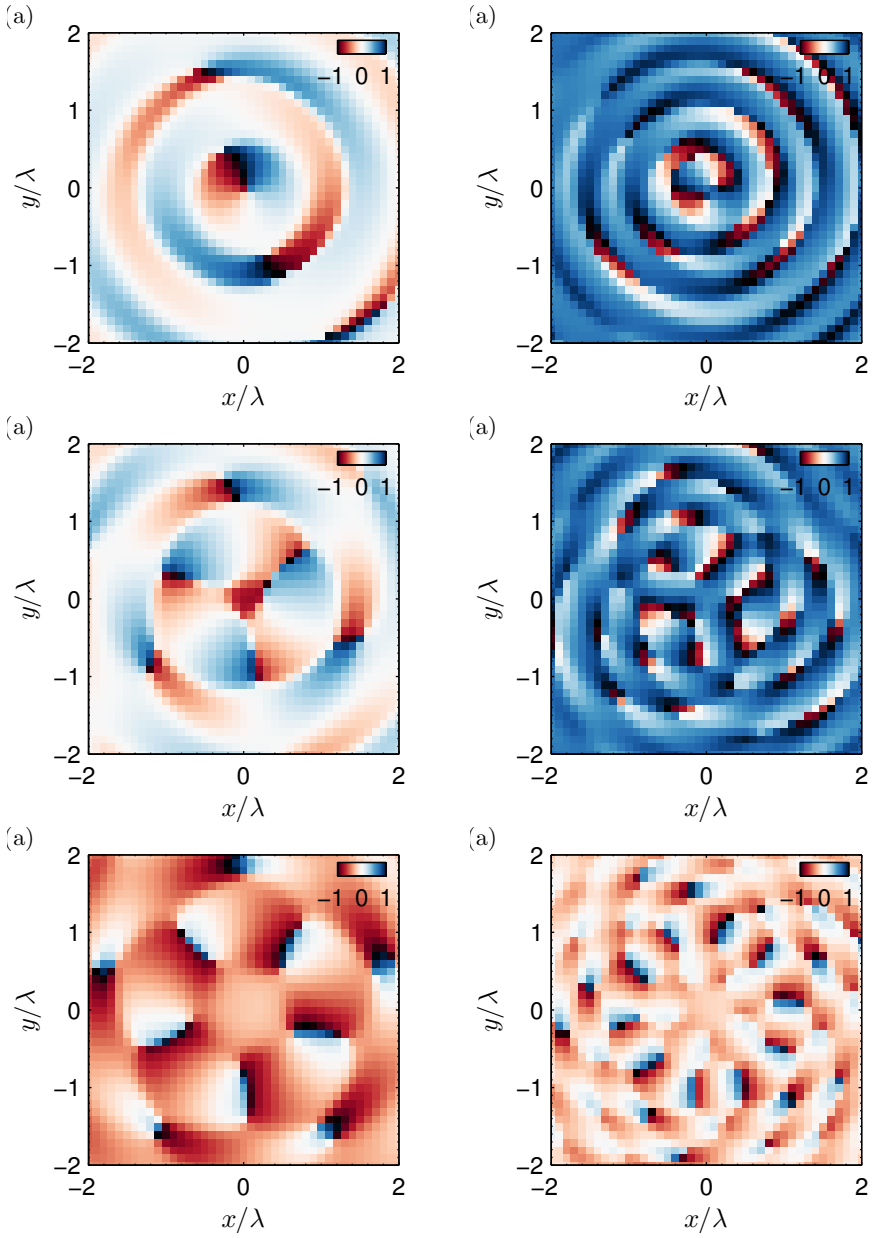


Figure 6.23: Phase of the field for the n-arm spiral grating, from top to bottom $n = 1, 3, 5$, (left column) first harmonic, (right column) second harmonic. Colorbars in ϕ/π units.

being these last of lower amplitude. Therefore, focalization around the axis of the higher harmonics are also helix shaped: the number of helix curves is the product of the harmonic index and the Bessel order.

Although the magnitude distribution of the field by this truncated grating hardly agrees to an ideal Bessel beam, the rotation of phase distribution is in agreement with the analytical vorticity of HOBBs. Thus, is clearly visible that the first harmonic in the simulations present a topological charge of n for the presented cases. In the case of second harmonic it rotates with topological charge $2n$. The topological charge is therefore the product of the the harmonic number and the order of the Bessel, i.e. the product of the harmonic and the number of arms. Thus, the conservation law for the ratio between the topological charge of the beam and the generated harmonic order is also observed (Marchiano et al., 2008). In this sense, nonlinearity present a opportunity to increase the topological charge of a generated beams.

Intensity vortex

One remarkable feature of the generated vortex is the acoustic intensity field. Due to the vortex rotation, the acoustic intensity vector presents, in addition to the axial, a rotational azimuthal component. The existence of this component evidences the possibility of using the HOBBs to transfer angular momentum to the media. Figure 6.24 presents an example of the transversal intensity distribution. The magnitude of the intensity maintains the characteristic ringed shape of the Bessel beam profile, wile the pointing vector of the intensity rotates around the axis.

The transfer of momentum from a wave to the media is closely related to the acoustic radiation force field. In the case of acoustic radiation force generated by scattering processes, i.e. when the gradient of the acoustic energy density is not null due to reflection on surfaces or objects, Bessel beams have been demonstrated high potential to generate interesting configurations for particle manipulation where negative axial radiation forces have been observed. On the other hand, if the gradient of the acoustic energy density is not null due to attenuation processes, there appears also a radiation force field. For plane waves, the acoustic radiation force exerted in the bulk of the lossy media is directly proportional to the intensity vector. The generated beams with acoustic intensity vortex can offer great potential in practical applications that uses acoustic radiation force generated by both, scattering or attenuation processes. The nonlinear acoustic radiation force will be studied in detail in Chapter 9 in the case of lossy media with frequency power law attenuation.

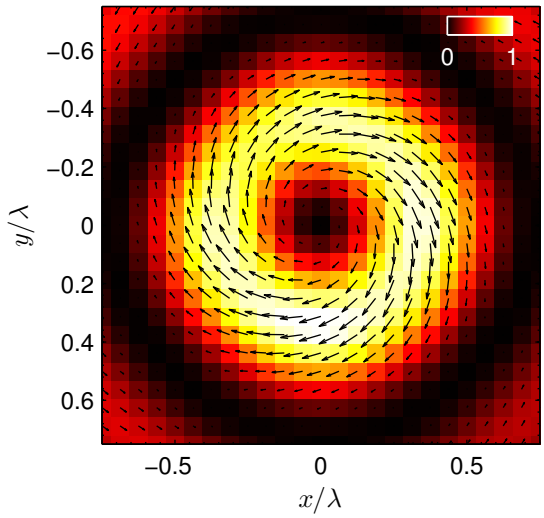


Figure 6.24: Intensity of a first order Bessel-like beam generated by a grating spiral. Colormap in $I/I_{\max}$ units, (arrows) intensity pointing vectors.

6.6 Conclusions

We have studied the scattering of Archimedes' spiral gratings, and demonstrated theoretically, experimentally and by numerical simulations that these diffraction gratings generates chiral beams. These beams are basically truncated high order Bessel beams, and are characterized by a null in the field all over it axis. It is demonstrated how the geometrical focal surrounds the axis in an helix shaped curve. It is of special interest the method presented for generation of arbitrary nth-order Bessel beams using regular spiral patters with n-arms or arms. It was shown that the order of the Bessel beam is directly the number of arms of the spiral. The radial position of the ringed lateral lobes grows with the order of the Bessel beam, and over it an acoustic vortex is generated. The topological charge of these vortex was also proportional to the number of arms of the spiral. Furthermore, we have demonstrated that another way to generate HOBBs is using higher diffraction orders, but this approach generates also secondary secondary beams along the axis and the energy spreads into all. Finally, The topological charge can be also increased by cumulative nonlinear effects, where the number of the harmonic is proportional to the product between the number of arms and the harmonic index.

The spiral diffraction gratings offers the possibility of dramatically increase the order of the beam by using together the mentioned effects. Thus, a grating made of high number of gratings can radiated with high frequency wave in order to excite superior diffraction orders. Finally, the ith-harmonic will present a topological

charge of inN, increasing its rotation and the possibility of transferring angular momentum to the media. On the other hand, currently work is being developed applying the technique of period varying grating exposed in Chapter 5 to an spiral configuration in order to achieve focusing of the vortex.

The presented method for synthesize HOBBs presents a high potential in ultrasound particle manipulation techniques and, in general, in acoustic radiation force applications in which the HOBBs have attracted great interest. This method provides the possibility of generation arbitrary order Bessel beams by a passive and extremely cheap device compared to active multiarrays. The generation of acoustic vortex by active means is limited by the amount of elements and its size. In contrast, the beam resolution by the proposed gratings is limited by the size of the scatterers and the space between them. Nowadays, with the increase in the performance of 3D printing and laser cutting techniques, the generation if HOBBs offer far more possibilities than its active counterpart to generate acoustical vortex.

References

Arlt, J and K Dholakia (2000). "Generation of high-order Bessel beams by use of an axicon". In: *Optics Communications* 177.1, pp. 297–301.

Bekshaev, A Ya and AI Karamoch (2008). "Displacements and deformations of a vortex light beam produced by the diffraction grating with embedded phase singularity". In: *Optics Communications* 281.14, pp. 3597–3610.

Brunet, Thomas, Jean-Louis Thomas, Régis Marchiano, and François Coulouvrat (2009). "Experimental observation of azimuthal shock waves on nonlinear acoustical vortices". In: *New Journal of Physics* 11.1, p. 013002.

Brunet, Thomas, Jean-Louis Thomas, Régis Marchiano, and François Coulouvrat (2010). "Experimental investigation of 3D shock waves on nonlinear acoustical vortices". In: *Physics Procedia* 3.1, pp. 905–911.

Demore, Christine, Zhengyi Yang, Alex Volovick, Han Wang, Sandy Cochran, Mike MacDonald, and Gabriel Spalding (2011). "A sonic screwdriver: Acoustic angular momentum transfer for ultrasonic manipulation". In: *Ultrasonics Symposium (IUS), 2011 IEEE International*. IEEE, pp. 180–183.

Durnin, Já, JJ Miceli Jr, and JH Eberly (1987). "Diffraction-free beams". In: *Physical Review Letters* 58.15, p. 1499.

Gspan, Stefan, Alex Meyer, Stefan Bernet, and Monika Ritsch-Marte (2004). "Optoacoustic generation of a helicoidal ultrasonic beam". In: *The Journal of the Acoustical Society of America* 115.3, pp. 1142–1146.

Heckenberg, NR, R McDuff, CP Smith, and AG White (1992). "Generation of optical phase singularities by computer-generated holograms". In: *Opt. Lett* 17.3, pp. 221–223.

Hefner, Brian T and Philip L Marston (1999). "An acoustical helicoidal wave transducer with applications for the alignment of ultrasonic and underwater systems". In: *The Journal of the Acoustical Society of America* 106.6, pp. 3313–3316.

Jimenez, Noe, Vicente Romero-García, R Picó, A Cebrecos, Víctor José Sánchez-Morcillo, LM Garcia-Raffi, Juan Vicente Sánchez-Pérez, and K Staliunas (2014). "Acoustic Bessel-like beam formation by an axisymmetric grating". In: *EPL (Europhysics Letters)* 106.2, p. 24005.

Marchiano, Régis, François Coulouvrat, Lili Ganjehi, and Jean-Louis Thomas (2008). "Numerical investigation of the properties of nonlinear acoustical vortices through weakly heterogeneous media". In: *Physical Review E* 77.1, p. 016605.

Marston, Philip L (2006). "Axial radiation force of a Bessel beam on a sphere and direction reversal of the force". In: *The Journal of the Acoustical Society of America* 120.6, pp. 3518–3524.

Marston, Philip L (2007a). "Negative axial radiation forces on solid spheres and shells in a Bessel beam". In: *The Journal of the Acoustical Society of America* 122.6, pp. 3162–3165.

Mitri, FG (2008). "Acoustic scattering of a high-order Bessel beam by an elastic sphere". In: *Annals of Physics* 323.11, pp. 2840–2850.

Mitri, FG (2009). "Negative axial radiation force on a fluid and elastic spheres illuminated by a high-order Bessel beam of progressive waves". In: *Journal of Physics A: Mathematical and Theoretical* 42.24, p. 245202.

Mitri, FG, TP Lobo, and GT Silva (2012). "Axial acoustic radiation torque of a Bessel vortex beam on spherical shells". In: *Physical Review E* 85.2, p. 026602.

Molerón, M., A. Leonard, and C. Daraio (2014). "Solitary waves in a chain of repelling magnets". In: *J. Appl. Phys.* 115.18, p. 184901.

Nye, JF and MV Berry (1974). "Dislocations in wave trains". In: *Proceedings of the Royal Society of London A: Mathematical, Physical and Engineering Sciences*. Vol. 336. 1605. The Royal Society, pp. 165–190.

Oemrawsingh, S. S. R., J. A. W. van Houwelingen, E. R. Eliel, J. P. Woerdman, E. J. K. Verstegen, J. G. Kloosterboer, and G. W. 't Hooft (2004). "Production and characterization of spiral phase plates for optical wavelengths". In: *Appl. Opt.* 43.3, pp. 688–694.

Romero-García, Vicente, R Picó, A Cebrecos, Víctor José Sánchez-Morcillo, and K Staliunas (2013). "Enhancement of sound in chirped sonic crystals". In: *Applied Physics Letters* 102.9, p. 091906.

Schwarz, Thomas (2013). "Rotation of particles by ultrasonic manipulation". PhD thesis. Diss., Eidgenössische Technische Hochschule ETH Zürich, Nr. 21572, 2013.

Skeldon, KD, C Wilson, M Edgar, and MJ Padgett (2008). "An acoustic spanner and its associated rotational Doppler shift". In: *New Journal of Physics* 10.1, p. 013018.

Thomas, Jean-Louis and Régis Marchiano (2003). "Pseudo angular momentum and topological charge conservation for nonlinear acoustical vortices". In: *Physical review letters* 91.24, p. 244302.

Vasara, Antti, Jari Turunen, and Ari T Friberg (1989). "Realization of general nondiffracting beams with computer-generated holograms". In: *JOSA A* 6.11, pp. 1748–1754.

Wu, Junru (1991). "Acoustical tweezers". In: *The Journal of the Acoustical Society of America* 89.5, pp. 2140–2143.

Yoon, Changhan, Bong Jin Kang, Changyang Lee, Hyung Ham Kim, and K Kirk Shung (2014). "Multi-particle trapping and manipulation by a high-frequency array transducer". In: *Applied physics letters* 105.21, p. 214103.

Publications

The contents of this chapter have been presented in the following publications:

Journal papers

- **N. Jimenez**, V. J. Sanchez-Morcillo, R. Pico, L. Garcia-Raffi, V. Romero-Garcia and K. Staliunas "High-order acoustic Bessel beam generation by spiral gratings" *Ultrasonics*, *In preparation*

Conference proceedings

- **N. Jimenez**, V. J. Sanchez-Morcillo, R. Pico, L. Garcia-Raffi, V. Romero-Garcia and K. Staliunas "High-order acoustic Bessel beam generation by spiral gratings" *2015 International Congress on Ultrasonics*, Metz, France. May 10-15, (2015)